Dissertation

submitted to the
Combined Faculties for the Natural Sciences and for Mathematics
of the Ruperto-Carola University of Heidelberg, Germany
for the degree of
Doctor of Natural Sciences

Put forward by
Dipl.-Phys. Dominique Maurice Richard Corteville
born in Bad Friedrichshall, Germany

Oral Examination: 23.07.2015

Optimization of the measurement sequence used for functional Fourier Decomposition Magnetic Resonance Imaging of the human lung at 1.5 Tesla

Referees: Prof. Dr. Lothar Schad
Prof. Dr. Peter Bachert

Optimization of the measurement sequence used for functional Fourier Decomposition Magnetic Resonance Imaging of the human lung at 1.5 Tesla

Fourier Decomposition (FD) magnetic resonance imaging is a non-invasive method for assessing ventilation and perfusion in the lungs. However, the technique struggles with a low signal to noise ratio (SNR). This work analyzed and optimized the standard balanced steady-state free precession (bSSFP) sequence used in the FD framework. The biggest drawbacks of the standard sequence were the long echo time compared to the short T_2^* of the lung parenchyma and the restriction of the utilized flip angles, due to specific absorption rate (SAR) limitations. To achieve the necessary improvements, advanced techniques were used, specifically, (utra-)fast bSSFP, two speed variable-rate selective excitation (VERSE) pulses and variable flip angle (VFA) patterns. All steps of the optimization process were tested in both simulations and phantom measurements. The finished sequence was tested in two human studies, one featuring healthy volunteers and the other featuring patients with different types of lung cancer. In both studies the average SNR of the morphological images was increased by 47±5%, while the SNR of the functional images was increased by 53±7%. Furthermore, due to the higher SNR of the morphological images, both the effective resolution and the robustness of the functional images were increased. None of the employed techniques introduced any transient artifacts and possible blurring was minimized. Due to these improvements, this work reinforces both the position of FD MRI as a research tool and brings the technique closer towards a clinical application.

Optimierung der Messsequenz verwendet zur funktionellen Fourier Decomposition Magnetresonanztomographie der menschlichen Lunge bei 1.5 Tesla

Fourier Decomposition (FD) Magnetresonanztomographie ist ein nicht invasives Verfahren um die Ventilation und Perfusion in der menschlichen Lunge zu bestimmen. Allerdings wird die Methode durch ein geringes Signal zu Rausch Verhältnis (SNR) im Lungenparenchym stark beeinträchtigt. Diese Arbeit analysierte und optimierte die im FD Verfahren standardmäßig eingesetzte balanced steady-state free precession (bSSFP) Sequenz. Die größten Probleme der Standardsequenz sind hierbei die im Vergleich zum niedrigen T_2^* der Lunge langen Echozeiten und die Beschränkung der verwendbaren Flipwinkel durch die Limitation der spezifischen Absorptionsrate (SAR). Um die notwendigen Verbesserungen zu erreichen, wurden fortgeschrittene Sequenztechniken eingesetzt, namentlich (ultra-)fast bSSFP, two speed variable-rate selective excitation (VERSE) Pulse und ein System aus variablen Flipwinkeln (VFA). Alle Modifikationen wurden dabei sowohl in Simulationen, als auch in Phantommessungen getestet. Zusätzlich wurde die vollständig optimierte Sequenz in zwei Humanstudien eingesetzt. Sowohl in der Studie die an gesunden Probanden durchgeführt wurde, als auch an der Studie mit Lungenkrebspatienten, betrug der Zuwachs des SNR 47±5% in den morphologischen Bildern und 53±7% in den funktionellen Bildern. Ebenfalls wurden durch das erhöhte Signal in den morphologischen Bildern sowohl die effektive Auflösung, als auch die Robustheit der funktionellen Bilder verbessert. Keine der neu eingesetzten Methoden verursachte dabei zusätzliche, transiente Artefakte und Artefakte aufgrund von Unschärfe wurden minimiert. Diese Verbesserungen leisten einen wichtigen Beitrag um die FD Magnetresonanztomographie als wichtiges Instrument in der wissenschaftlichen Forschung zu etablieren und weiter an die klinische Routine heranzuführen.

Contents

1 Introduction

The lung is a highly specialized organ in the human body tasked with respiration. Its principal function is delivering fresh oxygen into the bloodstream and removing carbon dioxide from it. Due to its frequent interaction with the atmosphere outside of the body, the lung is often damaged by harmful particles in the air. This interaction can lead to various diseases, such as lung cancer, chronic obstructive pulmonary disease (COPD) or asthma. Lung diseases are one of the main causes of death in the modern world. As a consequence, pulmonary function such as pulmonary ventilation and perfusion are important biomarkers to monitor. Both of these parameters, as well as the ratio between them, are optimal indicators to examine the incidence and severity of both acute and chronic pulmonary diseases. Nowadays, the gold standard for regional investigation of these biomarkers is radionuclide planar scintigraphy [Mason et al., 2010] and single photon emission computed tomography (SPECT) [Roach et al., 2008], combined with 3D particle modeling [R., 2013]. However, due to the high cost of these techniques computer tomography (CT) scans are also commonly used to track structural defects. All of these methods suffer from the use of ionizing radiation, which make them especially undesirable for patients with chronic diseases requiring multiple follow-up scans or children. Magnetic resonance imaging (MRI) on the other hand does not suffer from this drawback. However, the regular proton MRI is generally unsuccessful due to the physical properties of the lung. The combination of low proton density, large susceptibility changes and constant motion lead to MR images that only showed the lung as a black hole. In turn, the efforts to visualize pulmonary ventilation using MRI have mostly focused on imaging using hyperpolarized noble gases, either ^{3}He [Mugler and Altes, 2013] or ^{129}Xe [Fain et al., 2010]. These techniques require elaborate equipment and expensive hyperpolarized tracers and thus, they are only available at a select few research centers. Pulmonary perfusion can also be examined using dynamic contrast enhanced (DCE) MRI via injection of paramagnetic contrast agents [Meaney et al.,

1999] or arterial spin labeling (ASL) [Buxton et al., 1998]. Although DCE MRI generally provides much higher signal than ASL, the administration and side effects of the contrast agent can be considered as a significant disadvantage.

Recently, a novel technique for functional pulmonary MRI has been developed. This method called Fourier Decomposition (FD) MRI acquires time-resolved sets of images during free breathing [Bauman et al., 2009] using a balanced steady-state free precession (bSSFP) imaging sequence [Carr, 1958]. After acquisition the images are registered to a reference image and subsequently periodic signal variations are separated using a Fourier analysis. In this manner a ventilation-weighted (V) and a perfusion-weighted (Q) image can be obtained. The clinical relevance of the technique has been validated in patient studies for different diseases, such as non-small-cell lung cancer [Sommer et al., 2013] and cystic fibrosis [Bauman et al., 2013]. These publications note that FD MRI offers clear advantages such as the omittance of all contrast agents and breath holds. However, it suffers from a low signal to noise ratio (SNR) due to the low proton density in the lung parenchyma. With patients being examined in the supine position, this effect is especially problematic in the anterior parts of the lung. The lack of sufficient SNR directly influences the quality of the subsequent data analysis either by standard FD or by the recently proposed quantitative approaches for perfusion [Kjørstad et al., 2014a] and ventilation [Kjørstad et al., 2014b].

The goal of this work was to maximize the possible SNR gain of pulmonary FD MRI by modifying the standard 2D balanced steady-state free precession (bSSFP) imaging sequence (also called TrueFISP, balanced FFE, or FIESTA). For this purpose a multitude of advanced sequence modifications were used. These techniques included changing the gradient timing of the sequence to an (utra-)fast bSSFP variant employing highly asymmetric readouts [Bieri, 2012]. Furthermore, the excitation pulses were altered using a two speed variable-rate selective excitation (VERSE) approach to allow the use of higher flip angles [Hargreaves et al., 2004]. Additionally, variable flip angle patterns were used for both the preparation of the magnetization and the acquisition of the signal. This method further increased the available flip angle range. Each optimization step was both simulated and tested on phantoms. Finally, studies using both healthy volunteers and lung cancer patients were performed to test the capabilities of the fully modified sequence.

2 Basics

This chapter will briefly cover the basics used in this work. It is split into three parts. The first part will cover the basics of Nuclear Magnetic Resonance (NMR), while the second part will demonstrate how NMR can be used for imaging. The last part of the chapter will sum up some basic information about the anatomy and the physiology of the human lung.

2.1 Nuclear Magnetic Resonance

The first basic observations about the magnetic moment of atomic nuclei were made in the early 1900s. In 1924, Wolfgang Pauli theorized that the hyper-fine structure could be explained by an interaction between the nucleus and its electrons [Pauli, 1924]. In the 30s Isaac Rabi performed experiments that were able to measure nuclear magnetic moments using resonance. First for protons [Rabi et al., 1934] and later for other nuclei [Rabi et al., 1939]. He was awarded the Nobel Prize in 1944 for these achievements. In 1946, both Felix Bloch [Bloch, 1946] and Edward Mills Purcell [Purcell, 1946] investigated NMR in solid and fluid probes and therefore shared the Nobel prize six years later. The following chapter will briefly cover the most important aspects of NMR. A full description of the physical basics can be found in [Abragam, 2007], [Slichter, 1996] and [Levitt, 2007].

2.1.1 Nuclear Spin and Magnetic Moment

All fundamental particles have an intrinsic angular momentum, which is called spin. All unpaired particles that make up regular matter (protons, neutrons and electrons) possess a spin of $S = 1/2$. However, in atomic nuclei protons and neutrons pair up separately and can cancel out their spins. Due to this all nuclei with an even number of protons and neutrons (e.g. ^{12}C and ^{16}O) have a total spin of zero. The assigned operator in quantum mechanics is called the spin-operator. This operator follows the algebraic characteristics of a general

angular momentum

$$\left[\hat{S}_i,\hat{S}_j\right] = i\hbar\epsilon_{ijk}\hat{S}_k, \quad \left[\hat{\mathbf{S}}^2,\hat{S}_i\right] = 0. \tag{2.1}$$

Without loss of generality one can construct eigenfunctions for the arbitrarily chosen z-axis

$$\hat{\mathbf{S}}^2|s,m_s\rangle = s(s+1)\hbar^2|s,m_s\rangle, \tag{2.2}$$

$$\hat{S}_z|s,m_s\rangle = m_s\hbar|s,m_s\rangle, \tag{2.3}$$

where $|s,m_s\rangle$ are the eigenstates. The values of s (the angular momentum quantum number) and m_s (the magnetic quantum number) follow the principle

$$s = 0, \frac{1}{2}, 1, \frac{3}{2}, 2, \frac{5}{2}, ... \tag{2.4}$$

$$m_s = -s, -s+1, ..., s-1, s. \tag{2.5}$$

Therefore, in a field-free space each state of $|s,m_s\rangle$ is $(2s+1)$ times degenerated. However, by adding an external magnetic field the degeneration can be nullified. Furthermore, a spin $\hat{S}$ is always linked to a magnetic moment $\hat{\mu}$ by the gyromagentic ratio γ

$$\hat{\mu} = \gamma\hat{S}. \tag{2.6}$$

The gyromagnetic ratio can by calculated using the Landé-factor g of the corresponding nucleus and the nuclear magneton μ_n

$$\gamma = \frac{g\mu_n}{\hbar}. \tag{2.7}$$

The nuclear magneton is a physical constant described by the mass of a proton m_p and the elementary electric charge e

$$\mu_n = \frac{e\hbar}{2m_p}. \tag{2.8}$$

The gyromagentic ratio of the hydrogen nucleus is the largest among all stable nuclei with $\gamma = 42.58\frac{MHz}{T}$. A list of γ-values for other important nuclei in NMR is shown in table 2.1.

Nucleus	Spin	Magnetic Moment [μ_n]	γ [MHz/T]	Abundance[%]
^{1}H	1/2	2.793	42.58	99.98
^{3}He	1/2	-3.685	-32.43	0.00013
^{17}O	5/2	-1.893	-5.77	0.037
^{19}F	1/2	2.627	40.05	100
^{23}Na	3/2	2.216	11.26	100
^{31}P	1/2	1.131	17.24	6.88
^{129}Xe	1/2	-1.345	-11.78	26.44

Table 2.1: *A list of selected NMR-active isotopes of interest in bio-medical applications. A negative sign for the moment and gyromagnetic ratio refers to the fact that the magnetic moment is antiparallel to the angular momentum vector [Haacke et al., 1999].*

2.1.2 Zeeman Effect

The Zeeman effect describes the splitting of a spectral line in an external electromagnetic field. A particle with charge e and mass m in a magnetic field has the following Hamiltonian

$$\hat{\mathbf{H}} = \frac{1}{2m}\left(\frac{\hbar}{i}\nabla - e\mathbf{A}(\hat{x},t)\right)^2 + e\Phi(\hat{x},t), \tag{2.9}$$

with the vector potential $\mathbf{A}(\hat{x},t)$ and the scalar potential $\Phi(\hat{x},t)$. Using the Coulomb gauge condition $\nabla\mathbf{A} = 0$ and neglecting the scalar potential, the Hamiltonian can be written as

$$\hat{\mathbf{H}} = -\frac{\hbar^2}{2m}\nabla^2 + \frac{i\hbar e}{m}\mathbf{A}\cdot\nabla + \frac{e^2}{2m}\mathbf{A}^2. \tag{2.10}$$

For an external field in z-direction given by $\mathbf{B} = (0,0,B_0)$ the vector potential can be written as $\mathbf{A} = -\frac{1}{2}(\hat{x}\times\mathbf{B}_0)$ and the Hamiltonian simplifies to

$$\hat{H} = -\frac{\hbar^2}{2m}\nabla^2 - \frac{e}{2m}J_z B0 + \frac{e^2B_0^2}{8m}(\hat{x}^2+\hat{y}^2), \tag{2.11}$$

where J_z is the component of the angular momentum operator in z-direction. If $\langle J_z\rangle \neq 0$ then the second term in equation 2.11 dominates the third term, which can thus be neglected. For particles without orbital angular momentum $\hat{\mathbf{J}} = \hat{\mathbf{S}}$. Therefore, the coupling term of the Hamiltonian can be written as

$$\hat{H} = -\gamma\hat{S}_z B_0. \tag{2.12}$$

Using equation 2.3 this leads to

$$\hat{H}|s,m_s\rangle = -\gamma B_0 \hat{S}_z|s,m_s\rangle = -\omega_0 m_s \hbar|s,m_s\rangle, \tag{2.13}$$

where $\omega_0 = \gamma B_0$ is the Larmor frequency. In conclusion, for each state $|s,m_s\rangle$ there are $(2+1)$ sub-states in an external magnetic field. These sub-states are separated by the energy $\Delta E = \hbar\omega_0$. For particles with a spin of 1/2 like protons this leads to two states $|m_s = +\frac{1}{2}\rangle$ and $|m_s = -\frac{1}{2}\rangle$. Using the value of the gyromagnetic ratio from the previous section the Larmor frequency of a proton is $\omega_0 = 63.9$ MHz in an external field with a strength of $B_0 = 1.5$T.

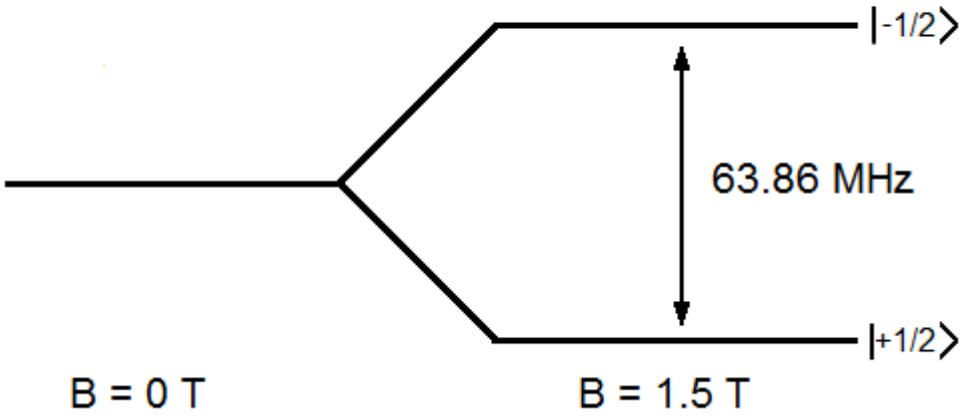

Figure 2.1: *In a hydrogen nucleus the two energy levels are split when placed in an external magnetic field. The difference between the energy levels is proportional to the magnetic field strength.*

2.1.3 Macroscopic Magnetization

All previous observations were based on a single spin system. However, NMR systems commonly examine volumes of at least one cubic millimeter. The order of the number of protons present in such a volume is approximately 10^{20}. Therefore, it is imperative to look at the macroscopic magnetization vector $\mathbf{M}$ which is the sum of all individual magnetic moments

$$\mathbf{M} = \frac{1}{V}\sum_{n=1}^{N}\langle\hat{\boldsymbol{\mu}}\rangle_n. \tag{2.14}$$

In an external field in z-direction the expectation values of both the x and the y-component disappear, leaving only the z-component

$$\mathbf{M} = M_0 = \frac{1}{V}\sum_{n=1}^{N}\langle\hat{\mu_z}\rangle_n. \tag{2.15}$$

Using equation 2.6 the magnetic moment can be exchanged for the spin

$$M_0 = \frac{\gamma}{V}\sum_{n=1}^{N}\langle\hat{S_z}\rangle_n. \tag{2.16}$$

Utilizing the eigenvalue equation 2.3 and the probability p_{m_s} that state m_s is occupied this leads to

$$M_0 = \frac{N}{V}\gamma\hbar\sum_{m_s=-S}^{S} m_s p_{m_s}. \tag{2.17}$$

The probability p_{m_s} can be calculated using Boltzmann statistics, provided that the system is in thermal equilibrium

$$p_{m_s} = \frac{1}{Z}e^{-\frac{E_{m_s}}{k_B T}}, \quad Z = \sum_{m_s} e^{-\frac{E_{m_s}}{k_B T}}. \tag{2.18}$$

Inserted into the previous equation this leads to

$$M_0 = \frac{N}{V}\gamma\hbar\frac{\sum_{m_s=-S}^{S} m_s e^{\frac{m_s\hbar\omega_0}{k_B T}}}{\sum_{m_s=-S}^{S} e^{\frac{m_s\hbar\omega_0}{k_B T}}}. \tag{2.19}$$

At human body temperature ($T \approx 310\text{K}$) the thermal energy $k_B T$ is several dimensions larger than the energy difference of the Zeeman levels. Thus, the exponential function can be approximated by $e^x \approx 1 + x$. Further, using the relation $\sum_{m=-S}^{S} m^2 = \frac{1}{3}S(2S+1)(S+1)$ this leads to

$$M_0 = \frac{N}{V}B_0\frac{\gamma^2\hbar^2}{3k_B T}S(S+1). \tag{2.20}$$

In conclusion, the macroscopic magnetization at thermal equilibrium is proportional to the spin density $\frac{N}{V}$, the strength of the external magnetic field B_0 and to the second power of the gyromagnetic ratio γ^2.

2.1.4 Motion of Non-Interacting Spins

The behavior of a nuclear spin system in an external magnetic field can be described by using the Ehrenfest theorem [Ehrenfest, 1927]

$$\frac{d}{dt}\langle\hat{\boldsymbol{\mu}}\rangle = \langle\frac{\partial\hat{\boldsymbol{\mu}}}{\partial t}\rangle + \frac{i}{\hbar}\langle\left[\hat{H},\hat{\boldsymbol{\mu}}\right]\rangle. \tag{2.21}$$

Using the equations 2.1, 2.6 and 2.13 this can be calculated as

$$\frac{d}{dt}\langle\hat{\boldsymbol{\mu}}\rangle = \gamma\langle\hat{\boldsymbol{\mu}}\rangle \times \mathbf{B}. \tag{2.22}$$

Equation 2.14 makes it possible to switch to the macroscopic magnetization $\mathbf{M}$

$$\frac{d}{dt}\mathbf{M} = \gamma\mathbf{M} \times \mathbf{B}. \tag{2.23}$$

2.1.5 Radiofrequency Excitation

To detect a signal in an NMR experiment the macroscopic magnetization has to be disturbed from its thermal equilibrium. To achieve this an external magnetic field $\mathbf{B}_1$ alternating at the Larmor frequency $\omega_1 = \omega_0$ is applied. It is circularly polarized and its components are given by

$$\mathbf{B_1} = \begin{pmatrix} B_1\cos(\omega_1 t) \\ B_1\sin(\omega_1 t) \\ 0 \end{pmatrix}. \tag{2.24}$$

Putting this into equation 2.23 with B_0 in z-direction, results in

$$\frac{d}{dt}\mathbf{M} = \gamma\mathbf{M} \times \begin{pmatrix} B_1\cos(\omega_1 t) \\ B_1\sin(\omega_1 t) \\ B_0 \end{pmatrix}. \tag{2.25}$$

The mathematical treatment can by simplified by introducing a rotating frame. Specifically this allows the elimination of the precession and the time dependence of $\mathbf{B}_1$. The new coordinate system (x',y',z') rotates with the Larmor frequency around the z-axis of the laboratory system

$$\begin{pmatrix} x' \\ y' \\ z' \end{pmatrix} = \begin{bmatrix} \cos(\omega_0 t) & -\sin(\omega_0 t) & 0 \\ \sin(\omega_0 t) & \cos(\omega_0 t) & 0 \\ 0 & 0 & 1 \end{bmatrix} \begin{pmatrix} x \\ y \\ z \end{pmatrix}. \tag{2.26}$$

In the rotating frame equation 2.23 can be written as:

$$\frac{d}{dt}\mathbf{M}' = \gamma \mathbf{M}' \times \begin{pmatrix} B_1 \\ 0 \\ B_0 - \frac{\omega_1}{\gamma} \end{pmatrix}. \tag{2.27}$$

At resonance condition $\omega_1 = \omega_0$ the field in z-direction vanishes and the effective magnetic field is aligned along the x'-axis. The solution to equation 2.23 is given by:

$$\mathbf{M} = M_0 \begin{pmatrix} -\sin(\omega_1 t)\sin(\omega_0 t) \\ \sin(\omega_1 t)\cos(\omega_0 t) \\ \sin(\omega_1 t) \end{pmatrix} \qquad \text{for the laboratory frame} \tag{2.28}$$

$$\mathbf{M}' = M_0 \begin{pmatrix} 0 \\ \sin(\omega_1 t) \\ \cos(\omega_1 t) \end{pmatrix} \qquad \text{for the rotating frame.} \tag{2.29}$$

A graphical representation of this can be viewed in figure 2.2. The flip angle is defined as the angle to which the net magnetization $\mathbf{M}$ is tipped relative to B_0 via the application of B_1

$$\alpha = \gamma \int_0^{T_{RF}} B_1(t) dt. \tag{2.30}$$

T_{RF} is the duration of the RF pulse. Common flip angles used in NMR experiments are 90°, which flips the magnetization into the xy-plane and 180°, which inverts the magnetization to the -z direction.

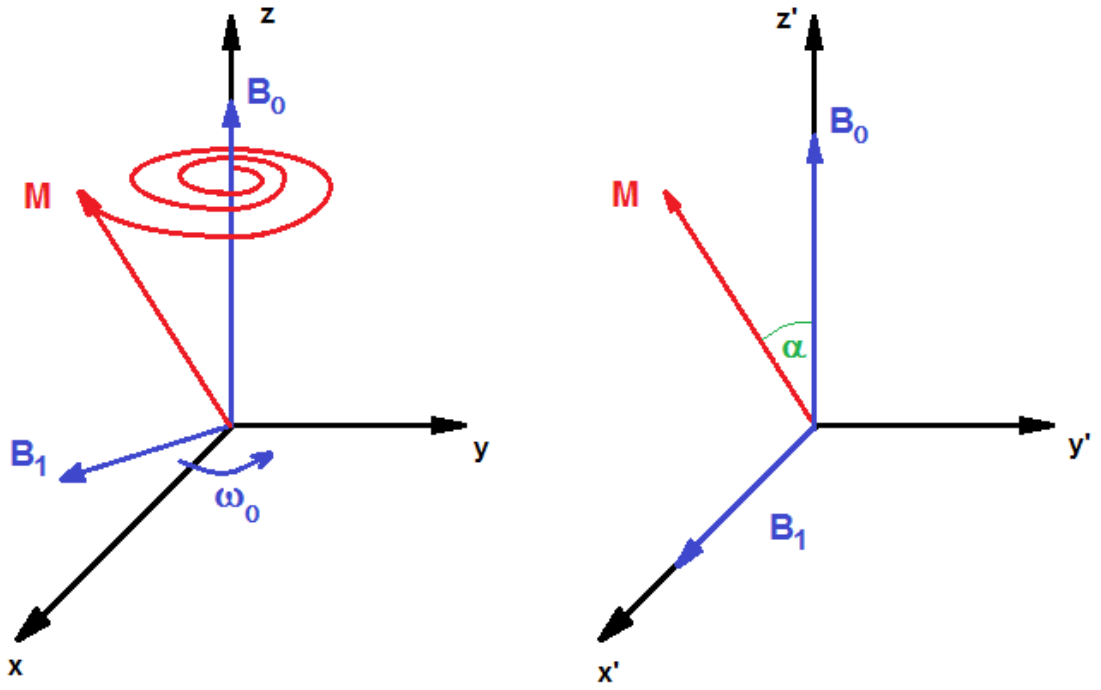

Figure 2.2: *Radiofrequency excitation. The net magnetization vector is flipped away from the z-direction by an RF-pulse applied at the Larmor frequency. Thus, the magnetization precesses around the B_{eff} vector in the laboratory frame (left). However, in the frame that is rotating at the Larmor frequency (right) B_1 appears stationary and the magnetization precesses around it with the flip angle α.*

2.1.6 Relaxation in a Magnetic Field

The simple solutions in the previous section only apply if the components of the magnetization do not interact with each other or exchange energy with their surroundings. However, in reality this is the case. Therefore, Felix Bloch extended the equations in 1946 by adding the relaxation terms [Bloch, 1946]:

$$\frac{d}{dt}M_x = \gamma(\mathbf{M}\times\mathbf{B})_x - \frac{M_x}{T_2}, \tag{2.31}$$

$$\frac{d}{dt}M_y = \gamma(\mathbf{M}\times\mathbf{B})_y - \frac{M_y}{T_2}, \tag{2.32}$$

$$\frac{d}{dt}M_z = \gamma(\mathbf{M}\times\mathbf{B})_z - \frac{M_z - M_0}{T_1}. \tag{2.33}$$

The above can be simplified separating the parallel and perpendicular magnetization

$$M_\perp = M_x + iM_y \quad \text{and} \quad M_\parallel = M_z. \tag{2.34}$$

In a homogeneous and static magnetic field in z-direction this leads to the following solutions

$$M_\perp = M_\perp(0)e^{i\omega_0 t}e^{-t/T_2} \tag{2.35}$$

$$M_\parallel = M_0 - (M_0 - M_z(0))e^{-t/T_1}. \tag{2.36}$$

The relaxation time T_1 and T_2 describe two separate physical processes. The T_1 relaxation describes how long the spin system takes to return to its thermodynamic equilibrium after a disturbance. The T_2 relaxation describes the decay of the magnetization perpendicular to the static magnetic field.

2.1.7 Spin-Lattice Relaxation

After a sample is placed in an external magnetic field the occupancy of the Zeeman levels is changed according to the Boltzmann distribution. By application of an RF pulse this equilibrium can be disturbed but it returns to the previous state afterwards. This redistribution comes from an interaction of the nuclei and its surrounding lattice and is characterized by the relaxation rate $R_1 = \frac{1}{T_1}$. R_1 depends on the rate at which systems can transfer energy to its surroundings [Becker, 1999].

The relaxation of a two state system can be explained by a simple probability outlook. Let n_0 be the total number of spins, n_+ and n_- be the number of spins on each energy level. W_+ and W_- the probability of upward and downward transitions between the levels. At thermal equilibrium these are balanced

$$W_+ n_- = W_- n_+. \tag{2.37}$$

Combining this with the information about the Boltzmann distribution

$$\frac{n_-}{n_+} = \exp\left(-\frac{\gamma\hbar B_0}{k_B T}\right), \tag{2.38}$$

and defining $W = (W_+ + W_-)/2$, while approximating the exponential function for the case $k_B T \gg \gamma\hbar B_0$, leads to two helpful expressions

$$\frac{W_+}{W} = 1 - \frac{\gamma\hbar B_0}{k_B T} \tag{2.39}$$

$$\frac{W_-}{W} = 1 + \frac{\gamma\hbar B_0}{k_B T}. \tag{2.40}$$

The relaxation of the system can be described by looking at the total change of the occupancy difference $n = n_- - n_+$

$$\frac{dn}{dt} = \frac{dn_-}{dt} - \frac{dn_+}{dt} = 2\frac{dn_+}{dt}. \tag{2.41}$$

Using the probabilities this can be calculated as

$$\frac{dn_+}{dt} = n_+ W_- - n_+ W_+. \tag{2.42}$$

Using equation 2.39 this leads to

$$\frac{dn}{dt} = -2W\left(n - n_0 \frac{\gamma\hbar B_0}{k_B T}\right). \tag{2.43}$$

This means the time constant T_1 is directly related to the probability of the transition between Zeeman levels and therefore dependent on B_0.

2.1.8 Spin-Spin Relaxation

After an excitation pulse all spins precess synchronously around the effective external magnetic field. This coherent spin movement results in a transverse or perpendicular magnetization. After a while the movement dephases and likewise the transverse magnetization decays. As the coherence of the movement is the deciding factor on how fast this decay occurs it is solely dependent on the interaction between the spins and not the interaction with the lattice. Spins interact among each other in various ways but one of the most important is the Brownian motion. Molecular movements alter the magnetic field around each spin and influence its nearest neighbors. These field changes lead to changes in the precession frequency and cause the characteristic dephasing. An additional effect to this process is caused by static field inhomogeneities. Therefore, the effective transverse relaxation time T_2^* is defined as

$$\frac{1}{T_2^*} = \frac{1}{T_2} + \frac{1}{T_2'}, \tag{2.44}$$

where T_2' is the part of the transverse decay caused by static field inhomogeneities.

Tissue	T_1 [ms]	T_2 [ms]
Gray matter	950	100
White matter	600	80
Muscle	900	50
Fat	250	60
Blood	1200	100-200
Lung	1300	50-60

Table 2.2: *Approximate relaxation values of tissues at* $1.5T$*. These values were taken from [Haacke et al., 1999] and [Wild et al., 2012]. The higher* T_2 *value for blood corresponds to arterial blood, the lower to venous blood.*

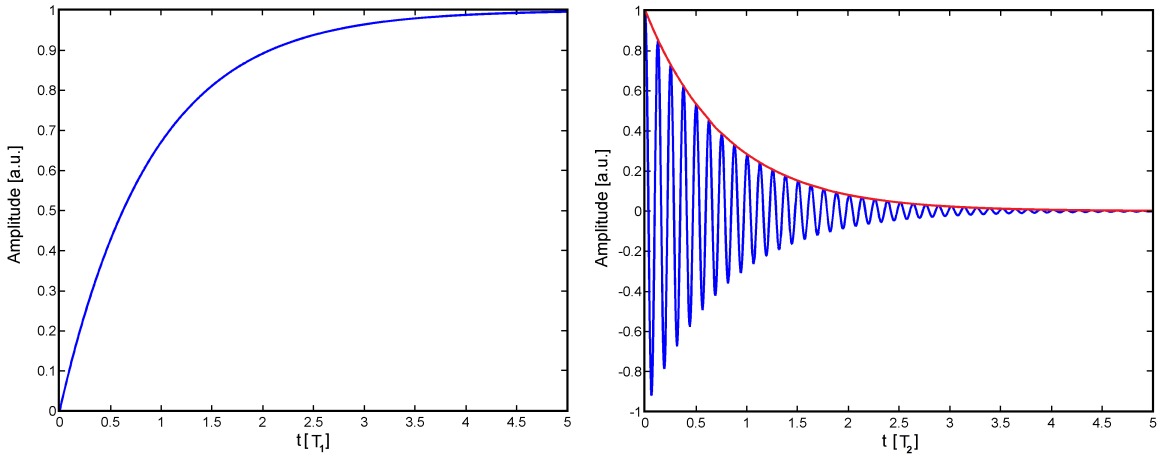

Figure 2.3: *Relaxation of the magnetization after excitation. Left: Recovery of the longitudinal component of the magnetization with the spin-lattice relaxation time* T_1 *after application of a* $90°$ *excitation pulse. Right: Temporal evolution of the real part of the measured signal (blue line) and decay of the transverse magnetization with the spin-spin relaxation time* T_2 *(red line).*

2.1.9 The NMR Signal

The following account is an abbreviation of [Haacke et al., 1999], which can be read for a complete derivation of the following formulas. After excitation of a sample the rotating transverse magnetization causes a magnetic current $\Phi(t)$. This magnetic current causes, based on Faraday's law of induction, a voltage given by

$$U_{ind}(t) = -\frac{d}{dt}\Phi(t) = -\frac{d}{dt}\int \mathbf{B}d\mathbf{S}. \tag{2.45}$$

The magnetic field **B** can be expressed as a rotation of the vector potential **A** and thus, the surface integral can be transformed into a line integral

$$U_{ind}(t) = -\frac{d}{dt}\int(\nabla \times \mathbf{A})d\mathbf{S} = \oint \mathbf{A}d\mathbf{l}. \tag{2.46}$$

As the transmit and the receive properties of a coil are identical the induced voltage can be calculated as

$$U_{ind}(t) = -\frac{d}{dt}\int \mathbf{B}_1(\mathbf{r})\mathbf{M}(\mathbf{r},t)d\mathbf{r}. \tag{2.47}$$

Using the expression from equation 2.35 and assuming that the measured NMR signal is proportional to the induced voltage, the signal is proportional to

$$S \propto \omega_0 \int e^{-\frac{t}{T_2(\mathbf{r})}} M_\perp(\mathbf{r})\mathbf{B}_\perp(\mathbf{r}) \sin(\omega_0 t + \Theta_B(\mathbf{r}) - \Phi_M(\mathbf{r}))d\mathbf{r}. \tag{2.48}$$

$\Theta_B(\mathbf{r})$ and $\Phi_M(\mathbf{r})$ resemble the starting phases of the perpendicular field $\mathbf{B}_\perp(\mathbf{r})$ and the perpendicular magnetization $M_\perp(\mathbf{r})$ respectively. To remove the fast modulation the signal is demodulated and in complex notation can be given as

$$S \propto \omega_0 \int e^{-\frac{t}{T_2(\mathbf{r})}} M_\perp(\mathbf{r})\mathbf{B}_\perp(\mathbf{r}) e^{i(\Theta_B(\mathbf{r}) - \Phi_M(\mathbf{r}))}d\mathbf{r}. \tag{2.49}$$

2.2 Magnetic Resonance Imaging

The idea to achieve imaging using a space resolved NMR signal was first published by Lauterbur in 1973 [Lauterbur, 1973]. He used field gradients overlaying the static B_0 field in all directions. Mathematically the gradients are given by

$$G(t) = (G_x(t),G_y(t),G_z(t)) = \left(\frac{\partial B_z(t)}{\partial x}, \frac{\partial B_z(t)}{\partial y}, \frac{\partial B_z(t)}{\partial z}\right). \tag{2.50}$$

By doing this the Larmor frequency is space resolved as well

$$\omega(\mathbf{r},t) = \omega_0 + \gamma \mathbf{G}(t)\mathbf{r}. \tag{2.51}$$

This dependence of the Larmor frequency is used in magnetic resonance imaging (MRI) to achieve its spatial resolution. In the following chapter the basic concepts of the magnetic field

gradients, as well as k-space are covered.

2.2.1 k-Space

After exciting the magnetization, it precesses with the Larmor frequency ω_0 around the effective magnetic field. If a gradient is active for the duration T, then the magnetization accumulates a phase $\phi(\mathbf{r})$. In the rotating coordinate system this phase can be calculated as

$$\phi(\mathbf{r}) = \int_0^T \omega(\mathbf{r},t)dt = \gamma\mathbf{r}\int_0^T \mathbf{G}(t)dt = \mathbf{k}(t)\mathbf{r}, \tag{2.52}$$

where $\mathbf{k} = (k_x(t),k_y(t),k_z(t))$ represents a point in k-space and is defined by the previous equation as

$$\mathbf{k} = \gamma\int_0^T \mathbf{G}(t)dt. \tag{2.53}$$

The space dependent phase adds an additional phase term in equation 2.49. The signal can now be described as

$$S \propto \omega_0 \int e^{\frac{-t}{T_2(\mathbf{r})}} M_\perp(\mathbf{r})B_\perp(\mathbf{r})e^{i(\phi(\mathbf{r})+\theta_B(\mathbf{r})-\Phi_M(\mathbf{r}))}d\mathbf{r} \tag{2.54}$$

$$= \omega_0 \int e^{\frac{-t}{T_2(\mathbf{r})}} M_\perp(\mathbf{r})B_\perp(\mathbf{r})e^{-i(\mathbf{k}(t)\mathbf{r}+\theta_B(\mathbf{r})-\Phi_M(\mathbf{r}))}d\mathbf{r}. \tag{2.55}$$

This can be simplified, with $\mathbf{M}_\perp(\mathbf{r}) = M_\perp(\mathbf{r})e^{i\phi_M(\mathbf{r})}$ and $\mathbf{B}_\perp(\mathbf{r}) = B_\perp(\mathbf{r})e^{i\theta_B(\mathbf{r})}$, while neglecting the T_2-relaxation

$$S = S(t) \propto \omega_0 \int \mathbf{M}_\perp(\mathbf{r})\mathbf{B}_\perp(\mathbf{r})e^{-i\mathbf{k}(t)(\mathbf{r})}d\mathbf{r}. \tag{2.56}$$

Assuming that the magnetic field $\mathbf{B}_\perp(\mathbf{r})$ is homogeneously distributed over the whole volume this leads to

$$S(t) \propto \int \mathbf{M}_\perp(\mathbf{r})e^{-i\mathbf{k}(t)(\mathbf{r})}d\mathbf{r}. \tag{2.57}$$

Equation 2.57 is the definition of the Fourier transformation [Fourier, 1822]. Thus, the MR-image $\mathbf{M}_\perp(\mathbf{r})$ can be calculated by an inverse Fourier transformation of the signal $S(t)$

$$\mathbf{M}_\perp(\mathbf{r}) \propto \int S(\mathbf{k}(t))e^{2\pi i\mathbf{k}(t)\mathbf{r}}d\mathbf{k}. \tag{2.58}$$

2.2.2 Spatial Encoding

In the following section spatial encoding is explained using a 2D MRI-experiment, which uses slice selection, phase- and frequency encoding.

Slice Selection

To achieve a signal from a two dimensional plane, first the magnetization of said plane has to be excited. This is achieved using an RF-pulse, while a magnetic field gradient is active. In the following explanation, without the loss of generality, the gradient is facing in z-direction. By using this gradient, the Larmor frequency is spatially resolved and thus, the resonance condition is only fulfilled in the desired slice. The thickness of the excited slice hereby is dependent on the bandwidth of the RF pulse and the strength of the gradient. This behavior is shown in figure 2.4. The bandwidth of the RF pulse is dependent on the Fourier transform of the pulse. For a sinc-pulse this is a rectangular function, thus its bandwidth can be changed by the duration of the pulse.

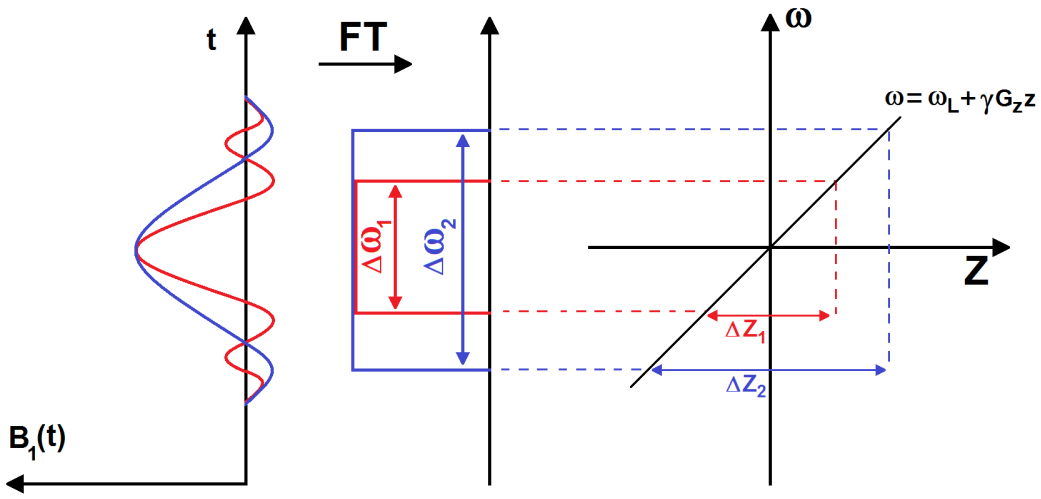

Figure 2.4: *Principal of slice selection. Using a magnetic field gradient in z-direction the resonance condition is only fulfilled in a slice perpendicular to the z-axis. Therefore, only a two dimensional slice is excited if an RF pulse is used while the gradient is active. The thickness of the excited slice is dependent on the bandwidth of the RF-pulse and the strength of the gradient.*

Phase Encoding

To achieve spatial encoding in the excited slice, the x and y directions also have to be encoded. This is done in the following manner. After the excitation of the slice, a gradient in y-direction

is used to change the accumulated phase depending on its position. This gradient is usually referred to as phase encoding gradient. Depending on the field of view and the resolution, the phase encoding step has to be repeated with different gradient strengths to sample the full k-space. The operation of the phase gradient is shown in figure 2.5.

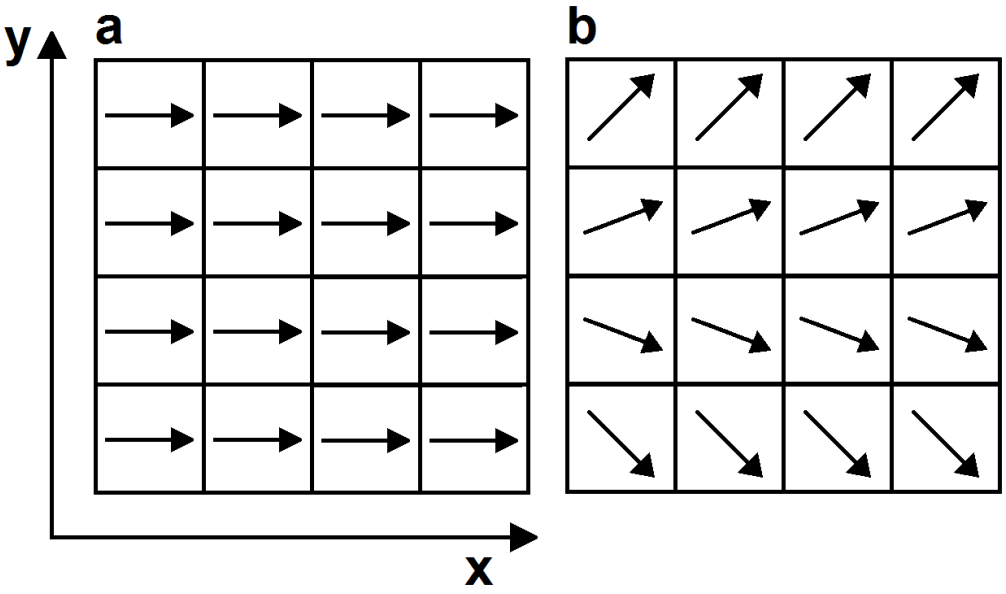

Figure 2.5: *Principal of phase encoding.* **a***: After the excitation by the RF-pulse the magnetization of each voxel has the same phase.* **b***: After using a gradient in y-direction each row in x-direction is in the same phase while each voxel in y-direction has a different phase.*

Frequency Encoding

To achieve encoding in the x-direction a gradient in x-direction is initiated at the same time as the measurement of the signal starts. This gradient is called frequency encoding gradient. Due to this gradient the Larmor frequency during signal acquisition is dependent on the position of the voxel in x-direction. The functionality of frequency encoding is shown in figure 2.6. Without a gradient during acquisition (**a**) the Larmor frequency in both objects is the same (**b**) and the spectrum of the object is a single peak (**c**). With a gradient during acquisition (**d**) the signal is comprised of different components (**e**) and the spectrum correctly shows the density of the spins in x-direction (**f**).

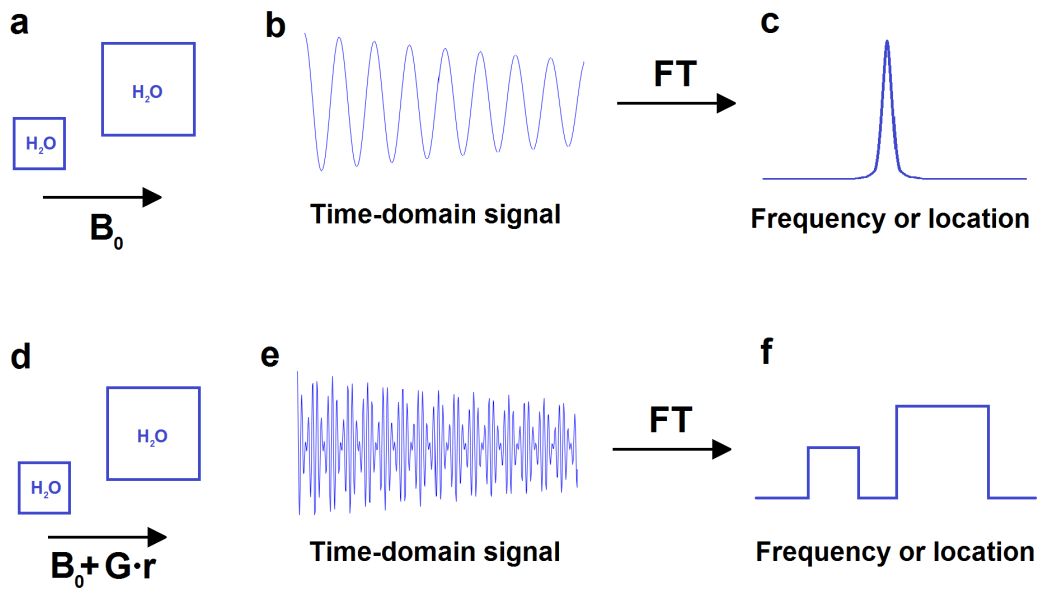

Figure 2.6: *Principal of frequency encoding. Without a gradient during acquisition (***a***) the Larmor frequency in both objects is the same (***b***) and the spectrum of the object is a single peak (***c***). With a gradient during acquisition (***d***) the signal is comprised of different components (***e***) and the spectrum correctly shows the density of the spins in x-direction (***f***).*

2.2.3 Imaging Sequences

Using the encoding techniques describes above the k-space can be measured by pulse sequences. These sequences are comprised of repeating RF-pulses and gradients. In this chapter the basic types of pulse sequences and their functionality will be covered.

Gradient Echo

Figure 2.7 shows a 2D gradient echo (GRE) sequence and the corresponding k-space trajectory. Gradient echo sequences are widely used for fast imaging. Its name is derived from the readout gradient dephasing the spins before the frequency encoding gradient forms the echo with opposite polarity. Thus, the echo usually occurs in the middle of the data acquisition. A multi-echo acquisition could be performed by adding more readout gradients to sample each k-space line with different echo times. To achieve 3D imaging an additional phase encoding gradient could be applied in slice direction. The images acquired by sequences of this type are T_2^*-weighted, due to the signal decay caused by magnetic field inhomogeneities. T_2 weighted images can be acquired using spin echo sequences, which are covered in the next section.

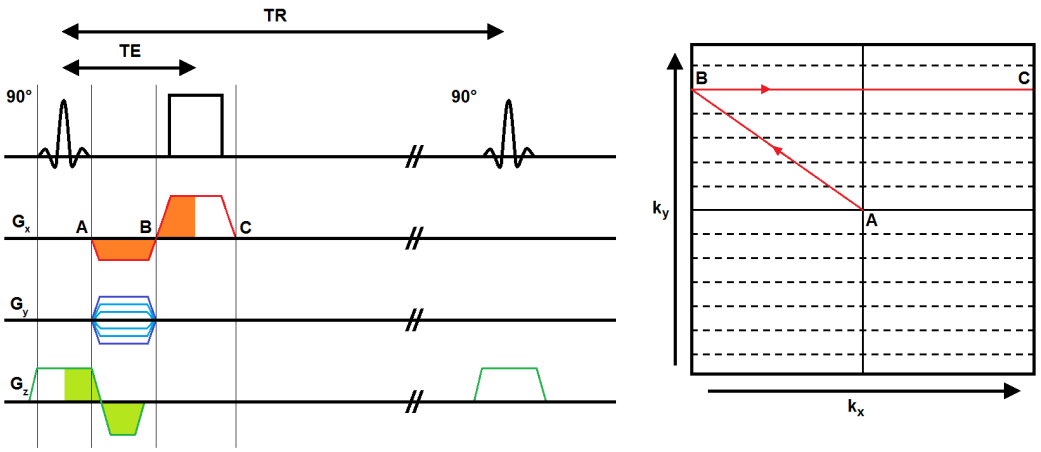

Figure 2.7: *2D gradient echo sequence (left) and corresponding k-space trajectory (right). After slice selection using the z-gradient (A) the x and y-gradients lead to point (B) in k-space. Here, the data acquisition starts with the application of the readout gradient and ends in point (C). The echo time TE occurs in the middle of data acquisition. Each repetition of the sequence acquires one line in k-space. The sequence is repeated after the repetition time TR until the required sections of k-space are sampled.*

Spin Echo

The concept of spin echoes (SE) is much older than the concept of k-space [Hahn, 1950]. It is the fundamental design that allows the acquisition of T_2 weighted images by refocusing all degradation effects. First, the magnetization is flipped into the xy-plane and dephases with the time T_2^*. However, after the application of an 180° pulse at the time TE/2 the signal is rephased and maximized at the echo time TE, eliminating all T_2^* effects. One problem spin echo sequences face are stimulated echoes. Thus, crusher gradients are employed near the refocusing pulse to destroy unwanted echoes. A 2D spin echo sequence and the corresponding k-space trajectory are shown in figure 2.8.

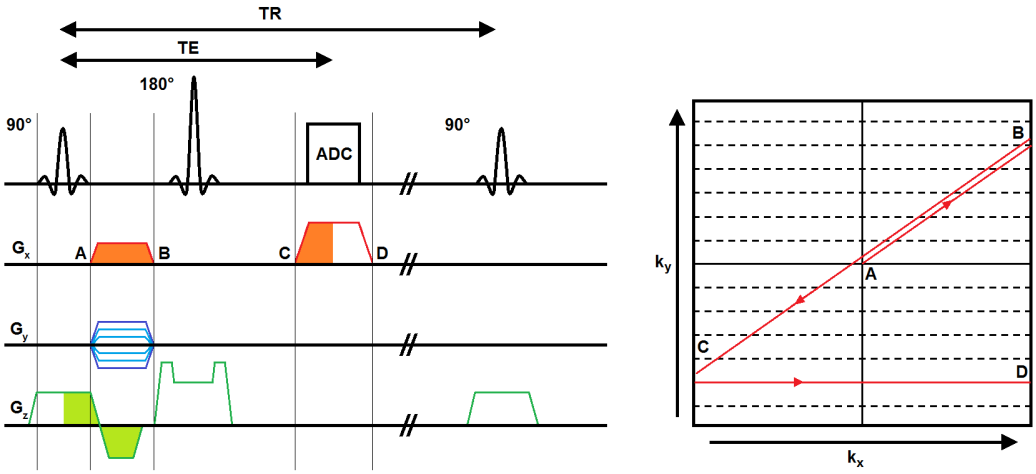

Figure 2.8: *2D spin echo sequence (left) and corresponding k-space trajectory (right). After slice selection using the z-gradient (A) the x and y-gradients lead to point (B) in k-space. Here, a 180° pulse is used to refocus the magnetization in point (C). The signal acquisition starts with the application of the readout gradient and ends in point D. The echo time TE occurs in the middle of the acquisition. Each repetition of the sequence acquires one line in k-space. The sequence is repeated after the repetition time TR until the required sections of k-space are sampled.*

Inversion Recovery

Inversion recovery sequences can be used to acquire T_1 weighted images. A 180° pulse is used to rotate the magnetization from the z-axis into the $(-z)$-axis. During the inversion time TI, the longitudinal magnetization recovers, before the excitation pulse flips it into the xy-plane. Due to tissue recovering at different rates, this can be used to acquire T_1-maps by fitting the data to

$$M_z(t) = M_0(1 - 2e^{-TI/T_1}). \tag{2.59}$$

Spoiler gradients are used to destroy the transverse components of the magnetization after the inversion. A 2D inversion recovery sequence is shown in figure 2.9.

2.2.4 Image Properties

Signal to Noise Ratio (SNR)

The signal to noise ratio (SNR) is defined as the ratio between the mean signal of the measured object and the mean signal of the background noise. The noise is the additional signal caused by random uncorrelated interactions of the magnetic moments, which is automatically added

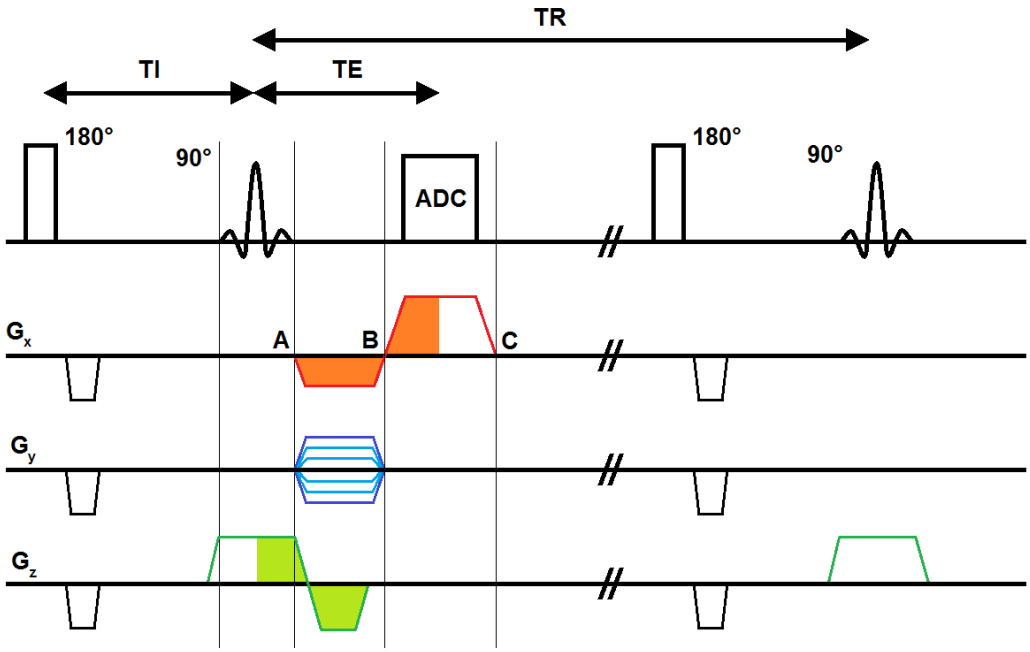

Figure 2.9: *Inversion recovery sequence. The magnetization recovers towards its equilibrium state after inversion and is flipped into the xy-plane after the delay time TI has passed. Thereafter, the readout begins to acquire the signal. The sequence is repeated after the repetition time TR until the required sections of k-space are sampled.*

to the actual signal. Statistical noise has a Gaussian distribution [Haacke et al., 1999] and is primarily caused by three independent processes. The measured object or patient causes intrinsic thermal noise due to the Brownian motion of the water molecules. The receive coil also causes noise due to free electron movement in its wiring. Additional to that, the amplifier system causes some additional noise, however in modern scanners the noise caused by this is small compared to the noise caused by the other two sources. In MRI the SNR of an object is measured within a region of interest (ROI). It can be calculated as

$$SNR = \frac{S}{N_R}, \tag{2.60}$$

where S is the mean signal of an object and N_R is the standard deviation of the noise in the specified region that only consists of noise [Weisskoff, 1996]. It is important to note, that the noise does not have Gaussian shape anymore after reconstructing the image via the Fourier transform. The contrast to noise ratio (CNR) between two objects is defined as the difference

of the corresponding SNR values

$$CNR_{A-B} = SNR_A - SNR_B. \tag{2.61}$$

There are some system parameters that influence the SNR. These are namely the voxel size V and the acquisition time T_{aq} [Haacke et al., 1999]

$$SNR \propto V\sqrt{T_{aq}}. \tag{2.62}$$

It is important to note that the acquisition time in this equation is not equal to the time of the measurement. Instead, it only refers to the time during which the signal is acquired. It is given by the following equation

$$T_{aq} = N_{PE}\tau_{ADC}, \tag{2.63}$$

where N_{PE} is the number of phase encoding steps and τ_{ADC} is the duration of the ADC. However, for almost all MRI sequences the duration of the measurement is directly proportional to the time during which signal is acquired.

Point Spread Function (PSF)

The point spread function (PSF) describes how the shape of a point in the measurement space is transformed in the image space. Using this the specific image properties of an MRI sequence can be analyzed [Rossmann, 1969]. The measured signal $S(k_x,k_y)$ can be described as the product of the idealized signal S_0 and a transfer-function $H(k_x,k_y)$

$$S(k_x,k_y) = S_0 \cdot H(k_x,k_y). \tag{2.64}$$

Using the most simplified case, where the object is a delta-function the PSF is the Fourier transform of the filter function

$$PSF = [\boldsymbol{FT}(H)](\boldsymbol{r}). \tag{2.65}$$

The PSF of an imaging sequence can be determined by measuring a homogeneous phantom without phase encoding. The PSF can then be calculated by using the inverse Fourier transformation of the raw data in phase encoding direction [Haacke et al., 1999].

Encoding Trajectories

Mathematically, the order in which the k-space is acquired is not specified. However these trajectories strongly influence the properties of the imaging sequence and in a worst case scenario can cause significant artifacts. The phase-encoding trajectory describes the order in which the acquisition steps are completed. That means a sequence of N phase encoding steps, that are taken at a time t_n are assigned to the N_{PE} amplitudes of the phase encoding gradient k_y in k-space,

$$PKT : t_n \rightarrow k_y = PKT(t_n) \quad (n = 1, ..., N). \tag{2.66}$$

The resulting PSF is given by

$$\overline{PSF}_n = [\boldsymbol{FT}(G(PKT_n))] \quad (n = 1, ..., N), \tag{2.67}$$

where t_n is the time at the nth echo and $G(t_n)$ are the corresponding weighting factors. This shows that the PKT is linked to the image properties. A continuous shape along the phase encoding direction is a requisite to achieve artifact-free imaging. Oscillation or jumps in the trajectory shape cause ringing and ghosting artifacts.

Properties of the Fourier Transform

As shown in the last segment, the acquisition of the signal is not continuous but discrete. Thus, the measured k-space points have a distance of $k = \gamma G \cdot t$. The discrete signal can be described as a continuous signal multiplied with Dirac delta functions

$$S_{discrete} = S(k) \cdot u(k) = S(k) \cdot \Delta k \sum_{n=-\infty}^{\infty} \delta(k - n\Delta k). \tag{2.68}$$

The function $u(k)$ is called Shah- or Comb-function [Bracewell, 1986]. The largest value for k (k_{max}) depends on the area of the gradient G. In the equation describing the measured signal S_M, k_{max} is expressed in the following manner

$$S_M(k) = S_k \cdot u(k) \cdot r(k), \tag{2.69}$$

with $r(k)$ as

$$r(k) = \begin{cases} 1 & \text{for} \quad -k_{max} \leq k \leq k_{max}, \\ 0 & \text{otherwise.} \end{cases} \tag{2.70}$$

As shown in equation 2.58, the MR image is the inverse Fourier transform of the measured signal. As such, the measured image is given by

$$M_M = \mathbf{FT^{-1}}[S_M(k)] = M(r) \otimes \mathbf{FT^{-1}}[u(k)] \otimes \mathbf{FT^{-1}}[r(k)], \tag{2.71}$$

where $M(r)$ is the distribution of the magnetization. As the structure of $u(k)$ and $r(k)$ are simple, the inverse Fourier transform can be solved analytically as

$$\mathbf{FT^{-1}}[u(k)] = \sum_{-\infty}^{\infty} \delta(r - \frac{n}{\Delta k}), \tag{2.72}$$

$$\mathbf{FT^{-1}}[r(k)] = 2k_{max} \cdot \mathrm{sinc}(2\pi k_{max} r). \tag{2.73}$$

The previous equations show that the resulting image is periodic and repeats with a factor of $1/\Delta k$. Therefore, the Nyquist-theorem [Nyquist, 1928] has to be fulfilled to ensure that repetitions of the measured objects are not part of the image. As such a suitable field of view (FOV) has to be chosen that limits the distance of two k-space points to the reciprocal value of the FOV

$$\Delta k \leq \frac{1}{\mathrm{FOV}}. \tag{2.74}$$

Thus, the resolution of the measured image depends on the maximum value of k-space (k_{max}). As small objects are mapped by the sinc-function, the resolution is defined as the full width of the main maximum at half intensity. This corresponds to the reciprocal value of the maximum value of k-space

$$\Delta r = \frac{1}{2k_{max}}. \tag{2.75}$$

Properties of k-Space

A direct result of properties of the Fourier transform for image reconstruction are the properties of the different k-space areas. The contrast or intensity of the image is described by the low-frequency lines in k-space. These are situated in the center of k-space. The outer k-space lines determine the sharpness or resolution of the image. In figure 2.10 the influence of different

k-space regions is shown.

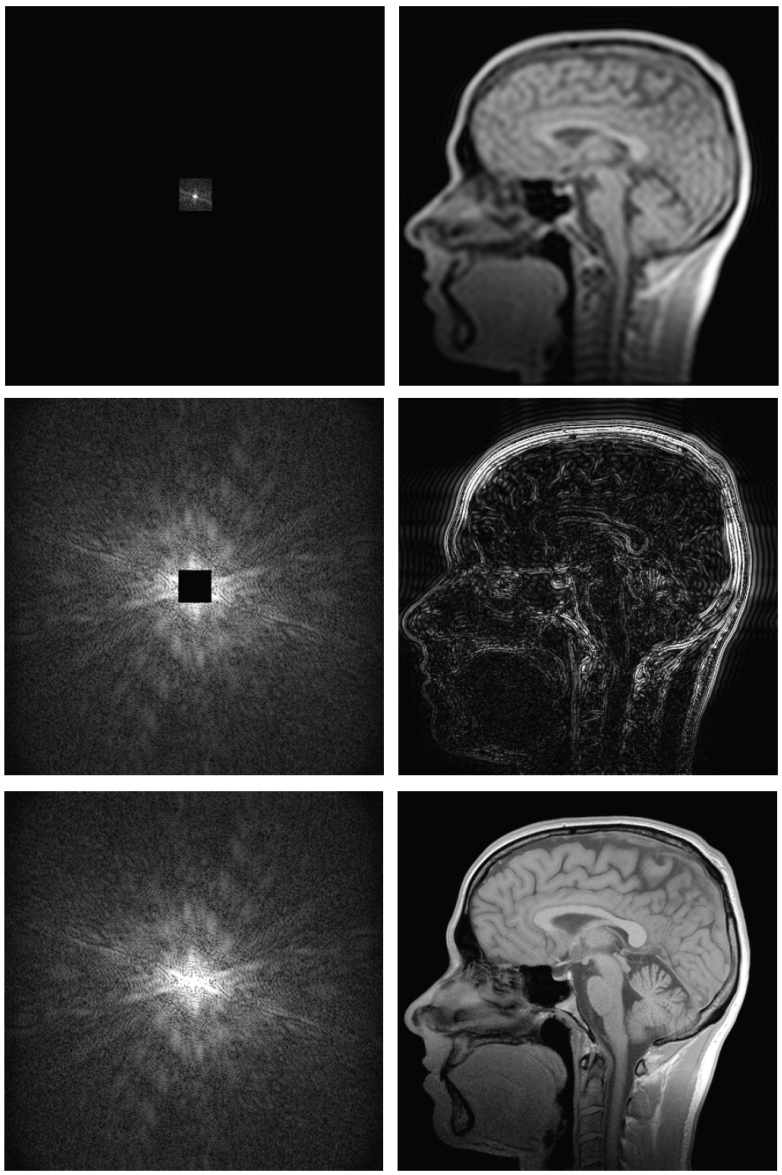

Figure 2.10: *Illustration of the properties of k-space. The left column shows which points in k-space were used to reconstruct the corresponding image in the right column. In the first row only the center of k-space is used. In the second row only the periphery of k-space is used. And in the third row the fully sampled k-space is used for comparison.*

2.2.5 Hardware Components

The most important components of an MR-Tomograph are the main magnet, the gradient system, the RF excitation system, including various body coils, and a computer used for image reconstruction. These parts and their most important properties will be covered in the

next section. A more thorough description can be found in [Haacke et al., 1999].

Main Magnet

The static magnetic field is produced by a superconducting coil, which is surrounded by a cryostat cooled by liquid helium. The coil is made up of NbTi filaments embedded in a copper matrix to increase flexibility. Currently, for clinical applications, magnets with a strength between 0.2T and 3.0T are common. For research, human scanners of up to 9.4T are in use for MRI. To achieve an image without artifacts it is paramount that the magnetic field within the imaged area is extremely homogeneous. The homogeneity of an unloaded tomograph with a bore diameter of 50 centimeters is commonly around 30ppm. To reduce the heterogeneity further, both passive and active shim coils are installed in the scanner. Using these the in-homogeneity in the bore can be brought down to around 1ppm. However, any kind of load (human subjects or phantoms) increases the in-homogeneity again, due to their own intrinsic heterogeneity. Thus, it is important to use the active shim coils before each measurement and optimize the homogeneity in the imaged area. If done correctly, this brings the in-homogeneity within the sample back down to between 1 and 2 ppm.

Gradient System

The gradient fields used for encoding are produced by another set of coils usually referred to as the gradient system. As explained in the previous chapter the resolution of an MR-image is proportional to the strength of the gradients. Thus, to increase the imaging speed, while keeping the resolution constant, a stronger and also faster gradient system is required. For these reasons, fast pulse sequences also require a modern gradient system. A gradient system can be defined by two parameters. The amplitude describes its maximum strength and the slew-rate describes its changing speed. Scanners used in the clinical routine usually have a gradient strength of $G_{max} = 40mT/m$ and a slew-rate of $200T/m/s$. Using Faradays law, changing magnetic fields introduce eddy currents, which reduce the effect of the gradient coils. These eddy currents skew the field produced by the gradient system. Therefore, modern gradient systems have a complicated form in order to compensate for such degradation effects. Additionally, strong and fast gradients introduce electric fields in human patients. These fields can lead to nerve stimulation and sudden muscle contractions. Thus, the stimuli caused by

the gradient system is always watched by intrinsic security systems in the scanner, which will abort the scan immediately if certain thresholds are violated. The gradient system also causes the loud noise that is characteristic for an MR scan. The noise is caused by the Lorentz forces, which are induced by the field switches and can reach up to 100dB. Therefore, patients should always wear noise protection during examination.

RF-System and Body Coils

The RF-system and the body coils used in MRI have two main objectives. Firstly, they produce the RF-pulses necessary to excite the magnetization (the transmit function). And secondly, they also measure the signal induced by the magnetization (the receive function). The integrated whole body coil in any MR scanner can be used to perform both tasks but surface coils, specifically tailored to certain sections of the body, offer a much higher signal to noise ratio (SNR).

Computer System

The adjacent computer system connected to each MR scanner is used as user interface and to control the scanner. It has to perform three separate processes. The first process synchronizes and controls the hardware components of the scanner. The second process reconstructs the image from the measured data and the third process hosts all the programs needed by the user to perform the measurement and evaluate the results.

Specific Absorption Rate (SAR)

In certain imaging sequences many RF-pulses with high flip angles are used in a short timeframe. The $B_1(t)$-field, which excites the spins, also generates an electric field $E_1(t)$ as described by the Maxwell equations. This electric field then causes eddy currents in the examined patients. The currents in turn heat up the patients and can lead to injuries if not restricted correctly. The part of RF-energy, that is absorbed by the human body and thus, causes the patients to heat up, is described by the specific absorption rate (SAR). The scanner automatically calculates the value before any measurements, using the patients weight and the examined region of the body. The European community specified that a temperature increase of $1K$ should not be harmful to any patient. Thus, the general limitations of $4W/kg$ for ex-

amining parts of the human body and $0.04W/kg$ for whole-body examinations were specified. The physical properties that influence the power absorbed by the patient are the following

$$P \propto \frac{\sigma\omega^2\alpha^2}{\gamma^2\tau_{RF}^2}, \tag{2.76}$$

where $\alpha = \gamma \int_0^{\tau_{RF}} B_1(t)dt$ is the flip angle. Thus, the specific absorption rate is proportional to the square of the field strength of $B_1(t)$. In turn, the limitations induced on your measurement sequences by SAR get much more serious at higher field strengths, such as $3T$ and $7T$.

2.3 The Human Lung

The organ of interest in this work is the human lung. Therefore, it is important to give an introduction to its anatomy, physiology and pathology. However, this is just a basic overview. For a more complete coverage please refer to [Ganong, 2005] or [West, 2008].

2.3.1 Anatomy of the Lung

The function of the lung is to bring air in and out of the body. The organ is separated into three sub-systems which differ in size or function. These sub-systems are, the upper airways (mouth, nose, pharynx, trachea), the lower airways (bronchi, bronchioles, alveoli) and the respiratory muscles (diaphragm, intercostal muscles). While all of these systems are vital for respiration the focus of this work will be on the lower airways, since imaging, such as MRI, CT or PET focuses on finding defects inside the lung. The purpose of the lung is gas exchange and its anatomy reflects that. The exchange of oxygen and carbon dioxide is controlled by diffusion. The direction of the gas exchange is guided by Ficks law, which states that the amount of gas that moves across a sheet of tissue is proportional to the area of the sheet and inversely proportional to its thickness [West, 2008]. Nature has optimized this process by making the barrier between blood and gas very thin (around $2\mu m$) and its surface area very large ($50 - 100m^2$). The large surface area is achieved by using an extremely high number of small air sacs, called alveoli. Each of these is perfused by small capillaries, that are wrapped around them. The lung of an adult human hosts around 300 million alveoli with a diameter of around $0.3mm$ each. The transition of the upper airways, starting with the trachea, and the lower airways, is achieved by a series of branching tubes which narrow up with each time they

split. Each split is called a generation and assigned a number with the trachea being specified as generation 0. During the first 16 generations no gas exchange is taking place. Thus, the area is referred to as conducting zone or anatomically dead zone. This area, which commonly takes up around $150ml$ only serves the purpose to bring gas into the respiratory zone, where the gas exchange takes place. During inspiration the volume of the lung expands due to the diaphragm contracting, moving downwards and therefore expanding the thorax. Due to this expansion there now is a downward pressure gradient that forces air into the lungs. This process is reversed during expiration. As the lung volume is shrinking, air is pushed out of the lung. The perfusion of the lung is handled by the right ventricle of the heart. The pulmonary artery carries the deoxygenated blood to the lungs and after gas exchange the newly oxygenated blood is transported through the venial system to the left atrium of the heart. An idealized representation of the anatomy of the respiratory system is shown in figure 2.11.

2.3.2 Physiology of the Lung

While the lung has other minor functions, this section will primarily look at the gas exchange, which is its main function. Gas exchange only occurs in the alveoli, where O_2 is added and CO_2 is removed. It depends on two separate physiological processes, the blood flow through the capillaries of the lungs (perfusion) and fresh air reaching the alveoli (ventilation). The perfusion of the lung is handled by the right chamber of the heart, which pumps deoxygenated blood into the lungs through the pulmonary artery. This main vessel then branches out into smaller vessels until finally reaching the capillaries wrapped around the alveoli. Here the blood is oxygenated. The perfusion of an average healthy adult human at rest is roughly $3.5L/min$. Due to the dead space in the lungs, which does not contribute to gas exchange, ventilation is split into two parameters. Minute ventilation measures the total amount of gas which enters the lung, whereas alveolar ventilation only describes the fraction that actually reaches the alveoli. To achieve optimal gas exchange both ventilation and perfusion have to match. Thus, the ventilation to perfusion ratio (V/Q - ratio) is an important bio-marker to rate the functionality of lung tissue. The V/Q - ratio of healthy subjects is in the range of $0.8 - 1.0$ [Dean, 1985]. To understand ventilation one has to classify different stages and volumes of the breathing cycle of a human. The most basic is the total lung capacity, which is on average $6L$ for men and $4.2L$ for women. However, these values are never reached in a regular breathing

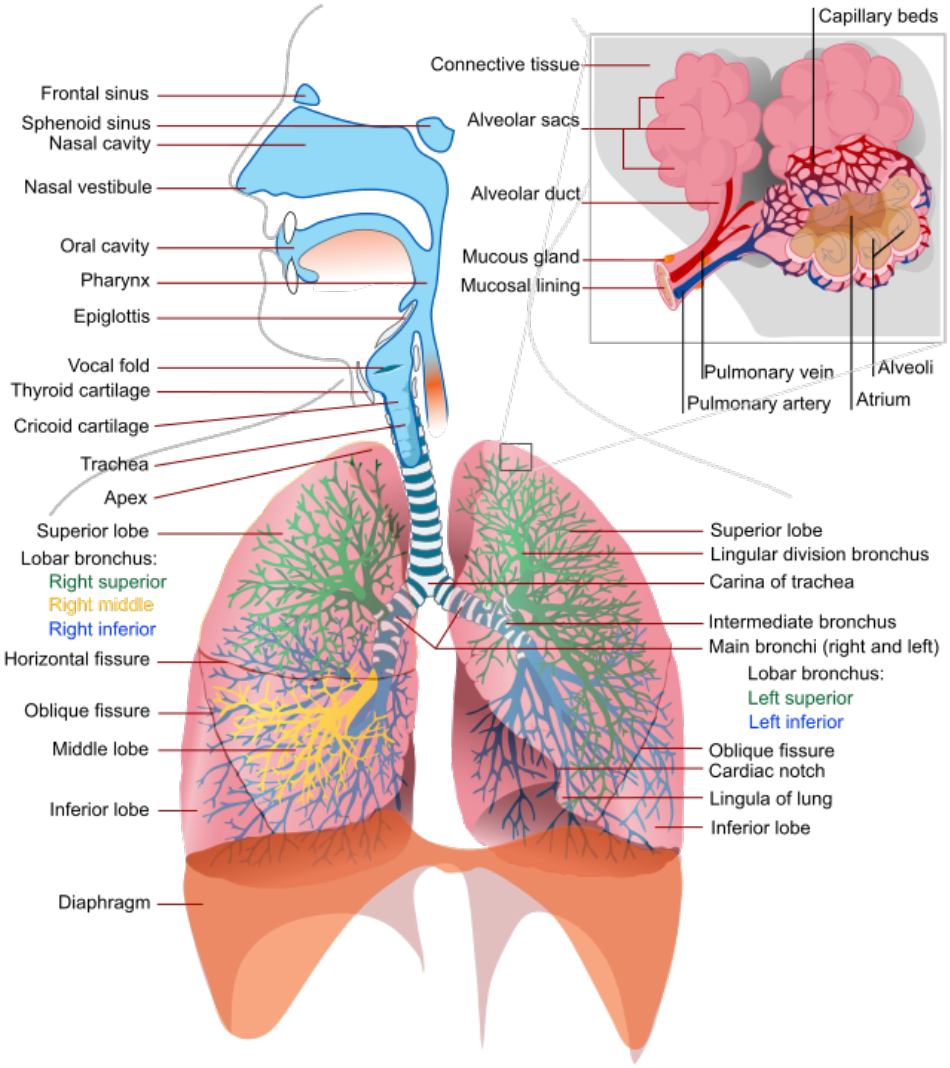

Figure 2.11: *Anatomy of the respiratory system. Source: Wikimedia Commons*

cycle at rest. The volume that is inhaled and exhaled during normal breathing is known as tidal volume and is only about $500ml$ per breath. Even when inhaling and exhaling as much as possible the total lung capacity can never be reached as there is always a residual volume left in the lung to prevent it from collapsing. The residual volume is about $1.2L$ for men and $1.1L$ for women. Measuring the functionality of the lung is usually done by spirometry, which measures the airflow during breathing. The most common test is the measurement of the forced vital capacity (FVC) and the forced expiratory volume in one second (FEV1). These two parameters are then combined into the FEV1/FVC - ratio and compared to literature values based on age, sex, height and weight of the subject. Other common spirometry tests include the forced expiratory and inspiratory flow (FEF and FIF) and the peak expiratory

flow (PEF). However, there are a plethora of other spirometry tests which are used depending on different symptoms and can be found in the relevant literature. While most parameters of the lung can be measured directly some are only measurable indirectly. The residual volume is such a case. To measure these parameters measurements using plethysmography or gas washouts are used. One of the more interesting features of the lung is its large dependence on gravity [Bryan et al., 1966]. Due to the top of the lung resting on the bottom, the lower parts of the lung are compressed. This influences not only the morphology of the lung but also the physiology (e.g. perfusion and ventilation). As such, standing up or lying down greatly influences the functionality of the lung. Thus, it is of utmost importance to always ensure that experiments are performed with the patients in the same position.

2.3.3 Pathology of the Lung

There is a wide range of problems that can occur in the human lung. This section will cover the most common ones and include a short description of their basic influence on the physiology of the lung.

Lung Cancer

Lung cancer is the most common cancer worldwide [Ferlay et al., 2010] and the leading cause of cancer related deaths in the USA [Humphrey et al., 2013]. Imaging such as CT plays a vital role in the detection and diagnosis of these types of cancers. As with cancer in most organs, lung cancers have a large variance in type and manifestation [Rami-Porta et al., 2009], but all share the uncontrolled cell growth. While tumors almost always restrict ventilation in the afflicted part of the lung, they can both be heavily perfused or restrictive perfused. As such the V/Q-ratio is important to determine the type of cancer.

Chronic Obstructive Pulmonary Disease

Chronic Obstructive Pulmonary Disease (COPD) is a common cause of death worldwide with rapidly growing prevalence [Gulsvik, 2001]. It is defined as preventable and treatable disease that induces persistent airflow limitations associated with an enhanced chronic inflammatory response to noxious particles. COPD is mainly caused by cigarette smoking but other factors such as environmental pollution or genetics also play a role in its prevalence. While COPD

is usually diagnosed by standard spirometry tests such as FEV1, imaging can play a role in identifying affected regions and applying localized treatment. As such hyperpolarized gas MRI of the lung has shown good promise in visualizing ventilation defects [Fain et al., 2007].

Cystic Fibrosis

Cystic fibrosis (CF) is a genetic disease which is common among people of Caucasian descent. Around 0.05% of all newborn are afflicted [Wood et al., 1976]. CF restricts the clearance of the lungs, which causes clogging of airways and inflammation based on the build up mucus. Similar to COPD, CF is usually diagnosed by global spirometric measurements. However, imaging could yield regional information about the severity and the progress of the disease and would be much preferable. As CF is a life-long disease, imaging based on radiation (e.g. CT) is largely inhibited. However, MRI was recently shown to be comparable to CT in detecting morphological changes in cystic fibrosis [Puderbach et al., 2007].

Pulmonary Hypertension

Pulmonary hypertension is defined as an increase in pulmonary arterial pressure [Rich et al., 1987]. It can lead to heart failure and subsequently death. There are many conditions that can lead to pulmonary hypertension and a correct classification of the disease and its stages is of paramount importance to ensure an appropriate treatment. V/Q-imaging has been shown to be able to accurately classify pulmonary hypertension caused by pulmonary embolism [He et al., 2012] and as such could help greatly with a classification of the disease.

Asthma

Asthma is a chronic disease characterized by reversible airflow obstructions due to inflammation. Both genetic and environmental risk factors have been identified [Martinez, 2007] and symptoms can vary greatly. Imaging so far has not played a role in the detection or treatment of asthma, but recent development has shown great promise for hyper-polarized gas MRI to detect both defects and changes [Samee et al., 2003].

3 Materials and Methods

3.1 MR Hardware and Software

Hardware

All measurements were conducted on a 1.5T whole body system by Siemens (Magnetom Avanto, Siemens Healthcare, Erlagen, Germany). Using the gyromagentic ratio of protons ($\gamma = 42.58\frac{MHz}{T}$) this leads to a Larmor frequency of $\omega_0 = 63.87MHz$ at 1.5 Tesla. The gradient system reached a maximum amplitude of $40\frac{mT}{m}$ in both x- and y-direction perpendicular to the main magnetic field B_0. In the z-direction, parallel to the main magnetic field $45\frac{mT}{m}$ were usable. The maximum slewrate of the gradient system was limited to $180\frac{mT}{m \cdot ms}$ in x- and y-direction, and $220\frac{mT}{m \cdot ms}$ in z-direction. These limitations are in place to prevent peripheral nerve stimulation [Reilly, 1989]. For all measurements, including both the sponge and the porcine phantom, a flexible 6-channel body coil array and the 6-channel spine array build into the patient table were used. All measurements of human volunteers and patients were performed head first and in supine position.

Software

The manufacturer's software framework for pulse sequences (IDEA, Siemens Healthcare, Erlangen, Germany) was used to implement and modify the imaging sequences. The image reconstructions were also done using the manufacturer's framework for image reconstruction (ICE, Siemens Healthcare, Erlangen, Germany). All further postprocessing and image analysis was done in MATLAB (MathWorks, Natick, MA, USA).

Figure 3.1: *1.5T Siemens Magnetom Avanto. Image courtesy of Åsmund Kjørstad.*

3.2 Phantoms

The phantoms used to test and validate the techniques described in this work will be covered in this section.

3.2.1 Sponge Phantom

Due to their structural similarities sponge phantoms are commonly used to simulate lung tissue [Zapke et al., 2006] [Molinari et al., 2014]. The phantom used in this work was created in-house to facilitate specific needs. A picture of the phantom can be seen in figure 3.2. The size of the cubic sponge was $10 \times 25\ cm^2$. The plastic straws had a diameter of 5 and 15 mm, respectively. The sponge phantom was filled with a mixture of water and contrast agent to achieve similar T_1 and T_2 times to the lung parenchyma. Before and after each measurement cycle, the relaxation times were measured to ensure stable conditions.

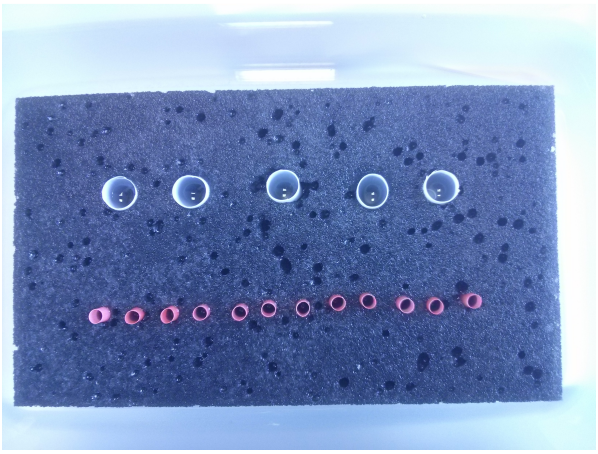

Figure 3.2: *Sponge phantom. The sponge is impaled with two rows of plastic straws. The white straws have a diameter of 15 mm, the red straws have a diameter of 5 mm.*

3.2.2 Porcine Phantom

Ex-vivo measurements were performed on a thorax phantom (ArtiCHEST, PROdesign GmbH, Heiligkreuzsteinach, Germany) holding a excised, preserved porcine lung (Lung Demonstration Model R10060, Erler-Zimmer GmbH & Co. KG, Lauf, Germany). The container included an artificial diaphragm to simulate a breathing cycle [Biederer et al., 2006]. In figure 3.3 a picture of the phantom is shown. The double-walled shells can be filled with liquid to simulate the chest wall. The excised porcine lung is attached to a pipe connected to the room air. Using a vacuum pump to evacuate the container the lung can be inflated, while an additional diaphragm pump controls the degree of inflation by expanding or contracting the artificial diaphragm. For this work a simulated free breathing cycle with a frequency of 10 breaths per minute with a sinusoidal amplitude was used.

Figure 3.3: *Ex-vivo porcine phantom. Thorax phantom containing an excised porcine lung attached to a vacuum pump. Image courtesy of Jascha Zapp.*

3.3 Special Sequence Techniques

In the following section two important sequence techniques will be explained that will be used in this work. The first is the parallel acquisition technique implemented in Siemens MRI, called GRAPPA. The second is a technique to optimize the SAR compatibility of radio frequency pulses called VERSE.

3.3.1 Parallel Acquisition (GRAPPA)

Parallel acquisition techniques are used to accelerate image acquisition. While there are many different techniques, they all dependent on coil arrays simultaneously acquiring data with several receive coils. Using the spatial information contained in the sensitivity of each coil the standard encoding with field gradients can be replaced. One of these techniques is GRAPPA [Griswold et al., 2002]. GRAPPA accelerates image acquisitions by only acquiring every R^{th} k-space line, where R is called the acceleration or under-sampling factor. The signal of the missing lines is then reconstructed using the linear combination of the signal acquired by each single coil. Mathematically this can be written as

$$S_j(k_y - m\Delta k) = \sum_{l=1}^{L} \sum_{b=0}^{N_b-1} n(j,b,l,m) S_l(k_y - bR\Delta k). \tag{3.1}$$

S_j is the signal of the unknown line, S_l the signal of the different coils, n the specific weighting factor of each coil and N_b the number of lines used for the reconstruction. The index m, l and b count through the missing lines, the coils and the lines used for reconstruction, respectively. An illustration of the reconstruction process can be seen in figure 3.4. The weighting factors required to calculate the reconstructed signal are determined using additional auto-calibration lines (ACS), which are acquired separately at the center of k-space. All ACS lines are fitted using adjacent lines of all different coils. Using the ACS lines, the missing lines for a specific coil can be reconstructed. The image for each coil can then be obtained normally by the Fourier transform. Images for each coil are created in this manner and afterwards combined. The most common combination mode, which was also used in this work, is the the sum of squares method [Roemer et al., 1990].

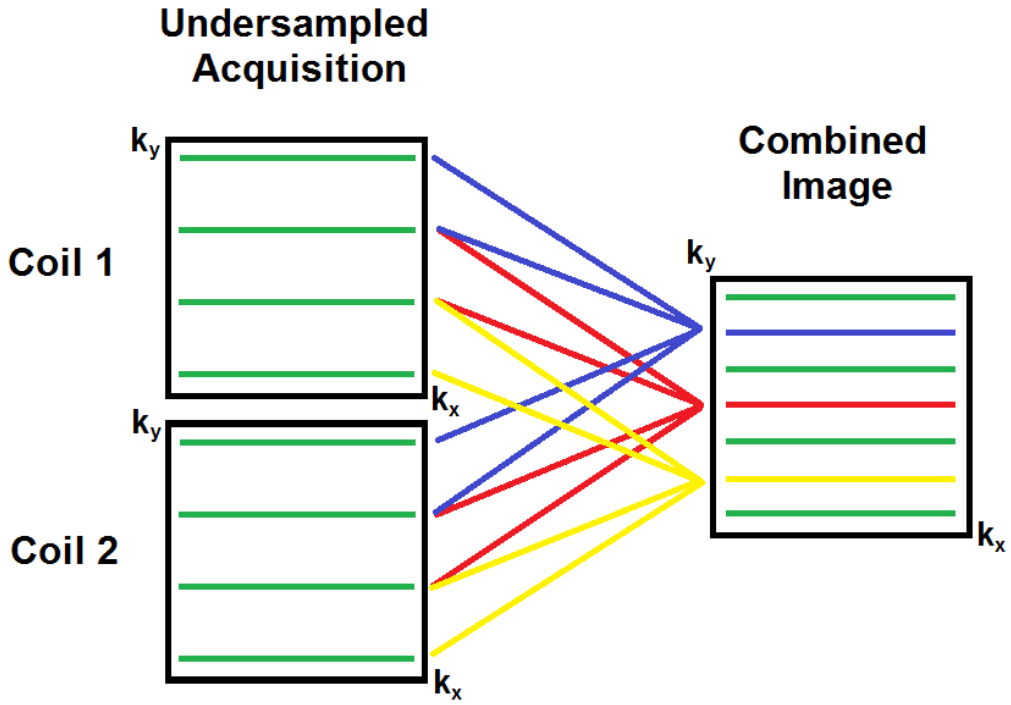

Figure 3.4: *GRAPPA reconstruction. Schematic reconstruction of three k-space lines (blue, red, yellow) for a Cartesian acquisition with an acceleration factor $R = 2$. The image is reconstructed using two coils and two adjacent lines each.*

3.3.2 Variable-Rate Selective Excitation (VERSE)

The reshaping of RF-pulses to reduce SAR constraints for bSSFP sequences was developed by [Hargreaves et al., 2004]. He proposed an algorithm that optimized a previously designed pulse by computing both a new amplitude waveform and a new waveform for the slice selection gradient. Due to the lower peak amplitude, the new pulse produces significantly lower SAR while the excitation is the same as the original pulse. As both the amplitude and the slice selection gradient vary in time, the method was called variable-rate selective excitation (VERSE).

The general principle behind the VERSE approach is based on the relationship of the Larmor frequency to the magnetic field strength. The effective field $\mathbf{B}_{eff}$ determines both the axis and the angle Φ of the magnetization during an RF-pulse. $\mathbf{B}_{eff}$ on the other hand depends on the local gradient $G(t)$ and the alternating field $B_1(t)$. Splitting the rotation into small time

frames dt, in which the effective field does not change, the rotation can be written as

$$d\Phi = \gamma|\mathbf{B}_{eff}| \cdot dt. \tag{3.2}$$

If each of these temporally constant rotations is matched by the new pulse design, the end product of all of them also remains unchanged. Thus, the profile of both the original and the modified excitation would match. As the net rotation is the only variable that has to remain the same, the single rotations can be varied as one sees fit. Mathematically this principle can be confirmed by the Bloch equations, which state for slice selection in z-direction

$$\frac{d}{dt}\mathbf{M}(t,z) = \mathbf{M}(t,z) \times \gamma\mathbf{B}_{eff}(t,z). \tag{3.3}$$

The magnetization vector is denoted by $\mathbf{M}$ and the effective magnetic field $\mathbf{B}_{eff}$ is determined by the excitation field and the gradient G

$$\mathbf{B}_{eff} = (B_x,B_y,G \cdot z). \tag{3.4}$$

Defining a time-dilation waveform $\tau(t)$ with $\frac{d}{dt}\tau > 0$ and a modified magnetization vector $\mathbf{m}(t,z) = \mathbf{M}(\tau(t),z)$, the Bloch equations modify to

$$\frac{d}{dt}\mathbf{m}(t,z) = \frac{d}{dt}M(\tau,z)\frac{d}{dt}\tau(t) \tag{3.5}$$

$$= \mathbf{m}(t,z) \times \gamma\mathbf{B}_{eff}(\tau(t),z)\frac{d}{dt}\tau(t). \tag{3.6}$$

This means that the modified magnetization is excited by the same profile if

$$\mathbf{B}_{eff} = \mathbf{B}_{eff}(\tau(t),z)\frac{d}{dt}\tau(t). \tag{3.7}$$

This equation is called the continuous-time variable rate theorem. Commonly the derivative of the time-dilatation is interpreted as a scaling function

$$\tau(t) = \int_o^t s(t')dt'. \tag{3.8}$$

Using this, VERSE transformed versions of the magnetic field and the slice selection gradient

are given by

$$B_{VERSE}(t) = s(t)B(\tau(t)) \tag{3.9}$$

$$G_{VERSE}(t) = s(t)G(\tau(t)). \tag{3.10}$$

Generally the length of the RF-pulse is not conserved by these relations. To achieve pulses of a similar length, an additional constraint has to be fulfilled

$$\tau(T_{pulse}) = T_{pulse}. \tag{3.11}$$

3.4 Signal States

Steady-state sequences have two different signal phases. The transition from thermal equilibrium to a state where the signal is constant is called transient phase. The phase in which the signal does not change anymore is referred to as the steady-state.

3.4.1 Transient Phase

Most steady-state sequences feature large signal oscillations in the transient phase. An example for such signal oscillations can be seen in figure 3.5. The transient phase of most steady-state sequences it quite long. For the balanced steady-state free precession (bSSFP) sequence used in this work it is commonly between 100-200 pulses depending on the T_1 of the tissue.
While shortening the transient phase and thus reaching the steady-state any faster is generally not possible, the reduction of the signal oscillations during it, is relatively simple using a preparation. The most basic preparation is an $\alpha/2$ pulse, which is applied $TR/2$ before the actual sequence starts [Deimling and Heid, 1994]. While such a simple preparation is not able to remove the oscillations completely, it will neutralize the most obvious ghosting artifacts caused by it. An example image with an unprepared bSSFP sequence and a sequence prepared with an $\alpha/2$ pulse can be seen in figure 3.6.
Mathematically the signal intensity during the transient phase can be calculated in the following way [Hargreaves et al., 2001]

$$M_n = (\sin(\alpha/2)M_0 - M_{SS})\lambda^n + M_{SS}. \tag{3.12}$$

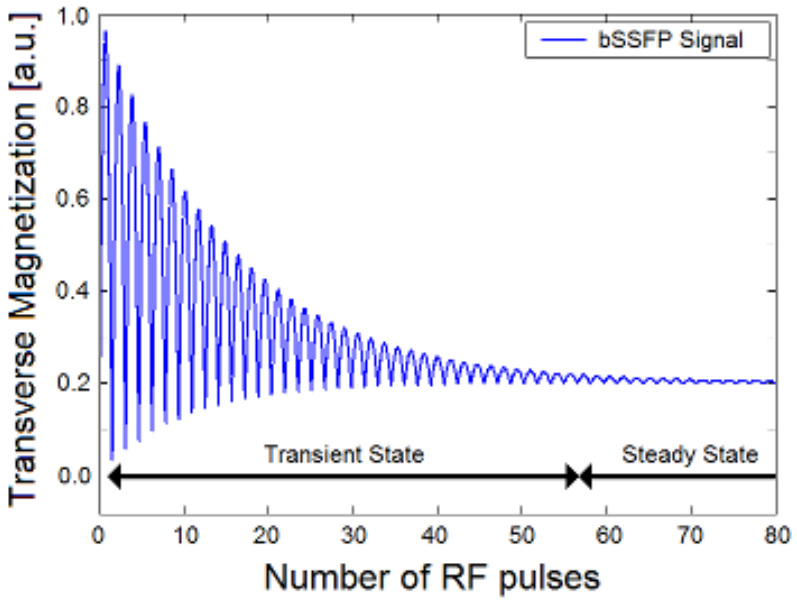

Figure 3.5: *Signal progression of a bSSFP sequence. The large oscillations during the transient state can be minimized by sufficient signal preparation.*

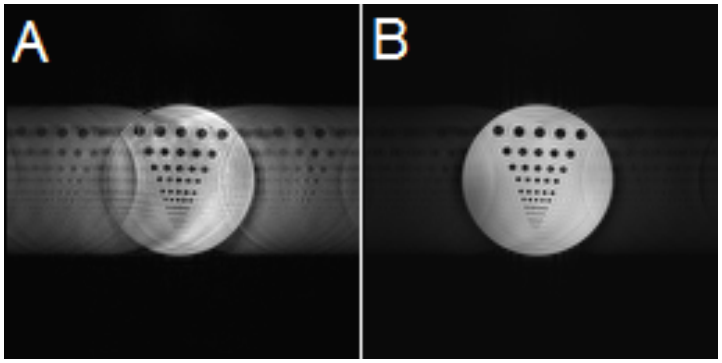

Figure 3.6: *Effect of signal oscillations during the transient state. Depending on the severity of the oscillations ghosting artifacts occur in the phase encoding direction. A: No preparation. B: $\alpha/2$ pulse preparation.*

Therein, λ is decaying constant and M_{SS} is the signal during the steady-state. Using a simple transformation the exponential decay of the signal during the transient phase becomes even more visible. Using the following transformation

$$F_n = M_n - M_{SS}, \tag{3.13}$$

with the starting condition

$$F_1 = M_1 - M_{SS} = \sin(\alpha/2)M_0 - M_{SS}, \tag{3.14}$$

the signal can be described as

$$F_n = F_1 \cdot \lambda^n. \tag{3.15}$$

The value of the decay constant λ depends on the flip angle α and the relaxation times T_1 and T_2 [Scheffler and Lehnhardt, 2003]

$$\lambda = \frac{1}{2}\cos(\alpha)(c_1 - c_2) + \sqrt{\frac{1}{4}(c_1 - c_2)^2\cos^2(\alpha) + c_1 c_2}, \tag{3.16}$$

with the abbreviations $c_1 = e^{-TR/T_1}$ and $c_2 = e^{-TR/T_2}$.

3.4.2 Steady-State

The evolution of the magnetization under the influence of a periodic sequence of RF-pulses and gradients can be characterized by the following formula [Hargreaves et al., 2001]

$$\mathbf{M}_{k+1} = \hat{\mathbf{A}}\mathbf{M}_k + \mathbf{B}. \tag{3.17}$$

In this recursion $\mathbf{M}_k$ stands for the magnetization after the k^{th} RF-pulse. The matrix $\hat{\mathbf{A}}$ and the vector $\mathbf{B}$ are responsible for the change of the magnetization over time. If the change in magnetization caused by the RF-pulse excitation is just strong enough to hold the magnetization in a balance, the so called steady-state is reached. Mathematically this is given by

$$\mathbf{M}_{k+1} = \mathbf{M}_k = \mathbf{M}_{SS}. \tag{3.18}$$

Using this in the previous equation the magnetization of the steady-state can be calculated solely by the change of the magnetization over time as

$$\mathbf{M}_{SS} = \left(\hat{\mathbf{I}} - \hat{\mathbf{A}}\right)^{-1}\mathbf{B}. \tag{3.19}$$

In a simple case, the RF-pulses of a sequence follow each other after the constant repetition time TR. In this case the evolution of the magnetization by the RF-pulses can be characterized

as the rotation by the angle α around the x'-axis and the rotation matrix is given by

$$\hat{\mathbf{R}}(\alpha) = \begin{pmatrix} 1 & 0 & 0 \\ 0 & \cos(\alpha) & \sin(\alpha) \\ 0 & -\sin(\alpha) & \cos(\alpha) \end{pmatrix}. \tag{3.20}$$

However, due to the gradient fields the magnetization also precesses around the z-axis with the angle Ω, with the corresponding rotation matrix

$$\hat{\mathbf{P}}(\Phi) = \begin{pmatrix} \cos(\Phi) & \sin(\Phi) & 0 \\ -\sin(\Phi) & \cos(\Phi) & 0 \\ 0 & 0 & 1 \end{pmatrix}. \tag{3.21}$$

Additionally, the magnetization also relaxes with T_1 and T_2 during the time between the excitation pulses. This can be accounted for by multiplication of a matrix $\hat{\mathbf{C}}$ and the subsequent addition of a vector $\mathbf{D}$. The form of these is given by

$$\hat{\mathbf{C}}(TR) = \begin{pmatrix} e^{-\frac{TR}{T_2}} & 0 & 0 \\ 0 & e^{-\frac{TR}{T_2}} & 0 \\ 0 & 0 & e^{-\frac{TR}{T_1}} \end{pmatrix} \qquad \mathbf{D} = \left(\hat{\mathbf{I}} - \hat{\mathbf{C}}(TR)\right) \begin{pmatrix} 0 \\ 0 \\ M_0 \end{pmatrix}. \tag{3.22}$$

Thus, the magnetization between two subsequent pulses a and b can be calculated as

$$\mathbf{M}_b = \hat{\mathbf{R}}(\alpha)\left(\hat{\mathbf{C}}(TR)\cdot\hat{\mathbf{P}}(\Phi)\cdot\mathbf{M}_a + \mathbf{D}(TR)\right) \tag{3.23}$$

$$= \hat{\mathbf{R}}(\alpha)\cdot\hat{\mathbf{C}}(TR)\cdot\hat{\mathbf{P}}(\Phi)\cdot\mathbf{M}_a + \hat{\mathbf{R}}(\alpha)\cdot\mathbf{D}(TR). \tag{3.24}$$

And the previously unknown variables $\hat{\mathbf{A}}$ and $\mathbf{B}$, are given by

$$\hat{\mathbf{A}} = \hat{\mathbf{R}}(\alpha)\cdot\hat{\mathbf{C}}(TR)\cdot\hat{\mathbf{P}}(\Phi) \tag{3.25}$$

$$\mathbf{B} = \hat{\mathbf{R}}(\alpha)\cdot\mathbf{D}(TR). \tag{3.26}$$

Now the magnetization in the steady-state can be calculated as

$$\mathbf{M}_{SS} = \begin{pmatrix} M_0 \cdot (1 - c_1) \cdot [c_2 \cdot \sin(\alpha)\sin(\Phi)]/N \\ M_0 \cdot (1 - c_1) \cdot [(1 - c_2 \cdot \cos(\Phi))\sin(\alpha)]/N \\ M_0 \cdot (1 - c_1) \cdot [c_2(c_2 - \cos(\Phi)) + (1 - c_2 \cdot \cos(\Phi))\cos(\alpha)]/N \end{pmatrix} \tag{3.27}$$

with the abbreviations $c_1 = e^{-TR/T_1}$, $c_2 = e^{-TR/T_2}$ and

$$N = 1 - c_1\cos(\alpha) - (c_1 - \cos(\alpha))c_2^2 + c_2(c_1 - 1)(1 + \cos(\alpha))\cos(\Phi). \tag{3.28}$$

Using this knowledge of the steady-state signal the influence of different measurement parameters can be simulated. As such it is an important tool to estimate optimal signal enhancement for all steady-state based sequences.

3.5 The Standard bSSFP Sequence

bSSFP is an abbreviation for balances steady-state free precession. The sequence was first proposed by [Oppelt et al., 1986]. A bSSFP sequence is a modified gradient echo sequence. Its properties are best explained using the sequence scheme depicted in figure 3.7.
Unlike a normal gradient echo sequence the transverse magnetization is rephased after TR. Instead it gets balanced in every direction. Thus, if T_2 relaxation is neglected, the transverse magnetization at position B is the same as at position E. Furthermore, the phase of the RF-pulses alternates between 0° and 180°, respectively. It should be noted that a sequence of this type causes significant oscillation artifacts unless the magnetization is sufficiently prepared. This is true for both the transverse and the longitudinal magnetization. The shape and number of the preparation pulses is something that depends on the properties of the scanned objects and can not be determined generally. Common preparations include a single $\alpha/2$ pulse or different ramps. A bSSFP sequence enters the steady-state after $N = \frac{5T_1}{TR}$ pulses, before that it is in the so called transient state. The biggest advantage of the bSSFP sequences it the high SNR during the steady-state. For a flip angle of $\alpha = 90°$ and $T_1 = T_2$ the steady-state signal of a bSSFP sequence is half as high as the magnetization of the measured object. Unlike other sequences the signal of a bSSFP sequence depends both on T_1 and T_2. This is often considered a hindrance for certain clinical procedures. It should also be noted that bSSFP sequences are

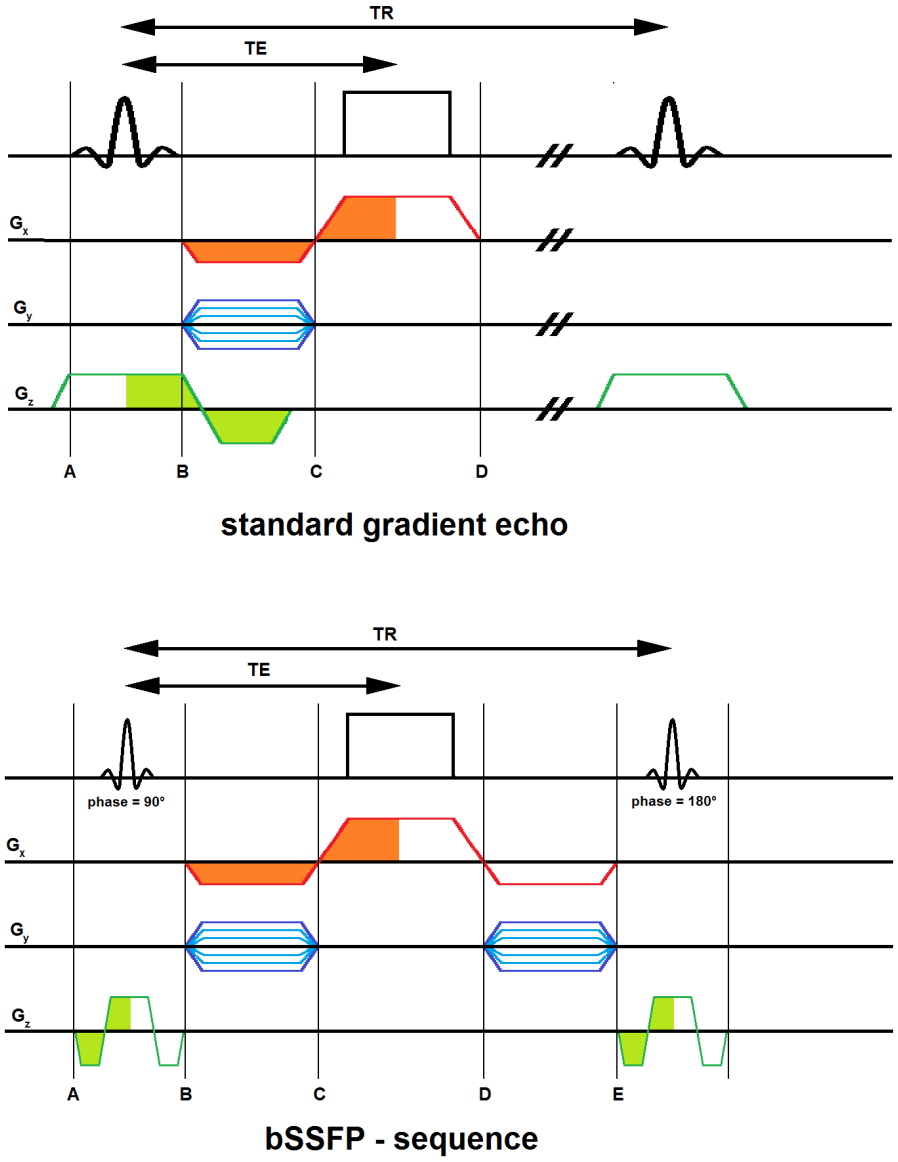

Figure 3.7: *Schematic of a standard bSSFP sequence. The standard gradient echo spoils the remaining transverse magnetization after the acquisition of the signal (top). The bSSFP sequence (bottom) refocuses the remaining transverse magnetization on each axis using gradient moments after the acquisition of the signal. Additionally, the phase of the RF-pulses alternates between 90° and 180° in a bSSFP sequence. The phase of all RF-pulses in the standard gradient echo sequence is the same.*

susceptible to various artifacts. Aside from the oscillation artifacts the second largest artifacts are so called banding artifacts, which are caused by offsets from the Larmor frequency [Zur et al., 1988]. The frequency of the banding artifacts depend only on TR. They occur at

$$\omega_B = \frac{1}{2 \cdot TR}, \tag{3.29}$$

and their higher harmonics. Therefore, a low TR is highly advantageous for bSSFP sequences to avoid banding artifacts. An additional step to reduce banding artifacts is the reduction of macroscopic field inhomogeneities. Thus, a good shim can significantly reduce these off-resonance effects.

3.5.1 Steady-State Signal of the bSSFP Sequence

The transverse magnetization of a bSSFP sequence is refocused after each TR. This means that the signal at the steady-state depends mostly on the dephasing Φ caused by the gradients during a single TR. An alternating phase of 180° as it is commonly used in bSSFP sequences is equivalent to a dephasing of $\Phi = 180°$ [Hinshaw, 1976]. Using this value in the formula to calculate the steady-state magnetization in the last section this leads to

$$M_{SS}^{bSSFP} = \begin{pmatrix} 0 \\ M_0 \frac{(1-E_1)\sin(\alpha)}{1-E_1E_2-(E_1-E_2)\cos(\alpha)} \\ M_0 \frac{(1-E_1)(E_2+\cos(\alpha))}{1-E_1E_2+(E_1-E_2)\cos(\alpha)} \end{pmatrix}. \tag{3.30}$$

Thus, directly after excitation the steady-state signal can be calculated as

$$S_{bSSFP} = \sqrt{M_{SS,x}^2 + M_{SS,y}^2} = M_0 \frac{1-E_1}{1-E_1E_2-(E_1-E_2)\cos(\alpha)}\sin(\alpha). \tag{3.31}$$

For $TR \ll T_{1,2}$ (which is correct in our case) the equation can be simplified by

$$E_{1,2} = e^{-\frac{TR}{T_{1,2}}} \approx 1 - \frac{TR}{T_{1,2}}. \tag{3.32}$$

This leads to

$$S_{bSSFP} = M_0 \frac{\sin(\alpha)}{1+\cos(\alpha)+(1-\cos(\alpha))\frac{T_1}{T_2}}. \tag{3.33}$$

Thus, the steady-state signal of a bSSFP sequence depends on the flip angle α, the ratio of the relaxation times $\frac{T_1}{T_2}$ and TR. The flip angle that provides the maximum steady-state signal can be calculated by derivation by α. This shows that the steady-state signal can be maximized for the flip angle

$$\alpha_E = \arccos\left(\frac{T_1 - T_2}{T_1 + T_2}\right). \tag{3.34}$$

3.5.2 The Pseudo Steady-State and its Relation to SAR and SNR

The standard bSSFP sequence operates in continuous acquisition mode. As such, the magnetization does not have time to relax between measurements. Thus, the steady-state is reached normally and the equations described in the previous section are correct. Aside from continuous there is also a non-continuous acquisition. This mode features a pause between the acquisition of each image. Due to the magnetization relaxing during the pause, a true steady-state is never reached. However, if the wait time TW between each image is constant a pseudo steady-state is reached after the acquisition of first few dummy images. Figure 3.8 shows a visual representation of a non-continuous acquisition. Which acquisition mode should be used depends on the requirements of the measurement. The continuous acquisition mode has many advantages. For example, it is the most effective way to acquire signal over time. Additionally, the signal intensity is constant during the acquisition, which is important for quantification. Non-continuous measurements will generally only retain an effectiveness of between 60 to 80% compared to the continuous mode and the signal intensity will change during the acquisition of the images. For these reasons most applications use the continuous acquisition mode.

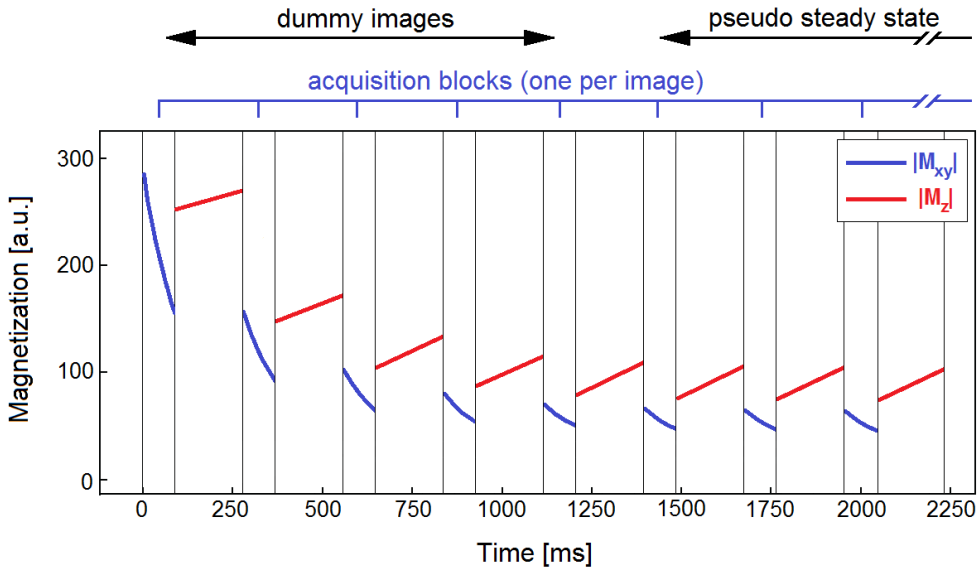

Figure 3.8: *Non-sequential acquisition and pseudo steady-state.*

However, the non-continuous acquisition mode has advantages as well. Sequences with high SAR requirements can make use of the pause to stay within the restrictions. Secondly, some low signal applications only lead to a SNR near or below 1 in the regular steady-state. Thus, averaging, which makes the continuous mode very successful, can not be used. Instead these measurements benefit from the higher signal of the pseudo steady-state. The non-continuous mode further benefits from a centric acquisition as the lines in the center of k-space also benefit from the higher signal at the start of image acquisition. Due the high SAR requirement all bSSFP sequences used in this work use the non-continuous and centric acquisition. The wait time is around twice as long as the image acquisition. This is in accordance with [Bauman, 2010].

3.6 The Standard Fourier Decomposition Method

Fourier Decomposition was first developed by [Deimling et al., 2008] using a steady-state free precession (SSFP) sequence at low field strength (0.35T). This sequence was able to acquire a series of fast 2D images of the lung and yielded peaks corresponding to both respiratory and cardiac cycles when analyzed in the time domain. The method was further optimized by [Bauman, 2010]. By changing the sequence to a balanced SSFP (bSSFP) and increasing the field strength to 1.5T, higher quality ventilation and perfusion maps could be obtained. A brief description of the current standard is given in the next section. The main processes that change the MR signal in the human lung are ventilation and perfusion. Ventilation changes the tissue density due to the inflow and outflow of air, while perfusion changes the amount of blood over time. Both processes are clearly visible in the time domain of the MR signal provided that the temporal resolution of the image series is substantially higher than the respiratory and cardiac frequency. As the respiratory frequency at rest is between 12-20 breaths per minute and the normal heart rate is between 60-80 beats per minute, the cardiac cycle is clearly the limit. Following the Nyquist theorem [Nyquist, 1928] the sampling rate needs to be twice as high as the heart rate, thus requiring speeds of 3 images per second. The application of the Fourier transform to a registered 2D data set $R(x,y,t)$ at the time points $t = 1, ..., N$ leads to a spectral image with the frequencies $\omega = 1, ..., N$

$$F[R(x,y,t)] = M(x,y,\omega). \tag{3.35}$$

The spectral resolution of these images is given by the sequence parameters TA (acquisition time) and TW (temporal resolution) in the following way

$$\Delta\omega = \frac{1}{2(TA + TW)}. \tag{3.36}$$

To analyze the image both the sum of the signal intensity in each image and its FFT were calculated

$$s(t) = \sum_{(x,y)} R(x,y,t), \tag{3.37}$$

$$F[s(t)] = S(\omega). \tag{3.38}$$

The corresponding frequency spectrum $S(\omega)$ then shows two frequency peaks ω_v and ω_q, which are related to perfusion and ventilation, respectively. After identifying these peaks the signal corresponding to these frequencies can be extracted to achieve both perfusion- and ventilation weighted images. Mathematically this is done by integration

$$Q(x,y) = \sum_{i=-l}^{l} |M(x,y,\omega_q + i)|^2 \cdot G_\beta(i), \tag{3.39}$$

$$V(x,y) = \sum_{i=-l}^{l} |M(x,y,\omega_v + i)|^2 \cdot G_\beta(i). \tag{3.40}$$

The constant l is an adjustable to determine the width of the frequency peaks that are used to obtain the images, and $G_{beta}(i)$ is a Gaussian window with the variance β. The whole process of the standard FD method can be visualized by the flowchart in figure 3.9. Example images of perfusion and ventilation weighted images can be seen in figure 3.10.

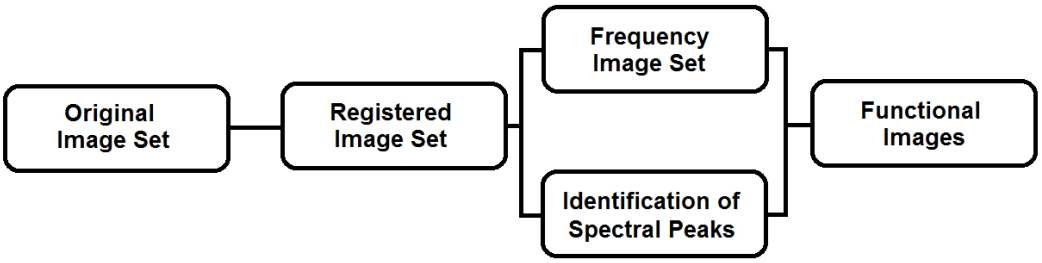

Figure 3.9: *Flowchart of the standard FD method. After registering the original data-set, the FFT is applied to acquire the frequency image sets. Additionally, the ventilation and perfusion frequency peaks are found from the spectrum of the data-set. The frequency image sets are then integrated over the corresponding peaks to achieve both ventilation and perfusion-weighted images.*

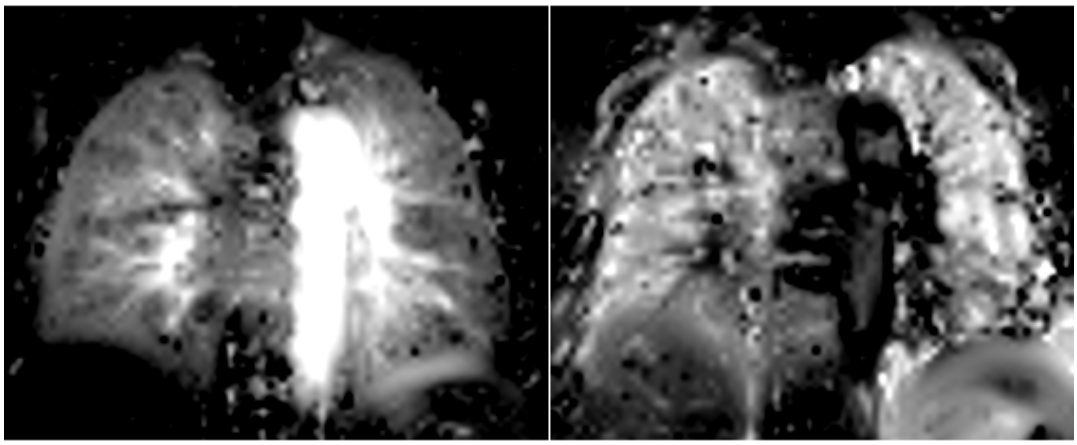

Figure 3.10: *Examples of functional FD images. The perfusion weighted image (left) shows the areas with increased perfusion, such as the large vessels, brightly. The ventilation weighted image (right) shows the areas of increased ventilation instead.*

3.7 Image Registration

Image registration describes the task of aligning images into the same coordinate system. A general overview of the technique, which is used for different modalities in medical imaging can be found in [Brown, 1992], [Myronenko and Song, 2010] or [Zitova and Flusser, 2003]. In the following the specific modification of the registration algorithm used in this work will be covered. A visualization of the basic process of image registration as a flow chart can be seen in figure 3.11.

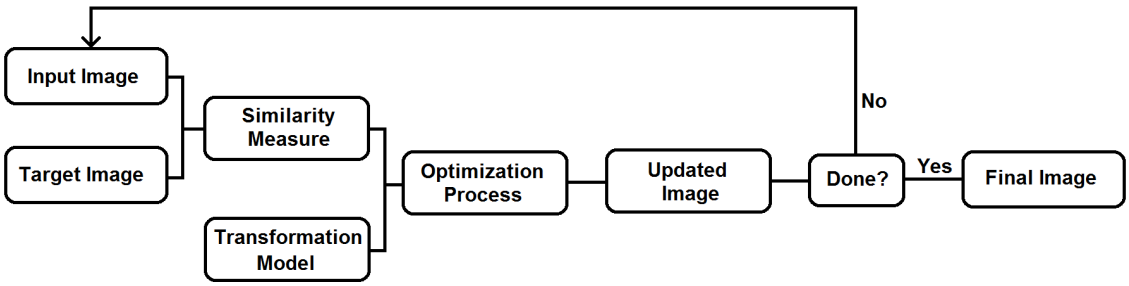

Figure 3.11: *Image registration flow chart. Two images, one defined as input and the other as target are compared using a similarity measure. The result of this measure is then combined with the restrictions of the transformation model and optimized. The updated image then goes through a convergence test to determine if the registration is done.*

3.7.1 Image Registration Framework

The registration of images of the lung requires high flexibility, thus a non-rigid, non-parametric model was chosen. This model can be described according to the framework of [Modersitzki, 2003], as finding a transformation ϕ that optimally registers the input image f into the target image g. Using the transformation ϕ the deformation of the image $\mathbf{u}$ is defined as

$$\mathbf{u}(x) = x - \phi(x). \tag{3.41}$$

To find the optimal transformation a functional τ is minimized. This functional contains both a similarity measure, M and the utilized transformation model R, which is also known as the regularization. As such τ can be described as

$$\min \quad \tau[\mathbf{u}] = \alpha R[\mathbf{u}] + M[f,g,\mathbf{u}]. \tag{3.42}$$

Minimizing τ is equivalent to finding the solution of the corresponding Euler-Lagrange equations

$$\alpha \mathbf{A}[\mathbf{u}] - \mathbf{b}(x,\mathbf{u}(x)) = 0, \tag{3.43}$$

where $\mathbf{A}$ and $\mathbf{b}$ are related to the Gateaux derivatives of R and M, respectively.

3.7.2 Similarity Measure

The similarity measure is designed to identify and align corresponding parts of the matched images. This is generally considered to be the most important and arguably most difficult part of a registration algorithm. While progress has been made on specific problems, such as facial recognition [Li and Jain, 2011], the general task of identifying similar structures in different images is still considered unsolved. As such the specific properties of the source images have to be considered before a similarity measure can be chosen. MR images of the lung possess multiple challenges for post processing algorithms. First and foremost the low signal of the lung parenchyma makes it difficult to identity structures. However, many other effects, such as the inflow of blood, the density changes of the parenchyma during a breathing cycle and its gravitational dependence, pose significant problems. Due to these problems a similarity measure that directly compares image intensities is not a suitable solution. Instead, the recently developed residual complexity similarity measure [Myronenko and Song, 2010], was chosen. This measure was specifically created with the goal to handle spatially dependent intensity changes. The following is a short description of this similarity measure. The intensity of the source images, input image f and target image g, are related by

$$g = f(\mathbf{u}) + S + n, \tag{3.44}$$

where S is an intensity correction field and n resembles zero-mean Gaussian noise. Using a maximum apostori probability (MAP) estimate [DeGroot, 2004] and under the condition that all pixels are independent and identically distributed random variable, this is equivalent to minimizing

$$E(\mathbf{S},\mathbf{u}) = \|\mathbf{g} - \mathbf{f}(\mathbf{u}) - \mathbf{S}\|^2 + \beta\|\mathbf{PS}\|^2. \tag{3.45}$$

Here, $\mathbf{g}$, $\mathbf{f}$ and $\mathbf{S}$ are in column-vector form, $\|.\|$ is the Euclidean norm and $\mathbf{P}$ is a yet to be defined regularization operator for $\mathbf{S}$. This equation can analytically be solved for $\mathbf{S}$, giving the final form of the residual complexity similarity measure

$$E(\mathbf{u}) = \sum_{n=1}^{N} \log\left(\frac{(\mathbf{q}_n^T\mathbf{r})^2}{\alpha} + 1\right). \tag{3.46}$$

$\mathbf{r}$ is the residual image after the transformation

$$\mathbf{r} = \mathbf{g} - \mathbf{f}(\mathbf{u}), \tag{3.47}$$

and $\mathbf{q}_i$ are the columns of the eigenvector matrix $\mathbf{Q} = [\mathbf{q}_1, ..., \mathbf{q}_n]$, created by the spectral decomposition of the matrix $\mathbf{P}^T\mathbf{P}$. The last step in the definition of the residual complexity similarity measure is the definition of the matrix $\mathbf{Q}$. With the definition above

$$\mathbf{P}^T\mathbf{P} = \mathbf{Q}\mathbf{\Lambda}\mathbf{Q}^T, \tag{3.48}$$

where $\mathbf{\Lambda}$ is the diagonal matrix of eigenvalues, $\mathbf{\Lambda} = d[\lambda_1, ..., \lambda_n], \lambda_i \geq 0$. The matrix $\mathbf{Q}$ is chosen as basis for a direct cosine transform (DCT) as it corresponds to the regularizer $\mathbf{P}$. After this definition the following set of equations can be used to implement the residual complexity similarity measure

$$\mathbf{r} = \mathbf{g} - \mathbf{f}(\mathbf{u}), \quad \mathbf{c} = \mathrm{dctn}(\mathbf{r}), \tag{3.49}$$

$$E = \sum \log\left(\frac{\mathbf{c}^2}{\alpha} + 1\right), \tag{3.50}$$

$$\nabla E = -\mathrm{idctn}\left(\frac{2\mathbf{c}/\alpha}{\mathbf{c}^2/\alpha + 1}\right) \nabla\mathbf{f}(\mathbf{u}) \frac{\partial \mathbf{u}}{\partial \theta}. \tag{3.51}$$

In these equations dctn and idctn denote the normal and inverse multidimensional discrete cosine transforms, α an adjustment parameter that was empirically set to 0.05, $\nabla\mathbf{f}$ the intensity image gradient and θ the transformation parameters. ∇E is the gradient of the similarity measure and is needed for the variational optimization process. In a less formulated description the residual complexity similarity measure can be visualized as optimizing the sparsity in the residual image. The discrete cosine transform of an image results in a set of coefficients which represent the information contained in the image. The number of coefficients larger than

zero is directly related to the information contained in the image. Therefore, two images can be registered by minimizing the amount of non-zero coefficients of the residual image. The logarithmic function accomplishes this very well as small values are disproportionally penalized more than large ones.

3.7.3 Transformation Model

To ensure physically realistic movement the deformation of the image needs to be restricted. This part of image registration is called the transformation model. These restrictions are important as images are imperfect and the similarity measure might, for example move a noisy voxel inside the patient to the outside of the image. Such a transformation, while mathematically accurate, is physically unrealistic and therefore heavily penalized by the transformation model. As there are different transformation models it is important to choose one that fits the specific registration problem. In this case, as the lungs expand unevenly during breathing a complex transformation model is required. The best results are achieved using a modified transformation model that is based on the deformation of a viscous fluid [Bro-Nielsen and Gramkow, 1996]. The basic idea of this transformation model will be explained in the following paragraph. Unlike the particle movement of solid objects, which is tracked using their coordinates in a Lagrange reference frame, fluid motion is tracked in an Eulerian reference frame instead. Looking at a particle at the position $\mathbf{x} = [x_1,x_2]^T$ in the moving image J, the position at a time t can be described as

$$\mathbf{t}(\mathbf{x},t) = \mathbf{x} - \mathbf{u}(\mathbf{x},t), \tag{3.52}$$

with $\mathbf{u}(\mathbf{x},t)$ being the displacement of the particles. The velocity is given by the derivative of the displacement in the Eulerian reference frame

$$\mathbf{v} = \frac{\partial \mathbf{u}}{\partial t} + \nabla \mathbf{u} \cdot \mathbf{v}. \tag{3.53}$$

This equation defines the deformation field $\mathbf{u}$ using the velocity $\mathbf{v}$. Thus, using a known velocity, it can be solved to achieve the image deformation $\mathbf{u}$. The velocity is derived using the fundamental laws to describe the flow of a viscous fluid [Christensen et al., 2007]. These laws are based on the basic assumptions of conservation of mass, which can mathematically

be described as

$$\frac{d\rho}{dt} + \rho\nabla \cdot \mathbf{v} = \eta, \tag{3.54}$$

where ρ is the density of the fluid and η is the rate at which mass enters or leaves a specific volume. Combining both conservation of mass and momentum and using the Reynolds transport theorem, the momentum equation can be derived as

$$\rho\frac{d\mathbf{v}}{dt} + \mathbf{v} \cdot \eta - \nabla \cdot \mathbf{T} - \mathbf{b} = 0, \tag{3.55}$$

where $\mathbf{T}$ is called the Cauchy stress tensor and $\mathbf{b}$ the body force acting on the material. The definition of the stress tensor $\mathbf{T}$ is necessary to allow large, non-linear deformations while also ensuring a smooth deformation field. The Cauchy tensor can be modeled using the Navier-Possion fluid model. This model defines $\mathbf{T}$ as $\mathbf{t} = (\lambda(tr(\mathbf{D}) - p) + 2\mu\mathbf{D}$. λ and μ are the Lamé parameters to describe shearing, p is the pressure and $\mathbf{D}$ the rate of deformation, which is defined as

$$\mathbf{D} = \frac{1}{2} \cdot (\nabla\mathbf{v} + (\nabla\mathbf{v})^T). \tag{3.56}$$

This modifies the equation describing the conservation of mass and momentum to

$$\mu\Delta\mathbf{v} + (\mu + \lambda)\nabla(\nabla \cdot \mathbf{v}) + \mathbf{b} = \nabla p + \rho\frac{d\mathbf{v}}{dt} + \mathbf{v} \cdot \eta. \tag{3.57}$$

Using the Reynolds transportation theorem the Reynolds number is defined as the ratio between inertial and viscous forces. For our problem a very low Reynolds number can be expected [Bro-Nielsen and Gramkow, 1996], which means the inertial forces can be set to zero. This simplifies the final equation to

$$\mu\Delta\mathbf{v} + (\mu + \lambda)\nabla(\nabla \cdot \mathbf{v}) = \mathbf{b}. \tag{3.58}$$

It should be noted that this equation depends on the body force $\mathbf{b}$, which is the gradient of the similarity measure. The Lamé parameters (μ and λ) can be converted to different elastic parameters such as Young's modulus and Poisson's ratio, which are more commonly used for homogeneous isotropic materials.

3.7.4 Optimization Process

Finding an optimal solution for both the similarity measure and the transformation model is a complex mathematical task. This work uses the Fourier-based method from [Cahill et al., 2007]. In the next paragraph, a brief coverage of the optimization process is given, for more details please refer to [Clarke, 2013]. The first step to solving a differential equation is the definition of boundary conditions. Here, periodic conditions scaled on an hyper-cube are used

$$\mathbf{u}_r(\mathbf{x}|x_s = 0) = \mathbf{u}_r(\mathbf{x}|x_s = 1) \quad \forall \mathbf{x} \in \delta\Omega \quad r,s = 1, ..., p. \tag{3.59}$$

Periodic boundary conditions allow eigenfunctions of the Fourier Transform as solutions, which allows much faster computation times than traditional methods [Cahill et al., 2007]. Applying the following linear operator L

$$L = (2\mu + \lambda)\Delta\mathbf{I} - (\mu + \lambda)\text{graddiv} \tag{3.60}$$

to equation 3.58, transforms it into a non-homogeneous bi-harmonic equation of the shape

$$\Delta^2 y = f. \tag{3.61}$$

A differential equation of this type can be solved by sampling it on an n-dimensional lattice with N_j samples

$$y = [y_k], \quad f = [f_k] \tag{3.62}$$

$$\mathbf{k} = (k_1, ..., k_n), \quad k_j = 0, ..., N_j - 1. \tag{3.63}$$

This defines the discrete Laplacian as

$$(\Delta y)_k = \sum_{j-1}^{n} (y_{k-e_j} + y_{k+e_j} - 2y_k). \tag{3.64}$$

Herein, e_j is the j-th column of the identity matrix. To achieve the double Laplacian Δ^2 this equation is applied twice. Our functions f and y can be written as a linear combination of

orthogonal basis functions

$$y_j = \sum_k \hat{y}_k \theta_j^k \quad \forall j, \tag{3.65}$$

$$f_j = \sum_k \hat{f}_k \theta_j^k \quad \forall j. \tag{3.66}$$

These basis functions can also be chosen to be eigenfunctions of the double Laplacian operator, thus

$$\Delta^2 \theta^k = \Delta(\Delta\theta^k) = \omega_k^2 \theta^k. \tag{3.67}$$

This changes the differential equation to

$$\sum_k \hat{y}_k \omega_k^2 \theta_j^k = \sum_k \hat{f}_k \theta_j^k, \tag{3.68}$$

which leads to the solution $y_k = \frac{f}{\omega_k^2}$. The basis functions, which fulfill both conditions as shown by [Cahill et al., 2007] are

$$\theta_j^k = \beta_2 \prod_{m=1}^{n} \exp\left(\frac{2ik_m j_m \pi}{N_m}\right), \tag{3.69}$$

and the eigenvalues are

$$\omega_k = \sum_{m=1}^{n} (2\cos\frac{2k_m\pi}{N_m} - 2). \tag{3.70}$$

These choices allow the efficient solution of Naviers equation and the calculation of the corresponding deformation field. This process is then iteratively completed until a convergence criterion is reached.

4 Results

The main focus of this work was the optimization of the 2D bSSFP sequence used for functional FD lung MRI. While many of the simple parameters were already optimized by [Bauman, 2010], some more advanced techniques were not utilized. Additionally, with the modified and improved sequence new possibilities for functional FD lung MRI arose. Such as quantification of perfusion [Kjørstad et al., 2014a], ventilation [Kjørstad et al., 2014b] and an improved reconstruction scheme [Wujcicki et al., 2015].

4.1 (Ultra-)fast bSSFP

The first parameter that strongly influences the contrast of a bSSFP image of the lung is the echo time. The signal of the lung parenchyma decays with $T_2^* \approx 1\ ms$ [Hatabu et al., 1999]. Thus, even the fastest echo times that are available to a conventional bSSFP sequences of around 0.8 ms - 0.9 ms are not ideal. By the time the signal is acquired around 60% of the magnetization is already decayed. A visual representation of the decay is given in figure 4.1. The measurement points were acquired using the porcine lung phantom with the breathing pump turned off. This enables both the reduction of motion artifacts and choosing a stable ROI, as well as longer averaging. Aside from the conventional bSSFP sequences, there is also the (ultra-)fast variant. This denotation was coined by [Bieri, 2012]. The technique was specifically designed for morphological proton lung MRI using SSFP sequences, due to its extremely short echo- and repetition times. As such, the design does not only benefit from the short T_2^* of the lung parenchyma, but also from its strong susceptibility variations. The occurrence of susceptibility banding artifacts is reduced by using (ultra-)fast bSSFP sequences, due to the faster repetition time, which in turn shortens the pass band. The method proposed by [Bieri, 2012] is fairly radical and proposes extremely asymmetric echoes. Asymmetric echoes reduce the strength of the readout gradient to shorten the echo time. In turn, this shortens

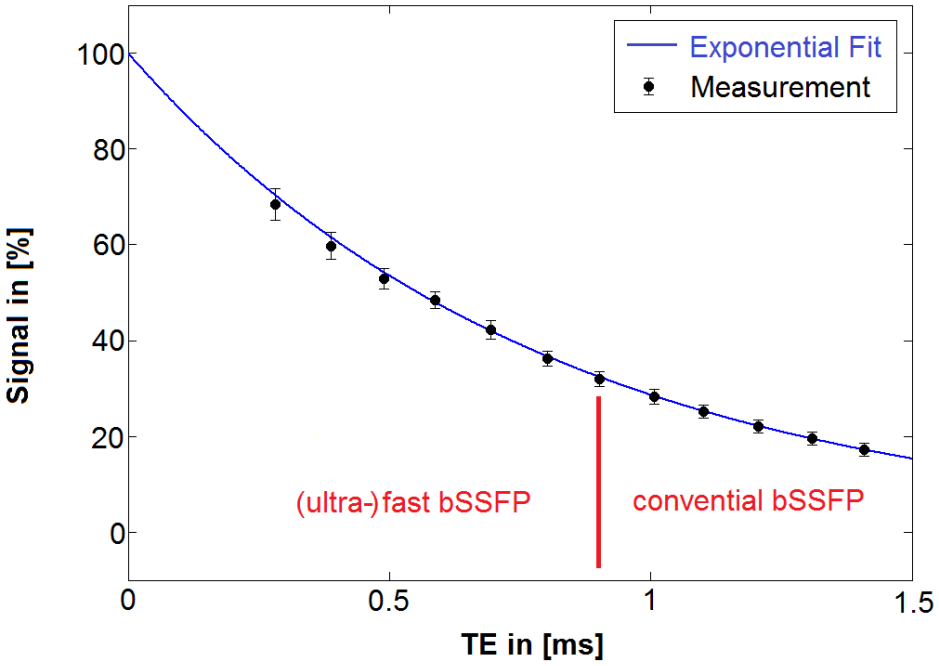

Figure 4.1: *Decay of the magnetization of the lung parenchyma at 1.5 Tesla. Using conventional bSSFP sequences 60% of the magnetization is decayed before a signal can be acquired. (Ultra-)fast bSSFP sequences with echo times of up to 0.3 ms fare much better.*

the signal acquisition right after the excitation pulse. The reconstruction of the signal is done using an estimation of the first, shortened half and the second, fully acquired half of the signal. A visual representation of an asymmetric readout can be seen in figure 4.2. Mathematically, asymmetric echoes are characterized by the asymmetry factor λ. This factor describes the relationship between the first and the second part of the acquired signal. It is defined as

$$\lambda = \frac{\text{Acquisition(first part)}}{2 \cdot \text{Acquisition(second part)}}. \tag{4.1}$$

For symmetric echoes this leads to λ=50% and for asymmetric echoes to λ<50%. While asymmetric echoes with $\lambda = 0$ are technically possible, this would lead to frequency encoding artifacts, as the gradient would not have enough time to ensure sufficient encoding. This can be seen as streaks or blurring in the frequency encoding direction. As the artifacts are most visible at the transition between the object and the empty space they can be characterized by the normalized noise. For this purpose two ROIs were specified, one just above the porcine lung phantom (ROI1) and one far away from any source that could cause artificial noise (ROI2).

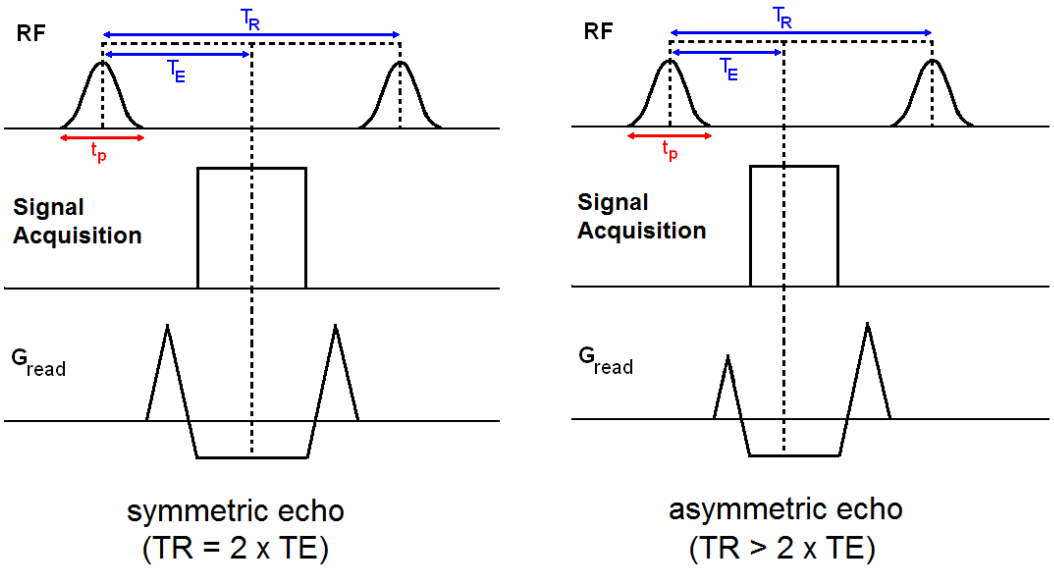

Figure 4.2: *Asymmetric readout of a bSSFP sequence. Using a symmetric readout (left), the gradient is fully balanced and the relation $TR = 2 \cdot TE$ is correct. Using an asymmetric readout (right), the first half of the readout gradient is weakened compared to the second half. This leads to faster echo times. The relation is now $TR > 2 \cdot TE$.*

By using the relation

$$\text{Normalized Noise} = \frac{\text{Signal(ROI 1)}}{\text{Signal(ROI 2)}} \tag{4.2}$$

the severity of the artifacts can be calculated. An example of what these types of artifact look like and how ROIs to measure the normalized noise should be chosen, is shown in figure 4.3. An artifact free image would lead to values of the normalized noise around 1, while anything

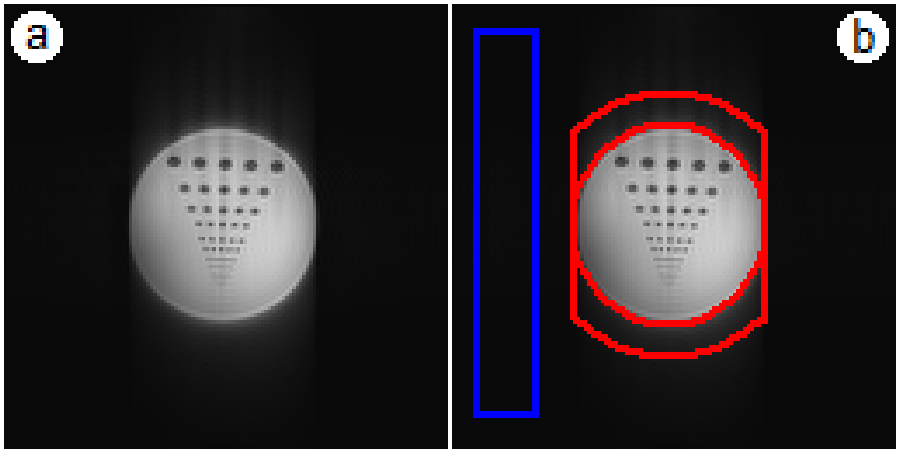

Figure 4.3: *Readout artifacts caused by strong asymmetric echoes. Figure a (left) exemplary shows the artifacts in frequency encoding direction (vertical). Figure b (right) exemplary shows how the ROIs to determine the normalized noise should be chosen. The value measured in ROI1 (red) will be significantly higher than the values in ROI2 (blue) if frequency encoding artifacts are present.*

larger than 1 would indicate the presence of frequency encoding artifacts. The results of the measurements performed on the porcine lung phantom are shown in figure 4.4.

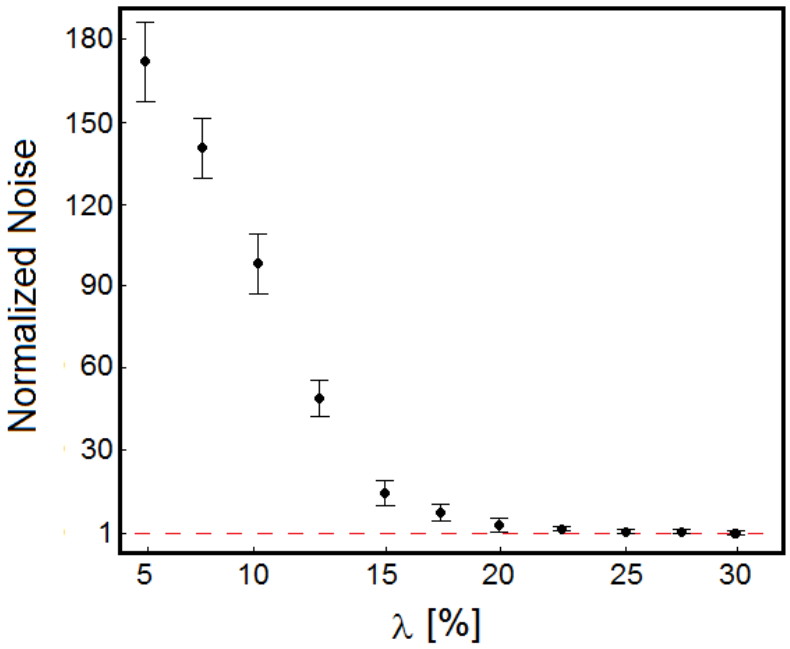

Figure 4.4: *Normalized noise for asymmetric readouts of different magnitude. Values near 1 signal that there are no artifacts present, while values larger signal the presence of readout artifacts.*

The graph shows, that asymmetry factors of lower than 15% lead to large streaking artifacts in the image. However, strong asymmetric echoes of between 15% and 20% still lead to significant deviations in the noise levels. These artifacts can be neglected for imaging tissues with a relatively large SNR compared to the surrounding area (for example morphological imaging of the blood vessels in the lung), as the blurred signal intensity would still be small compared to the actual signal. However, for functional ventilation this is not the case. Any blurred signal from the blood vessels that overlays with the signal from the parenchyma could cause extreme signal deviations. Thus, only asymmetry factors larger than 20% should be used for FD lung MRI. For this work λ=22.5% was chosen. This modified the timing of the original sequence used for FD lung MRI [Bauman, 2010] from $TE/TR = 0.8/1.9\ ms$ (λ=40%) to $TE/TR = 0.6/1.7\ ms$ (λ=22.5%). Based on figure 4.1 this change lead to a signal improvement in the lung parenchyma of around $16 \pm 2\%$.

	T_1 [ms]	T_2 [ms]
Lung parenchyma	1266 ± 142	51 ± 4
Blood	1441 ± 120	290 ± 30
Fat	343 ± 37	58 ± 4
Liver	576 ± 30	46 ± 6

Table 4.1: *Relaxation times of various tissues at 1.5T [Stanisz et al., 2005] or [Stadler et al., 2005].*

4.2 Optimization of the RF-Pulse

The second parameter that heavily influences the signal intensity of the measurement is the flip angle α. Due to the semi-transient behavior of the bSSFP sequence used for FD lung MRI, estimations based on the steady-state formulas are incorrect. In the next section the behavior of the bSSFP signal for different flip angles is simulated and subsequently the flip angle design is optimized using a two speed VERSE approach.

4.2.1 Simulation of the Signal Behavior

Based on the simplified formula for the optimal flip angle, deduced in the previous chapter

$$\alpha_{opt} = \arccos\left(\frac{T_1/T_2 - 1}{T_1/T_2 + 1}\right), \tag{4.3}$$

one would expect the optimal flip angle for the lung parenchyma to be between 20° and 30°. The relaxation times for the lung parenchyma at $1.5T$ can be seen in table 4.1. However, in practice this is not the case. The measured values show a big discrepancy when compared to the estimated values of the approximated formula

$$S \approx \frac{M_0 \text{sion}(\alpha)}{1 + \cos(\alpha) + (1 - \cos(\alpha))(T_1/T_2)}. \tag{4.4}$$

The realization that this discrepancy exists is not a new result. Its existence was already documented by a measurement in [Bauman, 2010]. For reference, figure 4.5 shows the original measurement, which was conducted five years ago. However, the previously proposed explanation that this effect is caused by the semi-transient nature of the sequence, is not completely accurate. While this is a factor, it is not the sole reason. To achieve an optimal pulse design, is it necessary to acquire a more profound understanding of the dependence of the signal intensity

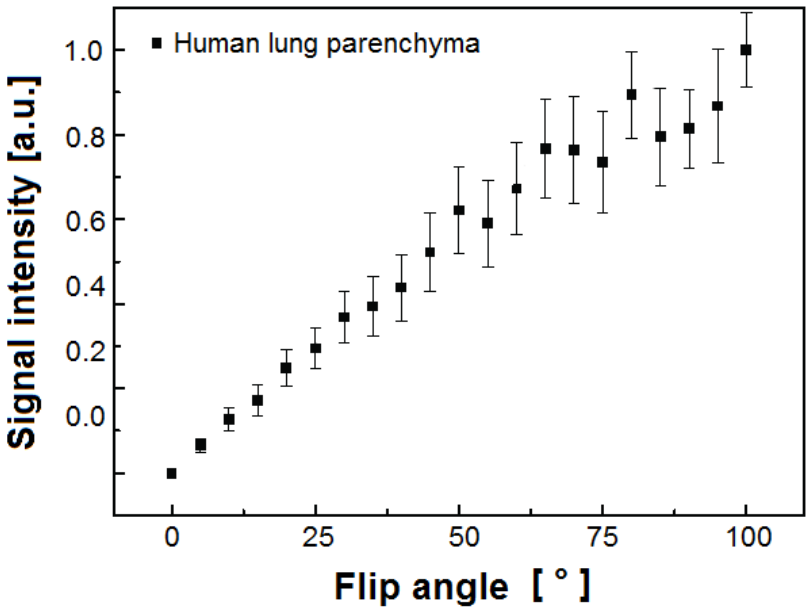

Figure 4.5: *Dependence of the signal intensity of the human lung parenchyma on the flip angle as published in [Bauman, 2010]. As noted by the author the maximum expected between 20° and 30∘ does not occur. The important sequence parameters were $TE/TR = 0.9/1.8\ ms$, $TW = 300\ ms$, $GRAPPA = 2$. The preparation was done with a 10 step linear ramp and the image was acquired using 48 pulses of the same flip angle. Additionally, it has to be noted that the measurement is blighted by large variations and errors. These are mainly caused by motion artifacts and the inability to accurately assign the same ROI to each image.*

on the flip angle. Besides never reaching a true steady-state, the other main culprit for the discrepancy is the general negligence of the duration of the RF-pulse (T_{pulse}). The formula to determine the optimal flip angle was deduced with the expectation, that the RF-pulse instantaneously flips the magnetization vector ($T_{pulse} \approx 0$). However, in practice this is not the case and relaxation effects during the application of the RF-pulse have to be taken into account. Each excitation pulse of a bSSFP sequences causes a flip of the transverse magnetization. For $T_{pulse} << T_R$ the relaxation during the application of the pulse can be neglected. However, in this case the magnetization changes during the application of the pulse are significant. This is visualized in figure 4.6. The most effective description of this process is splitting the RF-pulse into a series of N instantaneous rotations with the angle of $\alpha_i = \frac{\alpha}{N}$ and allowing for an relaxation of the duration of $T_{pulse,i} = \frac{T_{pulse}}{N}$ after each one. The effect of relaxation during an RF-pulse on the magnetization can intuitively be understood in the following way. Since the transverse magnetization during the application of the pulse is reduced, the T_2 relaxation is reduced as well. This effect leads to a higher signal in the (pseudo-) steady-state. For this work

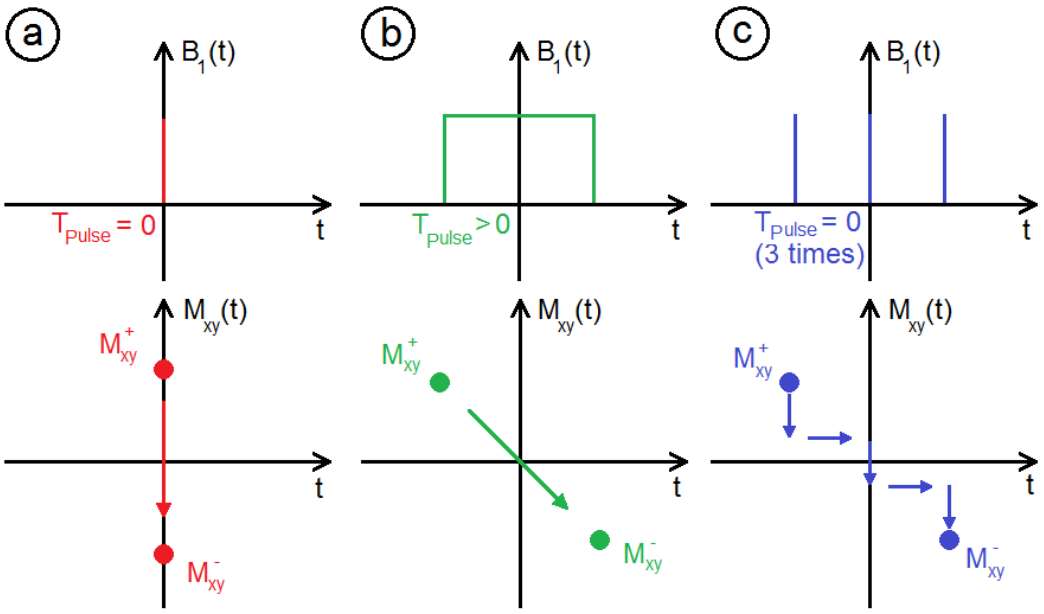

Figure 4.6: *Simplified difference between an instantaneous and non-instantaneous RF-pulse. An instantaneous pulse, as seen in part A of the figure (left), flips the transverse magnetization immediately. Thus, there is no time for an relaxation of the partially flipped magnetization. A realistic RF-pulse, as seen in part B of the image (middle) gradually flips the magnetization. As such, relaxation effects during the pulse occur. This effect is difficult to simulate, therefore it is best to approximate it with a series of instantaneous pulses, as shown in part C of the image (right).*

a simulation of the signal intensity comparing instantaneous and realistic RF-pulses was done. The pulse range was between 1° and 150°. The simulated parameters were $T_1 = 1250\ ms$, $T_2 = 50\ ms$, $TR/TE = 0.9/1.8\ ms$, $TW = 200\ ms$, $T_{pulse} = 1.2\ ms$, a linear preparation ramp of 10 pulses and 48 pulses per image. For the prolonged pulse N was set to be 1000. Additional to this simulation a measurement of the signal intensity was done in the porcine lung phantom. There are three advantages of measuring this effect in an ex-vivo phantom instead of a human volunteer. First and foremost, high flip angles of up to 150° can be used as SAR restrictions can largely be ignored without any consequences. In a human volunteer such high flip angles could potentially be hurt- or even harmful. Secondly, the breathing can be turned off, which enables the chosen ROI to be the same over each measurement. This significantly reduces the variance of the measurement. Lastly, since the phantom does not require any breathing, much longer measurement times are possible. As such, one point of data was acquired by averaging the signal over 5 minutes. This enables us to obtain very precise results. Figure 4.7 shows the results of both simulations and the measurements in the porcine phantom. The measurement in the porcine lung parenchyma agrees very well with the simulation, when both the partially

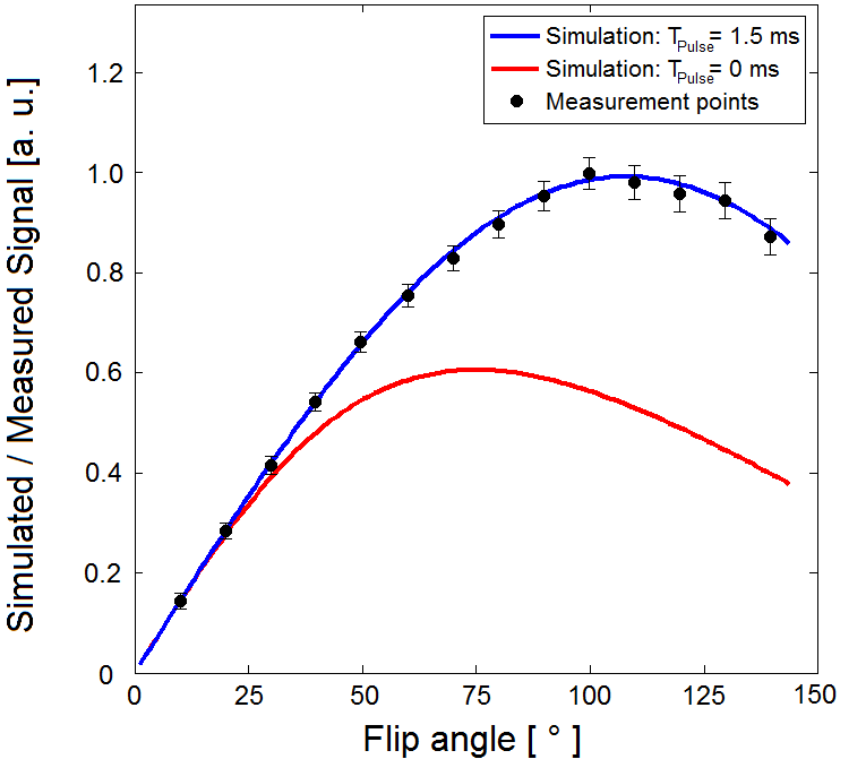

Figure 4.7: *Simulation and measurement of the signal of the lung parenchyma depending on the flip angle. The effect of using instantaneous versus non-instantaneous pulses for the simulation is significant. As expected the optimal flip angle range is pushed towards higher flip angles and the expected signal is higher. The measurement in the porcine lung phantom shows a great agreement with the simulation for non-instantaneous pulses.*

transient nature of the sequence and the non-instantaneous RF-pulses are taken into account. Thus, it is save to say that the increased theoretic understanding of the signal dependence of the lung parenchyma on the flip angle enables the optimal improvement of the sequence. In general the results show that very high flip angles of up to $\alpha \approx 100°$ would lead to the best signal intensity. However, due to SAR constraints this is not possible with the basic sequence described in [Bauman, 2010]. One possible solution to this problem was the application of the variable flip angle technique. The basic idea behind the technique is that higher flip angles could be used to increase the signal intensity in the center of k-space, where the majority of the signal intensity is acquired. In turn, lower flip angles would be used in the periphery of k-space in order to fulfill SAR restrictions.

4.2.2 Using VERSE to Increase the Flip Angle

Aside from changing the flip angles scheme of the bSSFP sequence, there is another way to soften the SAR constraints of the sequence. This can be achieved by changing the form of the RF-pulse from a basic sinc-pulse to a more advanced form. As described in the methods section, VERSE can be used to reduce the amplitude of the pulse, which in turn reduces the SAR and thus enables the use of higher flip angles. The specific technique used in this work is called two-speed VERSE. This technique redistributes the power of the pulse to the outer lobes of the pulse and thus allows a lower amplitude in the middle, effectively lowering the SAR caused by the pulse. This effect can be achieved by assigning two different speeds to the excitation pulse. A higher speed in the outer parts to deposit more energy and a lower speed in the middle part to deposit less. Figure 4.8 shows the used RF pulse before and after application of VERSE and the corresponding gradients. The limitation of the VERSE technique are the maximum gradient slew rate ρ_{max} and the maximum gradient strength G_{max}. To construct a pulse similar to the one shown, the scaling function has to fulfill certain requirements. Defining s_{fast} and t_{fast} as the scaling factor and the duration of the pulse in the outer lobes, the scaling factor in the middle s_{slow} and its duration t_{slow}, are given by

$$s_{slow} = \frac{\frac{p}{2} + \sqrt{((\frac{p}{2})^2 - q)} + G}{G} \tag{4.5}$$

with

$$p = t_{slow} \cdot \rho + 2G \cdot (s_{fast} - 1) \tag{4.6}$$

and

$$q = \rho G \cdot (s_{fast} - 1) \cdot (2T_{pulse} - t_{slow}) - (G \cdot (s_{fast} - 1))^2. \tag{4.7}$$

t_{fast} can then be calculated as

$$t_{fast} = T_{pulse} - t_{slow} - 2\frac{(s_{fast} - s_{slow}) \cdot G}{\rho}. \tag{4.8}$$

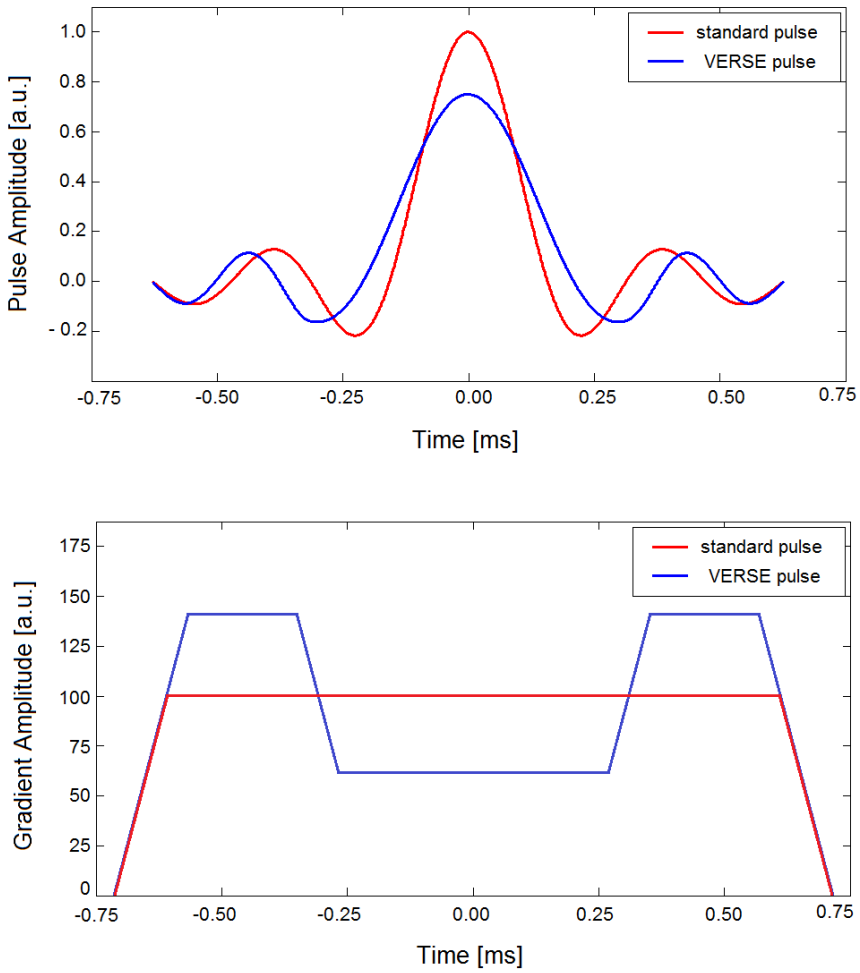

Figure 4.8: *Excitation pulse and slice selection gradient modified by VERSE. The pulse design (top) was changed from a standard sinc-pulse (red) to a two speed VERSE pulse (blue). The gradient shape (bottom) was in turn changed from a constant gradient (red) to a higher gradient on the lobes, and a lower one in the middle (blue).*

For the section between s_{fast} and s_{slow}, linear interpolation should be applied during construction. This is limited by

$$\rho_{max} \geq s_{fast} \cdot \rho \qquad \text{and} \qquad G_{max} \geq s_{fast} \cdot G. \tag{4.9}$$

In the case of this work the advantage of using VERSE was limited due to the already strong use of the gradient system. However, there was still some optimization possible. Leaving the SAR requirement constant, flip angles could be increased by 4°-5°. Based on the dependence of the signal to the flip angle of the previous section this translates to a signal increase of approximately 5%. While the increase is not large enough on its own to change how FD MRI

Name	Formula
Linear	$\alpha_L(x) = (\alpha_{End} - \alpha_{Start}) \cdot \frac{x}{N} + \alpha_{Start}$
Gaussian	$\alpha_G(x) = (\alpha_{End} - \alpha_{Start}) \cdot \exp\left(-[\frac{x-N}{\sigma}]^2\right) + \alpha_{Start}$
Kaiser Bessel	$\alpha_K(x) = (\alpha_{End} - \alpha_{Start}) \cdot I_0\left(\beta\sqrt{1-(2x/N-1)^2}\right) + \alpha_{Start}$

Table 4.2: *Formulas of the three most commonly used variable flip angle schemes. I_0 stands for the zeroth order of the modified Bessel function of the first degree. Additional information can be found in [Nishimura and Vasanamala, 2000] for the linear scheme, in [Schäffter et al., 2002] for the Gaussian one and in [Le Roux, 2003] for the Kaiser Bessel scheme.*

can be applied, this is still a sizable improvement with no disadvantages and thus should not be ignored.

4.3 The Variable Flip Angle Approach

As described in the last section, the main goal of using variable flip angles was to achieve a higher signal intensity in the center of k-space by increasing the flip angle in that portion of the sequence and then lowering the flip angle in the periphery. However, this is not a trivial matter, as changes in the flip angles can lead to heavy signal oscillations and therefore artifacts in the acquired image. Thus, to achieve smooth signal transitions it is imperative to have extensive knowledge about the signal properties.

4.3.1 Different Flip Angle Schemes

Various flip angle schemes are shown in figure 4.9. Their quantitative nature is described in table 4.3. The most commonly used schemes are the linear flip angle scheme, the Gaussian scheme and the Kaiser Bessel scheme. These schemes have a number of degrees of freedom but all include the flip angle at the start α_{start}, the flip angle at the end α_{end} and the length of the ramp, given by the number of pulses N. The Gaussian and the Kaiser Bessel scheme have an additional degree of freedom describing their gradient, σ and β, respectively. Using a numerical simulation based on the Bloch-equations in matrix-form [Hargreaves et al., 2001] the signal modifications for lung tissue ($T_1 = 1250\ ms$, $T_2 = 50\ ms$) was done for both on- and off-resonant signals.

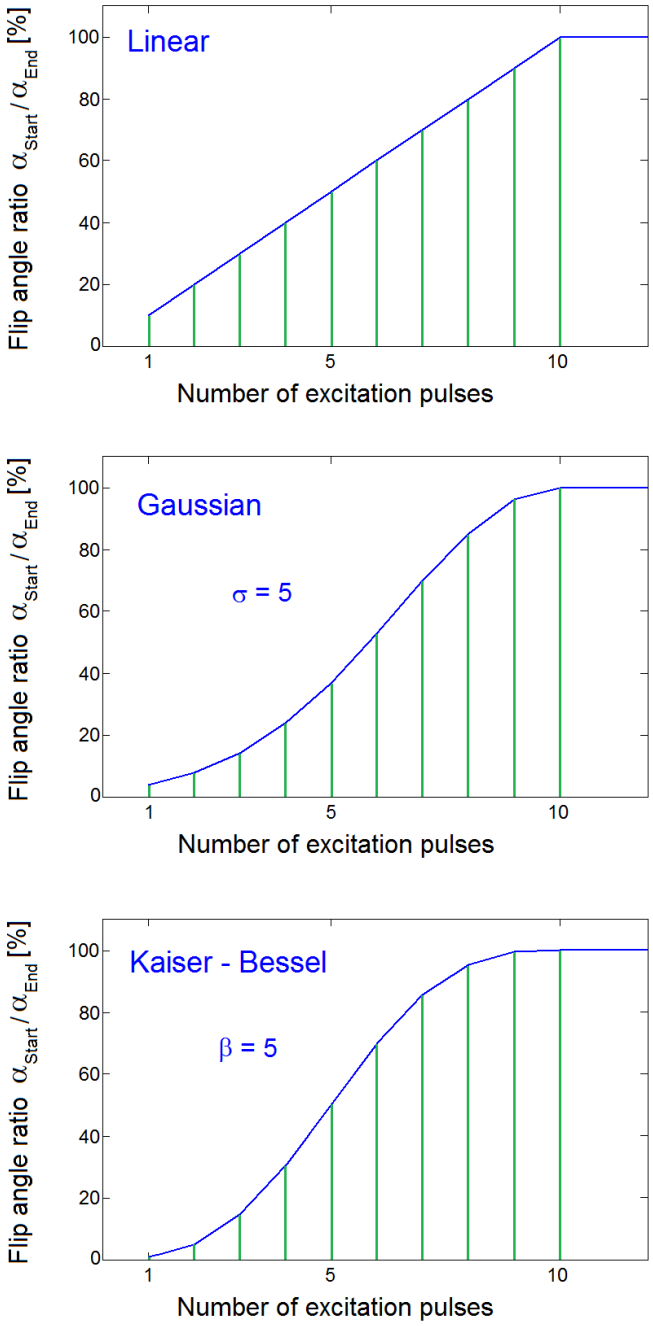

Figure 4.9: *Different flip angle schemes. The top figure shows the linear scheme, the middle one the Gaussian scheme with $\sigma = 5$ and the bottom picture shows the Kaiser Bessel scheme with $\beta = 5$. All preparation schemes were simulated using 10 pulses which are shown as green pillars. The enveloping function is shown in blue.*

To quantify the quality of the flip angle scheme as preparation, the signal oscillation index (SOI) was used [Deshpande et al., 2003]. The SOI compares the signal of n pulses after the

ramp to its nearest neighbors

$$SOI = \sum_{k=m+1}^{m+n+1} |S_k - 0.5 \cdot (S_{k-1} + S_{k+1})|. \tag{4.10}$$

n is commonly set to 10. The SOI depends on both relaxation times and other sequence parameters (such as voxel size). As such it is a relative value and can only be used to compare measurements with the same boundary conditions. The porcine lung phantom, with its breathing pump turned off, was used to test the various flip angle schemes.

4.3.2 Additional Parameters

As discussed beforehand both the Gaussian scheme and the Kaiser Bessel scheme have an additional parameter to describe their gradient. Before comparing the schemes to one another, these values have to be set correctly to enable a fair comparison. To achieve this, a simulation of the SOI for both preparation schemes was performed for $0.1 \leq \sigma \leq 20$ and $0 \leq \beta \leq 20$, respectively. The other sequence parameters were; $T_1 = 1250\ ms, T_2 = 50\ ms$, $TE/TR = 0.8/1.9\ ms$, $TW = 200\ ms$, $\alpha_{Start} = 0$, $\alpha_{End} = 90°$ and $N = 10$. The result of these simulations can be seen in figure 4.10. The SOI of both schemes follows a similar trend with a broad minimum in the middle and high SOI near the edges. The absolute minimum of the Gaussian preparation is near $\sigma \approx 3.7$ and for the Kaiser Bessel preparation near $\beta \approx 5.2$. As both minimums are fairly broad, the exact values do not matter, as long as values are chosen near the minimum. However, it should be noted that the Gaussian scheme is much less stable for values near zero as this essentially means no preparation at all. $\beta = 0$ on the other hand still leads to a linear preparation scheme, which performs much better. Further simulations for different tissue parameters T_1 and T_2 showed only a weak dependence of both σ and β on them and no change in the general trend. Changing the number of preparation pulses N revealed the same result. Changing α_{Start} and α_{End} did not influence the position of the minimum of the shape of the graph at all. It did however change the absolute values of the simulated SOI. As intuitively expected a smaller difference between α_{Start} and α_{End} leads to smaller signal oscillations and thus a smaller SOI.

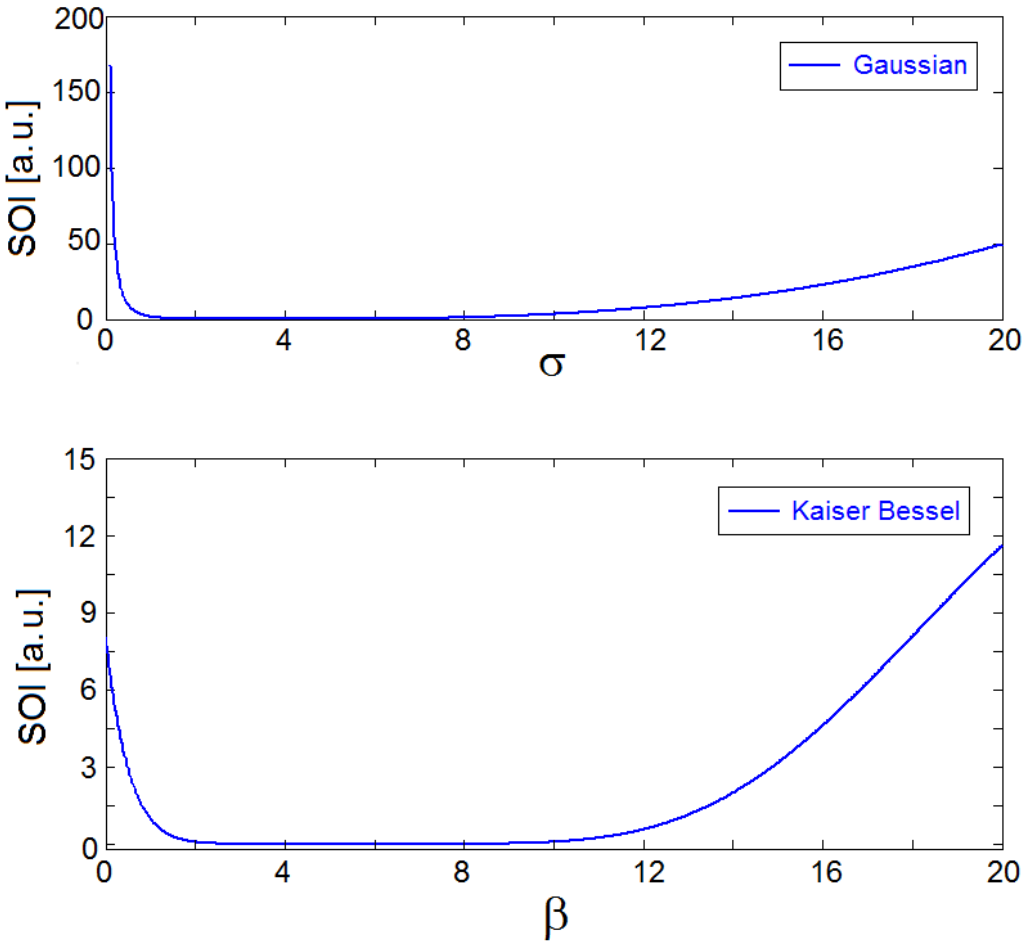

Figure 4.10: *Additional parameters for variable flip angle schemes. The Gaussian scheme (top) has a broad minimum for* $2 \leq \sigma \leq 6$ *with an absolute minimum near sigma* $= 3.7$*. The Kaiser Bessel scheme (bottom) has a broad minimum between* $3 \leq \beta \leq 8$ *with an absolute minimum near* $\beta = 5.2$*.*

4.3.3 The Optimal Preparation Scheme

After determining the optimal parameters for σ and β it was possible to investigate, which preparation scheme should be chosen to optimally prepare the magnetization before the measurement starts. In [Bauman, 2010] a linear preparation ramp was used. Table 4.3 shows the results for all three preparation schemes, both for on-resonant signals ($\Delta\omega = 0$) and for off-resonant signals within the pass band ($\Delta\omega = \pm 60\ Hz$). The results were further compared to the SOI of a simple $\alpha/2$ preparation.

The simulations were done for the timing parameters of $T_1 = 1250\ ms$, $T_2 = 50\ ms$, $TE/TR = 0.8/1.9\ ms$ and $TW = 200\ ms$. The flip angles were chosen to be $\alpha_{Start} = 0°$ and $\alpha_{End} = 90°$. Three ramp lengths were tested with $N = 5, 10, 15$, respectively. The additional parameters σ

Scheme	Ramp length N	$\Delta\omega = 0$ Hz	$\Delta\omega = \pm 60Hz$
$\alpha/2$	-	0.0	100.0
Linear	5	174.8	133.6
	10	8.2	54.3
	15	7.0	13.9
Gaussian	5	15.9	108.5
	10	3.6	8.2
	15	2.4	3.4
Kaiser Bessel	5	5.3	18.5
	10	1.2	1.4
	15	0.9	1.3

Table 4.3: *SOI values for different preparation schemes. The values for the off-resonant signal of the $\alpha/2$ pulse was set to 100 to enable a better comparison between the schemes. As expected the longer ramps perform better than the shorter ramps. For the simulated parameters, the Kaiser Bessel pattern outperforms the Gaussian one, while the Gaussian outperforms the linear pattern.*

and β were set to the absolute minimums found in the last section ($\sigma = 3.7$, $\beta = 5.2$).

The simulation shows that the $\alpha/2$ preparation perfectly prepares a fully on-resonant signal (SOI = 0.0). However, signals like those do in practice not exist, especially in the lung with its highly heterogeneous structure. For slightly off-resonant signals in the pass band the $\alpha/2$ preparation fares much worse. The values of this SOI was normalized to 100.0 to enable a easier comparison with the other preparation patterns. A short linear preparation $N = 5$ fares worse than the $\alpha/2$ preparation with SOIs larger than 100 for both on and off-resonant signals. However, with larger ramps of $N = 15$ this can significantly be reduced to 7.0 and 13.9 for on- and off-resonant signals, respectively. The Gaussian preparation fares similarly but slightly better. The SOI for larger ramps ($N = 10, 15$) is $2 - 3$ times lower for on-resonant signals and $4 - 6$ times lower for off-resonant signals. The Kaiser Bessel pattern performs the best by a significant margin. Even for the shortest simulated ramp ($N = 5$) it shows comparable values to the linear preparation of three times its length. For longer ramps it beats out the Gaussian scheme by a factor of around 2 for on-resonant signals and a factor $3 - 6$ for off-resonant signals. It should be noted however, that the increase in ramp length from $N = 10$ to $N = 15$ barely has any effect on the remaining SOI. Thus, for this application, which has to be performed with acquisition times of around 3 images per second, it would not make any

sense to rely on ramps that are significantly longer than 10 steps. Compared to the original linear 10 step preparation used in [Bauman, 2010], the Kaiser Bessel preparation lowers the signal oscillations by a factor of 7 for on-resonant signals and a factor of 39 times. This is a very important result, as combined with the centric reordering mode, the likelihood of artifacts especially in the lung is reduced by a significant margin.

4.3.4 Changing the Flip Angle During Acquisition

The idea of variable flip angles was not just proposed to enable a better preparation. The main focus instead was the reduction of the SAR, which in turn could then be used to increase the flip angle and increase the SNR of the sequence. However, this required a switch between flip angle levels from a high flip angle in the center of k-space towards a lower one in the periphery. The goal of this section was to determine which preparation would be best suited to avoid signal oscillations during the switch. For this purpose the three previously discussed flip angle schemes (linear, Gaussian and Kaiser Bessel) were simulated for a transition between $\alpha_{Start} = 90°$ and $\alpha_{End} = 30°$. The signal oscillation index was computed for 20 pulses starting from the first one of the ramp and the length of the ramp was set to $N = 10$. The timing parameters of the sequence were the same as in the last section, $T_1 = 1250\ ms, T_2 = 50\ ms$, $TE/TR = 0.8/1.9\ ms$ and $TW = 200\ ms$. Figure 4.11 shows both the flip angle pattern and the resulting signal oscillations caused in the measurement. As expected from the previous section, the signal oscillations were smallest using the Kaiser Bessel scheme. The linear pattern did the worst, especially in the case of off-resonant signals. A more complete list of results for different ramp lengths can be seen in table 4.4.

4.4 Evaluating the Modified Sequence

The flip angle scheme of the fully modified sequence, combined with a centric k-space sampling trajectory is shown in Figure 4.12. For comparison a regular sequence with a constant flip angle is also shown. It should be noted that the following results were already partially published in [Corteville et al., 2015]. Obeying this schedule, the flip angle is first initialized using a preparation ramp to reduce transient signal oscillations. During the acquisition, the flip angle is then varied in such a way that the center of k-space is sampled using a higher flip

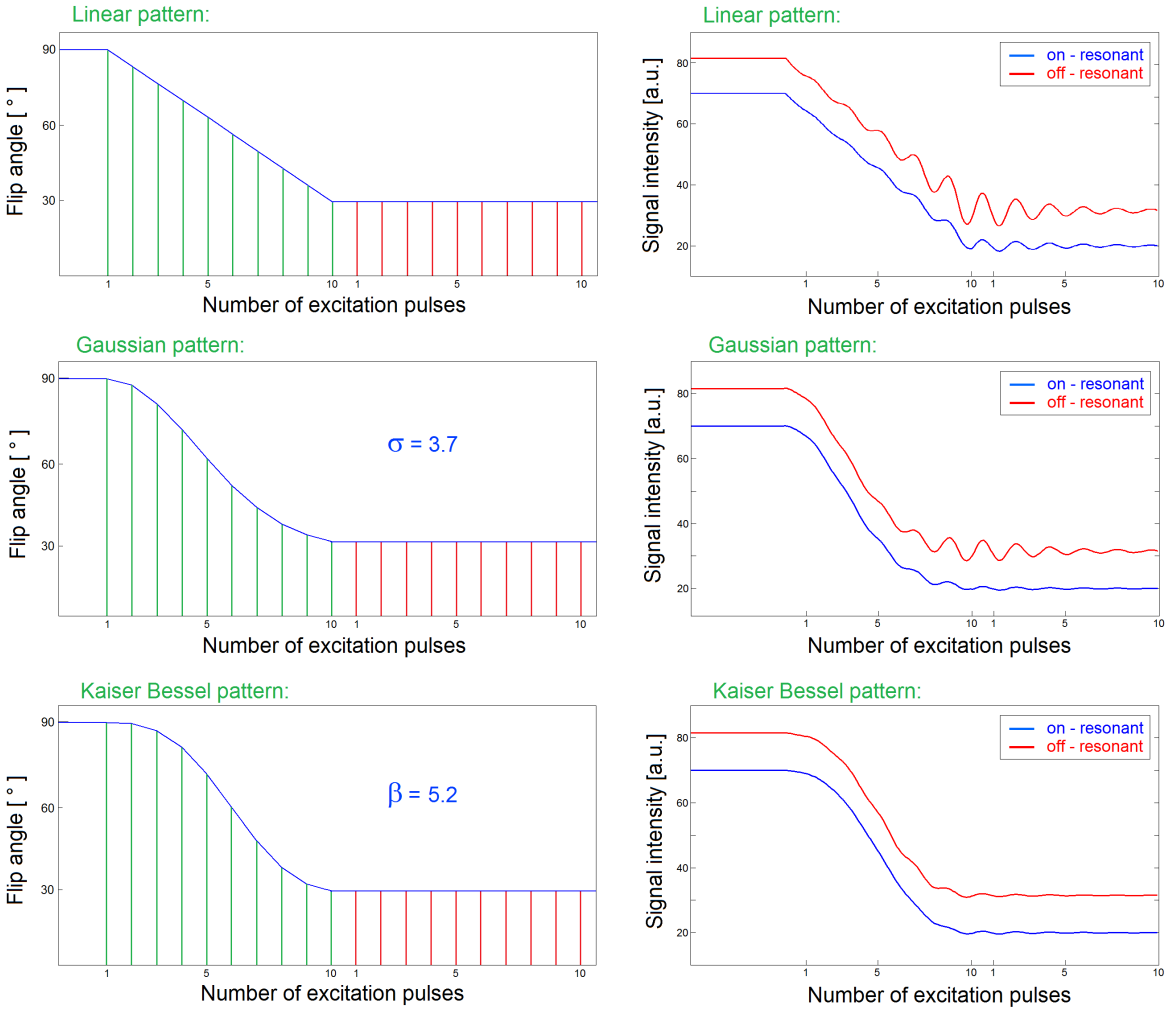

Figure 4.11: *Simulated signal intensity progression after a level switch. The flip angles were $\alpha_{Start} = 90°$ and $\alpha_{End} = 30°$. The ramp length was chosen to be $N = 10$. The off-resonant signal simulation was done at $\Delta\omega = \pm 60\ Hz$ and shifted slightly upwards to increase the visibility.*

angle α_{max}, while the periphery of k-space is sampled using a smaller flip angle α_{min}. Both the preparation ramp and the transition ramp from α_{max} to α_{min} follow the Kaiser-Bessel approach. As shown in the last section, this is the best method for both preparation of the magnetization and inducing flip angle changes during the acquisition for the set of parameters used in this work. Since the Fourier Decomposition method requires a rapid acquisition rate of at least three images per second to sample the human heartbeat the use of parallel imaging techniques is necessary. In this study we used the generalized auto-calibrating partially parallel acquisition technique (GRAPPA) [Griswold et al., 2002] with an acceleration factor of 3 and 24 reference lines. The technique is described in detail in the method section. As using variable

Scheme	Ramp length N	$\Delta\omega = 0$ Hz	$\Delta\omega = \pm 60Hz$
Linear	5	370.4	242.1
	10	21.2	100.6
	15	7.8	20.1
Gaussian	5	35.2	210.8
	10	11.1	22.9
	15	5.9	7.1
Kaiser Bessel	5	18.3	55.0
	10	3.8	4.3
	15	1.9	2.3

Table 4.4: *SOI values for different flip angle schemes after a level switch. As expected the longer ramps perform better than the shorter ramps. For the simulated parameters, the Kaiser Bessel pattern outperforms the Gaussian one, while the Gaussian outperforms the linear pattern.*

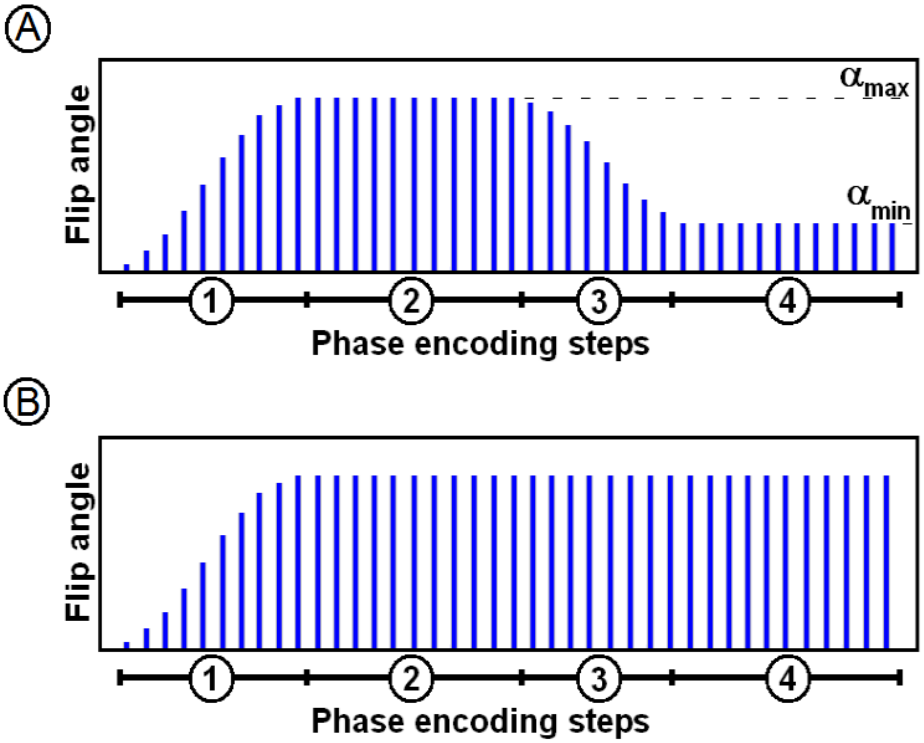

Figure 4.12: *The final flip angle scheme of the modified sequence. The modified pattern is shown in the top half of the figure (A). After a preparation ramp (1) the center of the k-space (2) is sampled with an increased flip angle α_{max}. Then the flip angle is ramped down (3) and the periphery of the k-space (4) is sampled at lower flip angle α_{min}. For reference the unmodified sequences is shown in the bottom half of the figure (B). In this version the flip angle stays the same after preparation.*

flip angles during the acquisition of the GRAPPA kernel could induce unexpected properties to the reconstruction, the flip angle was kept constant during the acquisition of the reference lines. Thus, the number of pulses in the center of k-space was chosen to be slightly higher than the number of reference lines for GRAPPA and was 27 for all variants of the modified sequence used in this work. For comparison a regular sequence with a constant flip angle of 75° was set up with similar timing parameters as the modified sequence. This flip angle is the standard for current FD proton lung imaging [Bauman, 2010]. The unmodified sequence is further referred to as M0, while the modified sequences are given higher indexes. The flip angle α_{max} was chosen in such a way, that the modified sequence, using the same timing as the regular sequence, reached the same exact SAR values. Therefore, the only parameters that further influence the SAR are the ramp length and the minimum flip angle α_{min}. Independent of the flip angles that were used, all excitation pulses had the two speed VERSE shape discussed in section 4.3 and a pulse duration of 1250 μs. For higher flip angles, only the amplitude of the pulses was modified. For a further systematic investigation, 12 variants of the fully modified sequence were taken into account. A list of all considered variants and the corresponding α_{max} can be seen in table 4.5. The parameter sets are labeled as M1 - M12 in the following to accomplish easier referencing.

4.4.1 Simulations

To test the properties of the finished sequence a set of simulation was conducted. It should be noted that the variable flip angle approach has a slight disadvantage, which is lowering the acquired signal in the periphery of the k-space. This in turn lowers the resolution of the image and can introduce blurring artifacts. To prevent this effect from causing any noticeable image degradation a simulation for the point spread function (PSF) was performed using propagation of the Bloch equations. Additionally, another simulation was performed to estimate the SNR increase achieved by employing the variable flip angle pattern. The parameters used in the simulation were the same as in the subsequent measurements, to be specific $TE/TR/TA = 0.6$ $ms/1.4$ $ms/97$ ms. The tissue parameters of the simulation were set to be to be $T_1 = 1300$ ms and $T_2 = 50$ ms. The effect of the variable flip angle approach on the PSF can be quantified by its full width half maximum (FWHM). Figure 4.13 shows the FWHM for the different parameter settings.

Modification	Ramp length	α_{min} [°]	α_{max} [°]
M0	-	75	75
M1	8	10	133
M2	16	10	120
M3	24	10	109
M4	32	10	100
M5	8	25	112
M6	16	25	104
M7	24	25	98
M8	32	25	92
M9	8	50	96
M10	16	50	92
M11	24	50	89
M12	32	50	86

Table 4.5: *Sequence settings for the variable flip angle scheme. The settings for the modified sequences are labeled M1-M12, while the standard sequence is labeled M0. The listed properties include ramp length, flip angle in the periphery of k-space (α_{min}) and flip angle in the center of k-space (α_{max}).*

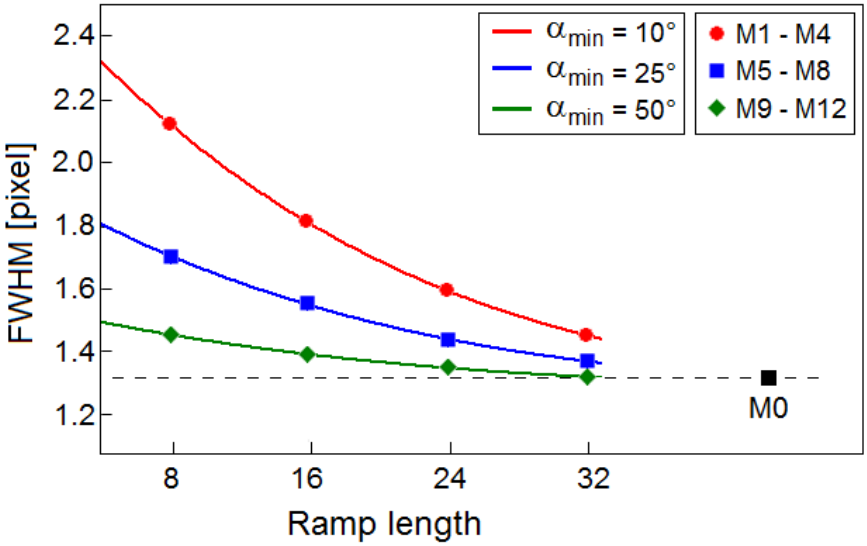

Figure 4.13: *Dependence of the PSF on the sequence parameters. While the technique always broadens the PSF, the severity strongly depends on the sequence parameters. For the variants M12 through M7 the broadening is only slight (between 2 and 5%), while other parameter sets increase the FWHM noticeably by between 9% (M6) and 47% (M1).*

It can be observed that, independent of the parameter settings, the PSF is always broadened by the technique. However, for the variants M7 through M12 the broadening is only slight (between 2 and 5%). For all other parameter sets the FWHM is increased noticeably by between 9% (M6) and 47% (M1). Figure 4.14 shows the simulated SNR gain using variable flip angles. The SNR is increased by between 23% and 41% and shows a similar distribution compared to the flip angle at the center of k-space α_{max}.

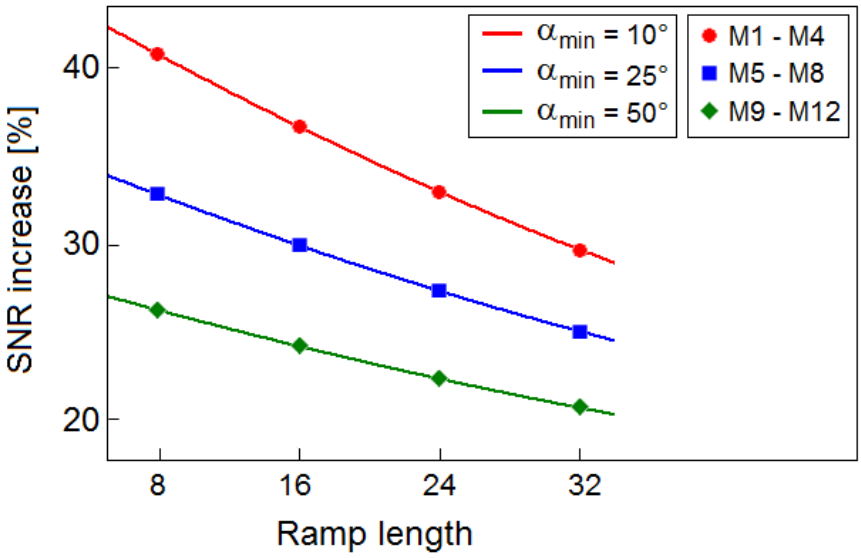

Figure 4.14: *Simulated SNR increase depending on sequence parameters. The SNR is increased by between 23% and 41% for different sequence parameters. It shows a similar distribution compared to the flip angle at the center of k-space α_{max}.*

4.4.2 Phantom Study

Additional to the simulations a phantom study was conducted. The parameters used were the same as in the simulation, $TE/TR/TA = 0.6/1.4/97\ ms$. The phantom used in this measurement had to have specific and well known properties in order to identify and quantify possible artifacts. Thus, the porcine lung phantom was not optimal for this measurement. In order to achieve the necessary specificity, a sponge phantom was built in-house to mimic the heterogeneous properties of lung tissue. An image of the used phantom can be seen in the method section, while a high resolution MR image of the phantom outlining the coarse and the fine profile can be seen in figure 4.15. The size of the sponge was $10 \times 25\ cm^2$ and the used straws had a diameter of 5 mm and 15 mm, respectively. The sponge phantom was filled with a mixture of water and contrast agent to achieve similar T_1 and T_2 times to the lung parenchyma.

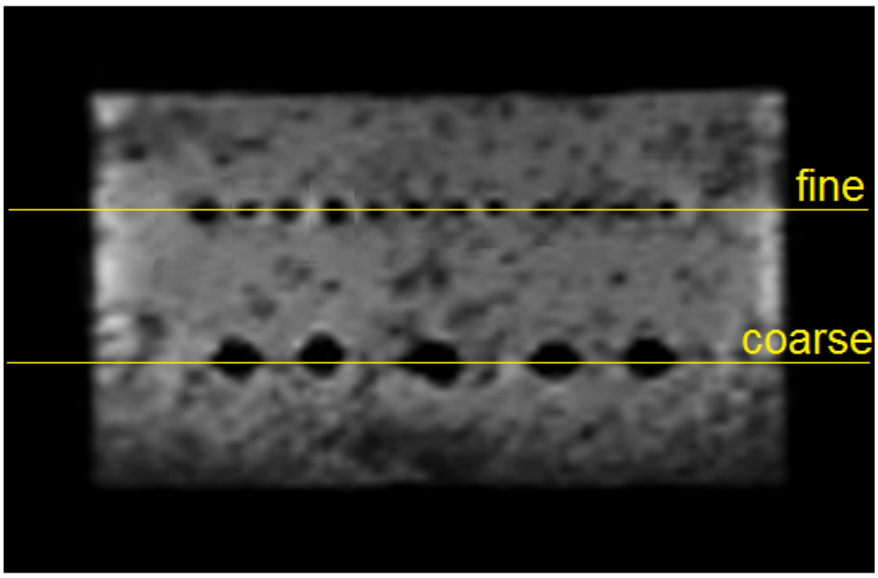

Figure 4.15: *High resolution MR image of the sponge phantom. The yellow lines indicate the evaluated fine and coarse profiles. The diameters of the straws used to make the profiles were 5 mm and 15 mm, respectively.*

The relaxation times were measured using standard techniques, IR-HASTE for T_1 and T_2-prep SSFP for T_2 [Wild et al., 2012]. To ensure stable conditions, these measurements were done twice, once before obtaining the bSSFP images and once afterwards. The results for T_1 were (1240±90) ms before the measurement series and (1270±80) ms afterwards. The results for T_2 were (40±40) ms before the measurement series and (60±50) ms afterwards. The large errors, specifically for T_2 are due to the heterogeneous structure of the phantom mimicking the lung. The prepared properties are in good agreement with the expected T_1 = (1200 - 1500) ms and T_2 = (30 - 70) ms of the human lung [Kauczor, 2009]. For all experiments the investigated straw profile was lined up in phase encoding direction. The geometric parameters of the imaging sequence were set to be equal to what is used in human measurements, specifically FOV = 450 × 450 mm^2, slice thickness = 10 mm and matrix size = 128 × 128. Thus, the resolution of the measured images was 3.5 × 3.5 × 10 mm^3. The modified bSSFP sequence acquired 200 images with an inter image delay of 200 ms. Therefore, the total acquisition time was roughly one minute per series. The relative SNR of the phantom measurements was analyzed using two regions of interest (ROI), one set inside the phantom and a second was placed away from the object. Since the measurements used the sum of squares coil combination mode, spatially inhomogeneous noise could only originate from noise correlations between the coils, which are typically low [Dietrich et al., 2008]. To account for signal variations within the phantom, the

ROIs were positioned in the same locations for all measurements. The relative SNR was then calculated as the mean signal divided by the standard deviation of the noise. The result of this measurement can be seen in figure 4.16 where it was compared to the previously performed simulation.

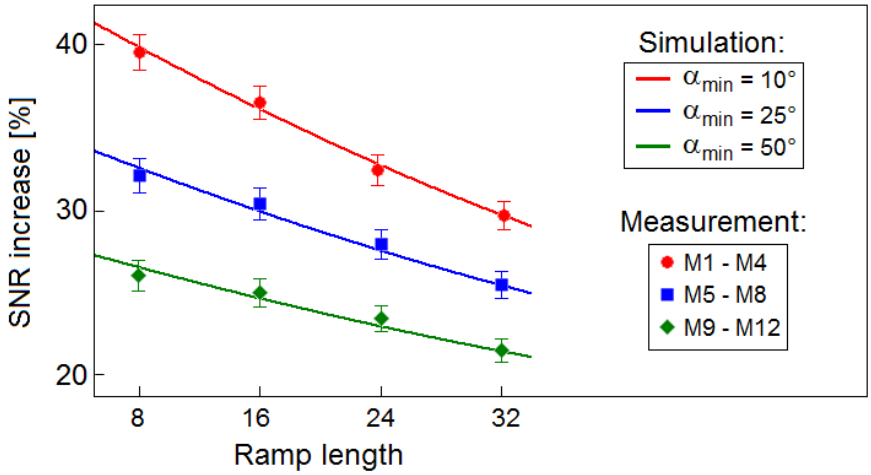

Figure 4.16: *SNR increase based on different sequence parameters measured in the sponge phantom. The phantom measurement is in good agreement with the simulation.*

The resolution degradation and blurring was investigated using both a coarse and a fine predefined profile of the phantom. As there was no water present at the position of the straws the signal should be zero. To determine how well the respective modified sequences were able to resolve these profiles, the signal at the position of the straws was evaluated and compared to the standard sequence (M0). The difference between the value of M0 and the examined variants of the modified sequence (M1−M12) at the position of the straws was voxelwise added up using a sum of squares difference. This combined value is further referred to as signal difference and can be used as an indication for blurring artifacts in the images. High values indicate a loss of resolution due to blurring, whereas values close to zero indicate no blurring and thus similar resolution to the standard sequence. Figure 4.17 shows both the fine and the coarse profile for three exemplary sets of sequence parameters (the standard sequence M0, a modification of medium magnitude M7 and a modification of high magnitude M1). It is clearly visible that M7 can resolve both profiles just as well as M0. M1 however, can only resolve the coarse profile and blurs the intensity of adjoining structures into the gaps.

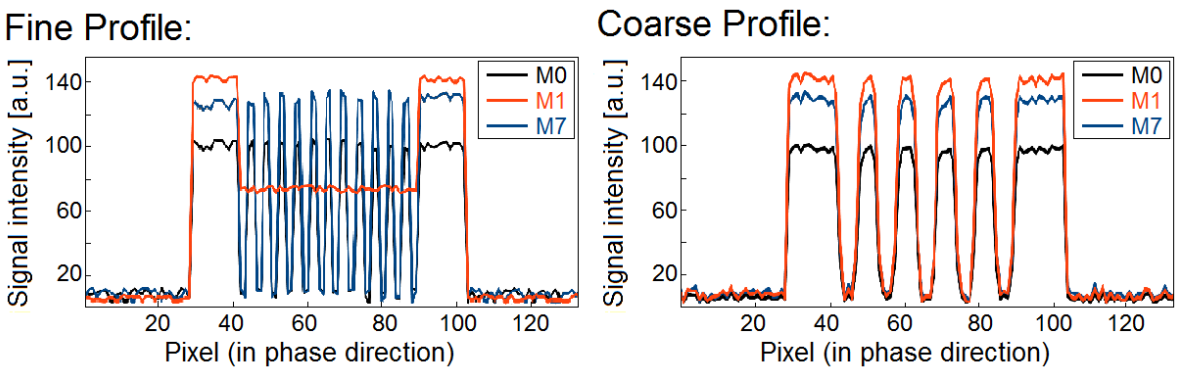

Figure 4.17: *Profiles of the sponge phantom imaged with three exemplary sets of sequence parameters. The standard sequence M0 and the modification M7 are able to resolve both profiles. The modification M1 can only resolve the coarse profile.*

A complete evaluation of the signal difference at the position of the straws for both the fine and the coarse profile is shown in figure 4.18. It shows that only the settings M7−M12 reach similar resolutions to the standard sequence. The settings M1−M6 on the other hand, are unable to resolve the fine profile. However, the resolution is only slightly impaired as all variants including M1 were able to resolve the coarse structure. While the SNR is steadily increasing depending on the flip angle in the center of k-space, the parameters indicating resolution show an increasing disparity between the standard sequence and the variants M1−M6.

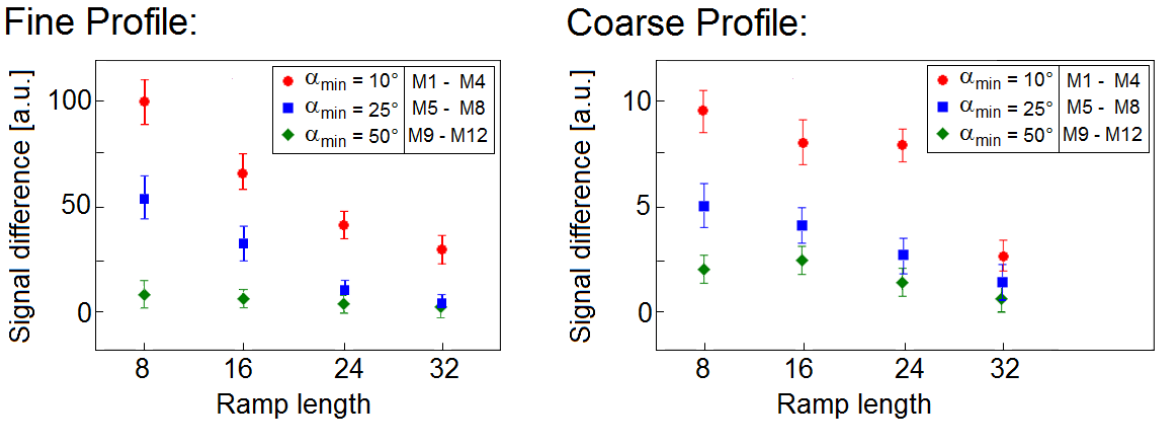

Figure 4.18: *Signal difference at the position of the straws compared for all sequence variants. While the modifications M7−M12 reach similar resolution levels as M0, the modifications M1−M6 are only able to resolve coarse structures.*

4.4.3 Volunteer Study

Finally, the sequence was tested in a volunteer study. For all measurements in the study, the necessary inter image delay was minimized until the individual SAR limit of the volunteer was reached. For the investigated volunteers, which were all males of normal weight and height this delay was between 150 ms and 180 ms. In total six healthy volunteers with an age of (27.5 $\pm$ 7.0) years underwent lung imaging. The imaging parameters were $TE/TR/TA$ = 0.6/1.4/97 ms. An asymmetric readout was used with a relative echo position of $\lambda = 22.5\%$. The geometric parameters were FOV = 450 $\times$ 450 mm^2, slice thickness = 10 mm and matrix size = 128 $\times$ 128, thus the resolution was 3.5 $\times$ 3.5 $\times$ 10 mm^3. 200 images were acquired, so the total acquisition time was roughly one minute per series. To obtain the functional images the standard FD method [Bauman et al., 2009] was applied: Briefly, the respiratory motion of the acquired data-sets was compensated using a two-dimensional non-rigid image registration algorithm [Chefd'hotel et al., 2002]. Thereafter, a Fourier analysis was conducted to find the periodic signal intensity changes caused by the cardiac and the respiratory cycles. Integration of the corresponding spectral lines provided the VW and QW images. The relative SNR was analyzed using regions of interest (ROI) within the lung parenchyma. To estimate the noise level a second ROI was placed outside of the volunteer. To account for signal variations within the volunteers, the ROIs were all positioned in the same locations. For the volunteers the ROI was set in the top lobe of the right lung. The SNR was then calculated as the mean signal divided by the standard deviation of the noise. The SNR of the resulting ventilation and perfusion images was obtained from ROIs that were positioned similarly. Figure 4.19 shows exemplary results of the volunteer study. The figure shows both morphological and functional images obtained by the standard sequence and the variants M1 and M7. The graphs in figure 4.20 take the data acquired of all six volunteers into account. Results show that the SNR benefits from shorter ramps and lower flip angles in the periphery of k-space, while the resolution suffers slightly for the more radical modifications M1$-$M6. The SNR gain of the morphological images and the functional images is similar for all variants and corresponds well with the findings in the simulation and the phantom. In addition to this, another effect is noticeable in the functional images. Due to the higher signal of the source data a better distinction of the perfusion and ventilation signals of smaller structures is possible. This leads to a higher effective resolution in the functional images.

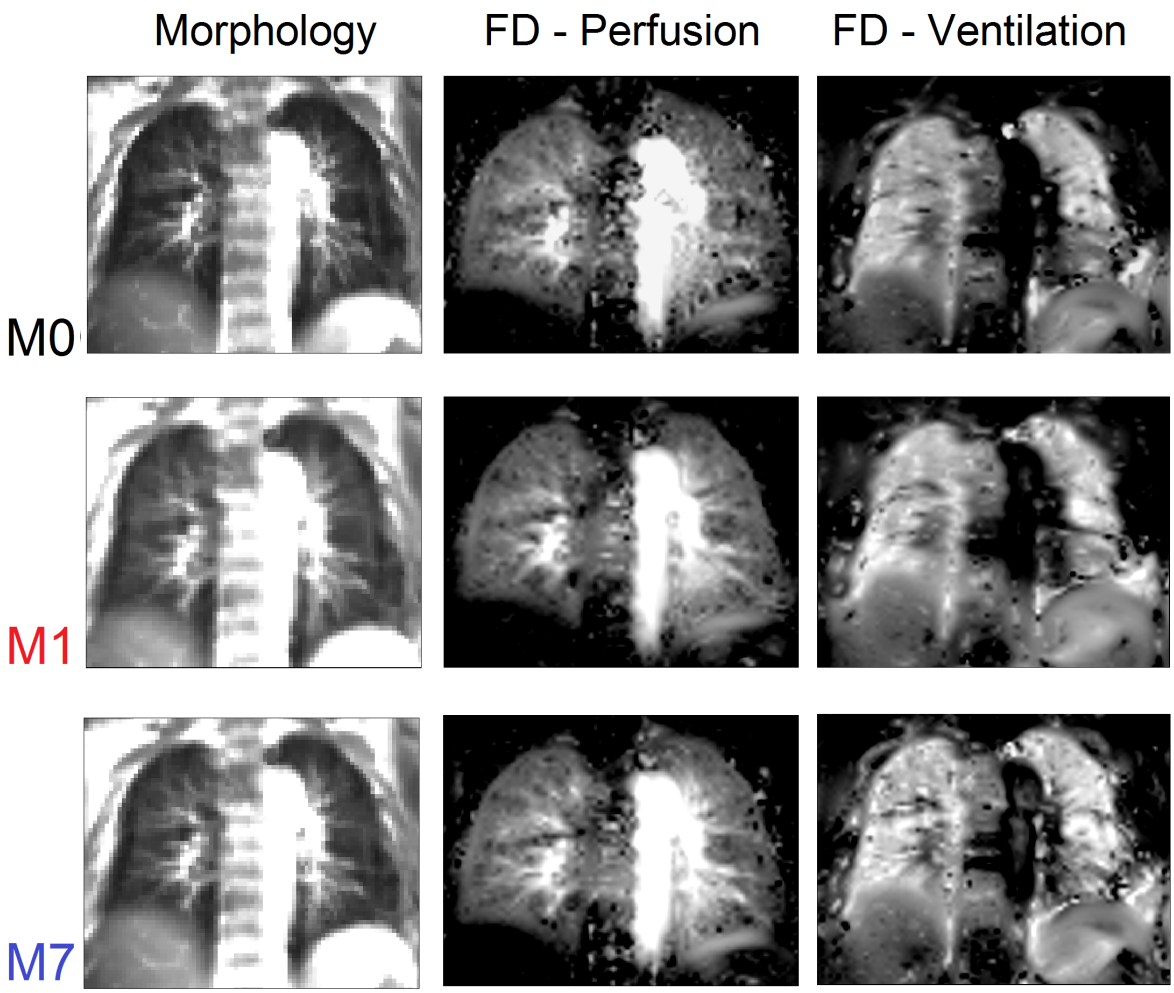

Figure 4.19: *Exemplary morphological and functional images of a volunteer. While M1 shows higher signal gains compared to M7, it also shows blurring artefacts in the functional images. M7 on the other hand even shows smaller structures in the functional images than M0.*

4.4.4 Patient Study

A recent study conducted on lung cancer patients [Kjørstad et al., 2015] using the previously described modified sequence, allowed the comparison of the modified sequence to the standard sequence in patients. Image series were acquired using the modification M7 and the standard sequence M0. While the healthy lung of the patients showed a similar signal increase compared to the healthy volunteers of around $34 \pm 3\%$, the situation in the afflicted lung was not as clear. Mean signal increases of as low as 23% and as high as 45% were measured in the afflicted parenchyma. Arguably, this effect does not indicate a problem with the sequence modification but instead with the medical properties of the tumors. Two examples for different patients can be seen in 4.21 and 4.22.

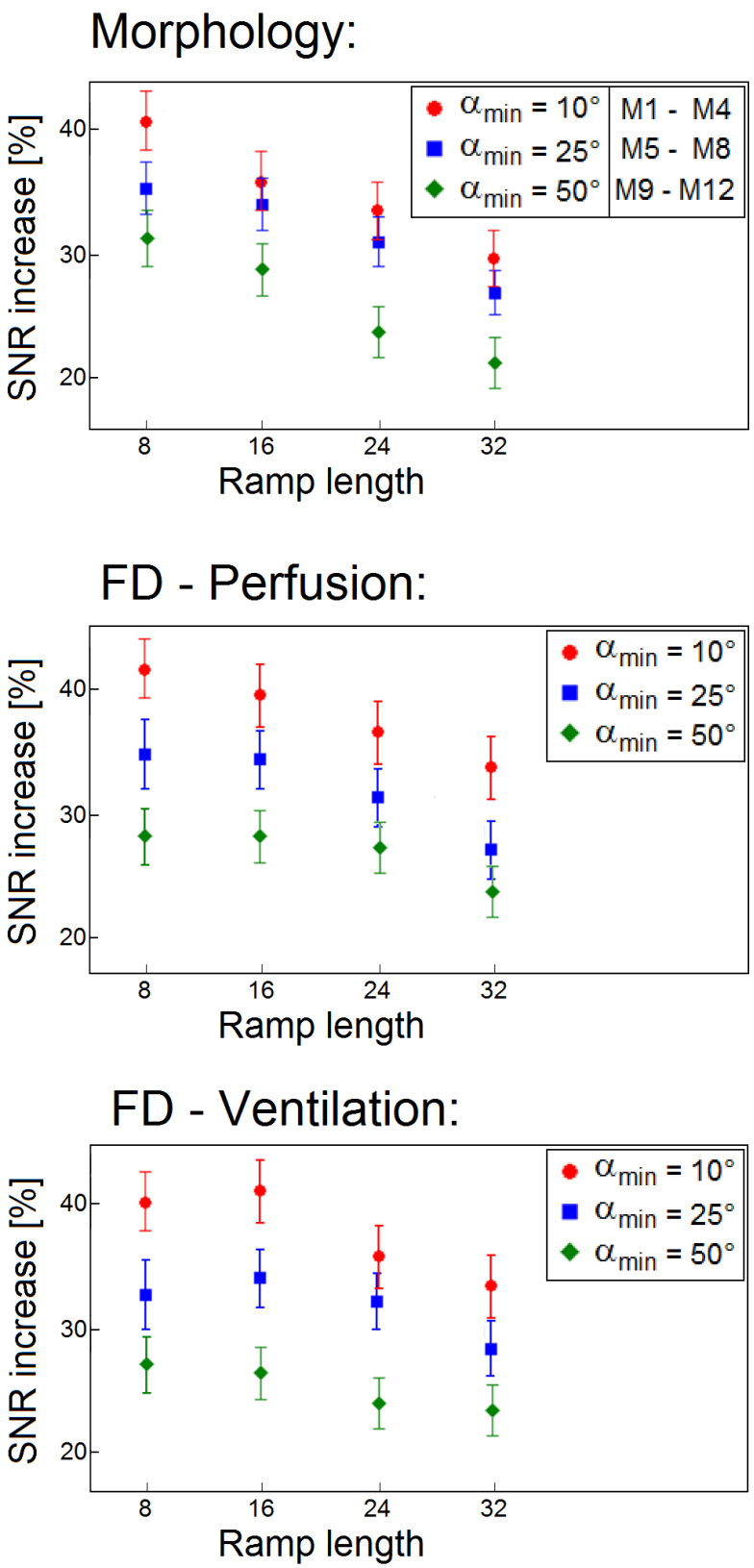

Figure 4.20: *Morphological and functional SNR gains depending on the sequence parameters M1−M12.*

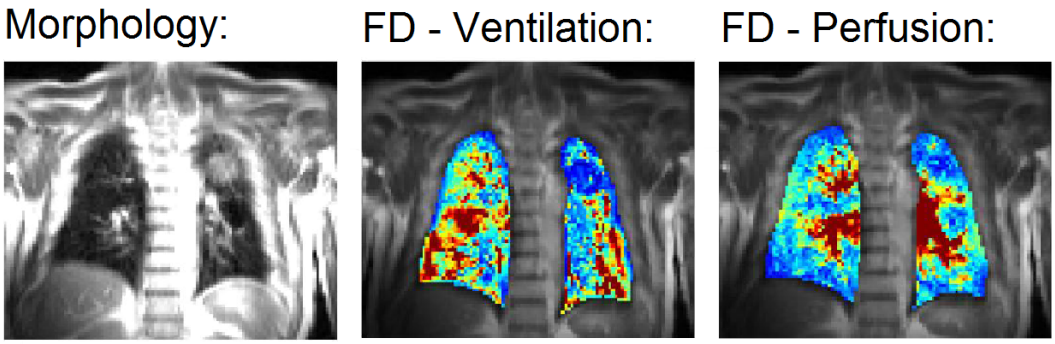

Figure 4.21: *Exemplary image of a lung cancer patient. The tumor is clearly visible in the anatomical image (left). It is located in the top left lung of the patient. The ventilation image (middle) shows a clear and very localized reduction of ventilation in the tumor area. The perfusion image (right) shows only a slightly reduced perfusion in the tumor.(Functional reconstruction courtesy of Åsmund Kjørstad.)*

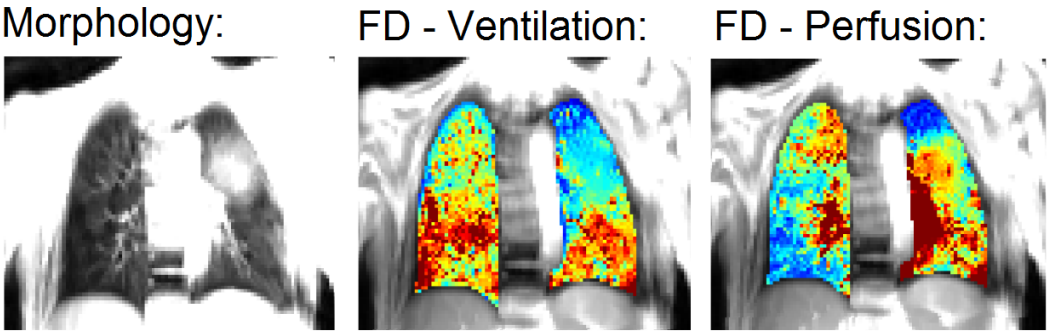

Figure 4.22: *Exemplary image of a lung cancer patient. The tumor is clearly visible in the anatomical image (left). It is located in the top left lung of the patient. The ventilation image (middle) shows reduced ventilation in and around the tumor area. The perfusion image (right) shows increased perfusion in the tumor, while the perfusion above the tumor area is reduced due to restructuring of the blood flow. (Functional reconstruction courtesy of Åsmund Kjørstad.)*

As the tumor and the tissue surrounding it have very different properties (T_1, T_2, T_2^*) compared to the healthy lung parenchyma, investigating them obviously yields different results. However, damaged lung tissue due to pulmonary edema, tumors or necrotic tissue usually yields higher signal intensity compared to the healthy parenchyma. Thus, a signal increase is not as crucial to identify this specific pathology. After excluding the tissue around the tumors, the mean signal increase in the afflicted lung was $36 \pm 7\%$.

5 Discussion

The goal of this work was to increase the usability of the Fourier Decomposition (FD) method developed by [Bauman, 2010]. For this purpose, the standard balanced steady-state free precession (bSSFP) sequence was modified to increase the signal to noise ratio (SNR) in the lung parenchyma. A series of advanced modification techniques were employed to reach this goal. In the following section the results obtained from these sequence modifications are discussed.

(Ultra-)fast bSSFP

One of the main reasons why obtaining signal from the lung parenchyma using proton MRI is difficult, are its large susceptibility changes. This intrinsic heterogeneity strongly influences the MR properties of the lung. While both a T_1 of around $1200 - 1500\ ms$ and a T_2 of around $40 - 60\ ms$ at 1.5 Tesla are not uncommon, a striking feature of the lung is its extremely low T_2^* of approximately 1 ms [Hatabu et al., 1999].

As FD lung MRI relies on sequences with very fast image acquisition times to sufficiently map the heartbeat of the human patients, fast gradient echo sequences such as bSSFP have to be used. The signal acquired with these sequences however, decays with T_2^*. Thus, with the fastest echo times of conventional bSSFP sequences being around $0.8 - 0.9\ ms$, roughly 60% of the available signal is already decayed before the acquisition starts.

To alleviate this effect, much work has been done to reduce the echo times of SSFP sequences. One of the most successful approaches was the recently developed (ultra-)fast bSSFP [Bieri, 2012]. This approach relies on strongly asymmetric readouts to both shorten the echo time and the repetition time of SSFP sequences. However, it should be noted that the technique was proposed for structural proton lung imaging and thus largely ignored small streaking artifacts

caused by highly asymmetric readouts. While these artifacts are insignificant, if the main aim is obtaining structural information of the blood vessels in the lung, this is not the case when investigating the lung parenchyma. Thus, it was imperative to minimize these artifacts before the technique could be included in the sequence used for functional FD MRI.

Conducting a series of measurements on an ex-vivo porcine lung phantom it could be shown, that extremely asymmetric echoes with an echo position of lower than $\lambda = 15\%$ would lead to large streaking artifacts in the image. However, the strong asymmetric echoes as proposed by [Bieri, 2012] using an echo position of between $\lambda = 15 - 20\%$ would still lead to measurable streaking artifacts. As the FD method relies on strict separation of the signal of the blood vessels and the parenchyma, this was deemed unacceptable. Asymmetric readouts with $\lambda > 22.5\%$ fulfilled the criteria of not causing any noticeable streaking artifacts and thus, the sequence was modified to employ an asymmetric readout with $\lambda = 22.5\%$.

Using these timing improvements, the sequence was modified to $TE/TR = 0.6/1.7\ ms$ (λ=22.5%). The original sequence used for FD lung MRI used the timing parameters $TE/TR = 0.8/1.9\ ms$ (λ=40%) [Bauman, 2010]. In conclusion, shortening the echo time of the bSSFP sequence using asymmetric readouts lead to a signal gain in the lung parenchyma of $16 \pm 2\%$.

Optimization of the shape of the excitation pulses

Besides the echo time, the second parameter that heavily influences the SNR of an image of the human lung acquired with a bSSFP sequence, is the flip angle α. Due to the semi-transient behavior of the bSSFP sequence used for FD lung MRI, estimations to determine the optimal flip angle based on commonly used steady-state formulas are generally incorrect. As such an accurate simulation had to be developed to determine the optimal flip angle α and its optimal shape.

The previously developed simulation in [Bauman, 2010] explained the discrepancy from the steady-state expectation solely by the semi-transient nature of the sequence. Due to the wait time after the acquisition of each image the sequence only reaches a pseudo steady-state.

However, this is not completely accurate. While the semi-transient behavior is the dominating factor for the lower range of flip angles $0° < \alpha < 75°$, it can not explain the signal behavior in the high flip angle range $\alpha > 100°$.

After a close inspection of the simulation method, the main culprit for this inaccuracy was identified to be the general negligence of the duration of the RF-pulse (T_{pulse}). Especially for long pulses used to apply comparatively large portions of energy, relaxation effects during the application of the pulse have to be taken into account. This effect was modeled by splitting the RF-pulse into a series of instantaneous pulses with relaxation taking place in between. After modification of the simulation in this way, it was able to predict the signal behavior of the porcine lung phantom with very high accuracy.

The results showed, that relatively high flip angles of between $100° < \alpha < 120°$, would lead to the highest signal intensity. However, flip angles of this magnitude are impossible to reach with the standard sequence, due to specific absorption rate (SAR) constraints. Thus, two advanced methods were employed to make higher flip angles usable, while still staying within the legally required SAR restrictions.

Variable-Rate Selective Excitation (VERSE) Pulses

The first, arguably less challenging method, was changing the shape of the RF-pulse from a basic sinc-pulse to a more advanced two speed variable-rate selective excitation (VERSE) pulse. The VERSE method redistributes the power of the excitation pulse to the outer lobes and thus allows a lower amplitude in the center, which effectively lowers the SAR caused by the pulse. However, the technique is limited by the maximum gradient slew rate and the maximum gradient strength available at the scanner.

In the case of this study, the gain of using VERSE was relatively small, due to the already large usage of the gradient system. However, there was still some optimization possible. As such, the average flip angle could be increased by $4° - 5°$. In particular, the standard sequence, which before operated at a limit of 75° due to the SAR constraint, was now able to use flip

angles of up to 79°. Due to the high dependence of the signal on the flip angle, this lead to an SNR gain of around $5 \pm 1\%$. While this signal amplification is not very large on its own, it still is a sizable improvement, which can easily be combined with other techniques without any drawbacks.

Varaible flip angle approach

The main method employed to increase the usable flip angle range was the variable flip angle (VFA) approach. The basic idea behind the application of this technique was to achieve higher signal intensity in the center of k-space by increasing the flip angle during that portion of the sequence and lowering the flip angle in the periphery to fulfill the SAR constraints. However, as changes in the flip angles lead to heavy signal oscillations and thus artifacts in the acquired image, the method cannot be applied carelessly. In order to achieve smooth signal transitions and artifact free images, extensive knowledge about the signal propagation is necessary.

This work examined the three most commonly used VFA patterns. These are the linear scheme [Nishimura and Vasanamala, 2000], the Gaussian scheme [Schäffter et al., 2002] and the Kaiser Bessel scheme [Le Roux, 2003]. The first series of measurements focused on determining the most beneficial intrinsic parameters of the Gaussian and the Kaiser Bessel pattern. Both schemes have an adjustable degree of freedom (σ and β, respectively), which describes their gradient. Using a numerical simulation based on the Bloch-equations in matrix-form [Hargreaves et al., 2001], the optimal range of these parameters for FD lung imaging was determined using the signal oscillation index (SOI) [Deshpande et al., 2003].

Shape Parameters of the Gaussian and Kaiser Bessel pattern

The Gaussian and the Kaiser Bessel variable flip angle pattern both feature additional parameters influencing their shape. As the shape of the patterns directly influences their ability to suppress signal oscillations, an investigation of these parameters was necessary to ensure an optimal behavior.

The result of the measurement showed, that for the Gaussian pattern an absolute minimum

could be found near $\sigma = 3.7$, however due to the large minimum of the SOI all values in between $2 < \sigma < 6$ should fare similarly. For the Kaiser Bessel pattern the absolute minimum was found near $\beta = 5.2$. However, due to a broad minimum values in between $3 < \beta < 8$ lead to similar results. While choosing these parameters, in general the Gaussian pattern is much less stable than the Kaiser Bessel one. As such, while staying in the suggested range is beneficial for both flip angle schemes it is much more important for the Gaussian approach.

The simulation also revealed that choosing these shape parameters only had a weak dependence on the number of ramp pulses used. Furthermore, the flip angle at the start and at the end of the pattern did not influence the position of the minimum at all. Thus, values of around $\sigma = 3.7$ and $\beta = 5.2$ should always be employed, when the respective VFA patterns are used for FD lung MRI.

Signal preparation

After investigating the shape parameters, the effect of the patterns on the preparation of the magnetization was evaluated. While an improved signal preparation does not increase the SNR of the images, it does improve the stability of the images and reduces possible artifacts from signal oscillations. The standard sequence used a linear preparation ramp, however this is not optimal.

After comparing the three different preparation schemes to a simple $\alpha/2$ preparation, it was shown that the Gaussian preparation significantly outperforms the linear preparation by lowering the resulting SOI by a factor of $2 - 3$ for on-resonant signals and a factor of $4 - 6$ for off-resonant signals. However, the Kaiser Bessel performed the best, outperforming the Gaussian pattern by a factor of around 2 for on-resonant signals and a factor $3 - 6$ for off-resonant signals. As expected, larger ramps prepare the magnetization better than shorter ramps. However, the effect is small after a certain threshold. For the Kaiser Bessel ramp, the SOI does not significantly decrease anymore after enlarging the ramp past ten preparation pulses. Thus, as preparation pulses both increase the SAR of the sequence and its duration, ramps of much more than 10 pulses should be avoided as their benefit to the signal preparation is rather small.

In conclusion, compared to the original linear ten step preparation used in [Bauman, 2010], the Kaiser Bessel preparation lowers the signal oscillations by a factor of 7 for on-resonant signals and a factor of 39 times for off-resonant signals. This is a fairly important result, as combined with the centric reordering mode, the likelihood of artifacts due to signal oscillations is significantly reduced.

Flip angle changes during acquisition

Aside from the improved preparation, the VFA approach was also used to reduce the flip angle in the periphery of k-space, while increasing the flip angle in the center of k-space. This required a flip angle switch during image acquisition, which in turn always leads to image degradation and potential artifacts. Investigating the VFA patterns and minimizing the severity of these artifacts was an important part before modifying the sequence.

The results showed a similar ranking order as the preparation of the magnetization. While the Gaussian scheme significantly outperformed the linear pattern, the Kaiser Bessel scheme provided the best results. The main difference between the preparation however, was that longer ramps still improved the SOI. As such, a ramp of 15 Kaiser Bessel pulses lowered the SOI by a factor of 2 when compared to similarly shaped ramp of 10 pulses. This goes well with the intuitive expectation, as longer ramps introduce more sequential flip angle changes of a smaller magnitude. However, using longer ramps also leads to disadvantages. The difference between the maximum and the minimum flip angle is reduced for longer ramps, as a larger portion of the available SAR has to be used for the ramp.

In conclusion, a general recommendation about the ramp length is difficult and should be evaluated on a case by case basis of the application. However, one recommendation is clear. Ramps shorter than 5 pulses, independent of their shape, introduce rather large signal oscillations and should generally be avoided.

Evaluating the VFA Approach

The evaluation of the sequence using custom VFA as published in [Corteville et al., 2015], already employed the other sequence modifications. Most notably the timing change of the sequence from $TE/TR = 0.9/1.8\ ms$ to $TE/TR = 0.6/1.4\ ms$, but also the change in usage of VERSE pulses. To enable a sensible comparison, which only evaluated the relative signal gain from the VFA pattern, the sequence which is referred to as modification 0 (M0), is not the standard sequence used in [Bauman, 2010]. As such the SNR gains discussed in this section are relative improvements by only changing the flip angle pattern.

SNR increase

The flip angle of the standard bSSFP sequence for Fourier Decomposition MRI is limited to 75° due to SAR constraints. By introducing the variable flip angle approach, the maximum possible flip angle in the center of k-space depends on both the ramp length and flip angle in the periphery. The highest possible maximum flip angle was reached with a ramp length of eight pulses and a minimum flip angle of 10° (M1). The SNR, both simulated and measured in a phantom and a volunteer study, showed a steady increase corresponding to the increase of the flip angle in the center of k-space and reaches amplifications of between 22% and 41%.

Image blurring

The simulation showed that, due to the sampling of the periphery of k-space with a reduced flip angle, the point spread function gets slightly broadened. This introduces some blurring to the image. These artifacts, while harder to identify in the volunteer images, are clearly visible in the phantom data. The results show, that large structures can be resolved with all parameter sets, while fine structures are sometimes slightly blurred. However, both the results obtained from the simulation and the phantom measurement show that the settings (M7) through (M12) share a similar resolution compared to the standard sequence (M0). These sequence modifications increase the SNR in the lung parenchyma by between 22% to 33%.

Functional Images

Both, the perfusion and the ventilation maps show a similar SNR gain compared to the morphological images. The blurring artifacts introduced by the setting (M1) throguh (M6) are also present at similar magnitude compared to the morphological images. This reduces the usefulness of images acquired with these parameters. However, using the modification (M7)-(M12), the contrary effect is visible. Very fine structures that are not resolved in the functional maps acquired using the standard sequence became visible using the presented approach. Previously, these small structures were not distinguishable from the noise. This effect is dominant over the slight broadening of the PSF. This means that the parameterization (M7) - (M12) not only increase the SNR, but also the effective resolution of the functional images due to more profound distinction between perfusion, ventilation, and background signal. Subsequently, this leads to fewer artifacts (i.e. black spots) in the functional images.

In conclusion, the parameter set M7 was deemed optimal for this application. It increased the SNR in the morphological and functional images by the largest amount, $32 \pm 3\%$ and $34 \pm 5\%$, respectively. And it did not introduce any significant blurring artifacts.

Evaluation in patients

A study evaluating the sequence modification M7 and the unmodified sequence M0 in lung cancer patients, showed similar signal increases compared to the healthy volunteers, when the investigated area was limited to the healthy lung of the patients. Specifically the result in patients was $34 \pm 5\%$ compared to $32 \pm 3\%$ for healthy volunteers.

Including the afflicted lung drastically changed these results. SNR gains of as low as 23% and as high as 45% were measured for different patients. This is a result of the tumor. The tissue surrounding it has different physical properties (T_1, T_2, T_2^*) compared to the healthy lung parenchyma. Thus, it is not surprising that the modified sequence does not increase the signal in a predictable manner. After segmentation of the clearly damaged tissue in the afflicted lung and excluding it from the SNR evaluation, a more reasonable gain of around $36 \pm 7\%$ was found.

In conclusion, the patient study showed similar results to the volunteer study when limited

to tissue that seemed functionally sound. For damaged tissue both higher and lower SNR amplifications were measured. These differences are likely related to the different physical properties of the damaged tissue.

Combined Gain of all Modifications

In this thesis, two independent effects were utilized to increase the acquired signal of a bSSFP sequence. First the timing of the sequence was changed to further accommodate the short T_2^* of the lung. This lead to a signal gain of $16 \pm 2\%$ in both the morphological and the functional images. Secondly, a variable flip angle approach using VERSE pulses was developed, which increased the signal intensity of the morphological images by $32 \pm 3\%$ and the functional images by $34 \pm 5\%$.

Combined, both effects lead to an effective SNR gain of 47±5% in morphological the images and 53±7% in the functional images, when compared to the original sequence in [Bauman, 2010].

6 Summary and Outlook

The goal of this thesis was to further increase the usability of the Fourier Decomposition (FD) method by modifying and optimizing the balanced steady state free precession (bSSFP) sequence used for acquiring its source image data. This was accomplished using advanced sequence techniques, specifically (utra-) fast bSSFP employing highly asymmetric readouts, two speed variable-rate selective excitation (VERSE) pulses and variable flip angle patterns for both the preparation of the magnetization and the acquisition of the signal. Each modification was optimized using information acquired from simulations and phantom measurements. This ensured that none of the newly employed techniques introduced any kind of artifacts or blurring. The finished sequence was then tested in both healthy volunteers and in a patient study. In comparison to the standard bSSFP sequence the technique was able to improve the signal to noise ratio of the morphological images by $47 \pm 5\%$. The signal to noise ratio of the functional images fared even better and was increased by up to $53 \pm 7\%$. The signal amplification not only increased the low robustness of the technique in volunteers and patients but also helped out during to development of novel and more advanced uses of the FD method. As such, image data acquired with the newly modified sequence was used to develop quantification techniques for both ventilation and perfusion as well as advanced reconstruction schemes. One of the biggest feats of the sequence was acquiring the source data used to produce the first non-invasive, quantitative, simultaneously acquired ventilation-perfusion (V/Q) images in MRI. As such this work was very successful and provided what could be considered a crucial step towards reinforcing the position of FD MRI as an important research tool as well as bringing the technique closer towards a clinic application. However, even with all the potential of the improved sequence, the Fourier Decomposition method is currently still not robust enough to be used in a clinical environment. Specifically arrhythmic and shallow breathing as commonly encountered in patients pose unsolved problems. Additionally, even though the

signal to noise ratio of the images was significantly increased by the modified bSSFP sequence it can not be considered to be a game changer. The signal obtained from proton lung MRI is still too low to compete with other imaging modalities, that are currently considered to be the gold standard for lung imaging. As such, the goal of bringing FD lung MRI into the clinic will likely not be realized by modifying the protocol of the bSSFP sequence any further. The sequence described in this work is already highly specific and employs many cutting edge modification techniques. While certainly a few parameters could always be tweaked, especially on a patient by patient approach, such changes would hamper the general robustness. Thus, those approaches will not help to bring the method any closer towards a broad clinical application. Hardware improvements in the future might help, as faster and stronger gradients would certainly help to improve the timing of the sequence. However, due to constraints set by nerve stimulation these improvements will likely not provide the necessary boost. Another aspect that has to be considered, is that Fourier Decomposition lung MRI in its current state does not benefit from the trend to move towards higher magnetic field strengths. Higher magnetic field strengths further shorten the T_2^* of the lung parenchyma and impose stronger restrictions of the specific absorption rate, in turn limiting the range of the usable flip angles. As such field strengths of $3T$ or higher would be a hindrance and not an advantage. However, in recent years there have been advances in morphological proton lung MRI using ultrashort echo time (UTE) sequences, which are able to acquire signals instantaneously after excitation. While sequences of these types do not fit into the current framework of FD lung MRI this could be changed within a few years by both adjusting the FD framework and modifying a UTE based sequence. As UTE type sequences generally benefit from the current trend to higher field strengths, this could eventually bring proton lung MRI in general and FD lung MRI in particular into the clinic. With all of this in mind, it is clear that the FD method combined with a highly specific, modified bSSFP sequence, due to its simplicity, speed and quantitative accuracy, is already a strong research tool for advancing the boundaries of functional proton lung MRI. Furthermore, while it arguably is not ready yet, we believe that it holds enough future potential to eventually make its way into the clinic.

Bibliography

Abragam, A. (2007). *Principles of Nuclear Magnetism*. Oxford Science Publications.

Alsop, D. (1997). The sensitivity of low flip angle rare imaging. *Magnetic Resonance in Medicine*, 37:176–184.

Bauman, G. (2010). *Development of a non-Contrast-Enhanced method for spatially resolved lung ventilation and perfusion measurement using Magnetic Resonance Imaging*. Natural Sciences Dissertation, Heidelberg University.

Bauman, G., Puderbach, M., Deimling, M., Jellus, V., C., C., Dinkel, J., Hintze, C., Kauczor, H.-U., and Schad, L. (2009). Non-contrast-enhanced perfusion and ventilation assessment of the human lung by means of fourier decomposition in proton mri. *Magnetic Resonance in Medicine*, 62:656–664.

Bauman, G., Puderbach, M., Heimann, T., Kopp-Schneider, A., Fritzsching, E., Mall, M., and Eichinger, M. (2013). Validation of fourier decomposition mri with dynamic contrast-enhanced mri using visual and automated scoring of pulmonary perfusion in young cystic fibrosis patients. *European Journal of Radiology*, 82:2371–2377.

Becker, E. D. (1999). *High Resolution NMR: Theory and Chemical Applications*. Elsevier Science.

Biederer, J., Plathow, C., Schoebinger, M., Tetzlaff, R., Bolte, H., Zaporozhan, J., Meinzer, H., Heller, M., and Kauczor, H. (2006). Reproducible simulation of respiratory motion in porcine lung explants. *Fortschritte auf dem Gebiet der Röntgenstrahlen und der bildgebenden Verfahren*, 178(11):1067–1072.

Bieri, O. (2012). Ultra-fast steady state free precession and its application to in vivo 1h lung imaging. *Proceedings of the International Society for Magnetic Resonance 20*.

Bloch, F. (1946). Nuclear induction. *Physical Review*, 70:460–474.

Bracewell, R. N. (1986). *The fourier transform and its applications*. McGraw Hill.

Bro-Nielsen, M. and Gramkow, C. (1996). Fast fluid registration of medical images. *Proceedings of the 4th International Conference on Visualization in Biomedical Computing*, pages 267–276.

Brown, L. (1992). A survey of image registration techniques. *ACM Computing Surveys*, 24:325–376.

Bryan, A., Milic-Emili, J., and Pengelly, D. (1966). Effect of gravity on the distribution of pulmonary ventilation. *Journal of Applied Physiology*, 21:778–784.

Buxton, R., Frank, L., Wong, E., Siewert, B., Warach, S., and Edelman, R. (1998). A general kinetic model for quantitative perfusion imaging with arterial spin labeling. *Magnetic Resonance in Medicine*, 40:383–396.

Cahill, N., Noble, J., and Hawkes, D. (2007). Fourier methods for nonparametric image registration. *IEEE Conference on Computer Vision and Pattern Recognition 2007*, pages 1–8.

Carr, H. (1958). Steady-state free precession in nuclear magnetic resonance. *Physical Reviews*, 112:1693–1701.

Chefd'hotel, C., Hermosillo, G., and Faugeras, O. (2002). Flows of diffeomorphisms for multimodal image registration. *IEEE International Symposium on Biomedical Imaging*, pages 753–756.

Christensen, G., Song, J., Lu, W., El Naqa, I., and Low, D. (2007). Tracking lung tissue motion and expansion with invesre consistent image registration and spirometry. *Medical Physics*, 34:2155–2163.

Clarke, F. (2013). *Functional Analysis, Calculus of Variations and Optimal Control*. Springer Verlag.

Corteville, D., Kjørstad, Å., Henzler, T., Zöllner, F., and Schad, L. (2015). Fourier decomposition pulmonary mri using a variable flip angle balanced steady-state free precession technique. *Magnetic Resonance in Medicine*, 73(5):1999–2004.

Dean, E. (1985). Effect of body position on pulmonary function. *Physical Therapy*, 65:613–618.

DeGroot, M. (2004). *Optimal Statistical Decisions*. John Wiley & Sons.

Deimling, M. and Heid, O. (1994). Magnetization prepared true fisp imaging. *Proceedings of the International Society for Magnetic Resonance 2*, page 495.

Deimling, M., Jellus, V., Geiger, B., and Chefd'hotel, C. (2008). Time resolved lung ventilation imaging by fourier decomposition. *Proceedings of the International Society for Magnetic Resonance 16*, page 6197.

Deshpande, V., Chung, Y., Zhang, Q., Shea, S., and Li, D. (2003). Reduction of transient signal oscillations in true-fisp using a linear flip angle series magnetization preparation. *Magnetic Resonance in Medicine*, 49:151–157.

Dietrich, O., Raya, J., Reeder, S., Ingrisch, M., Reiser, M., and Schoenberg, S. (2008). Influence of multichannel combination, parallel imaging and other reconstruction techniques on mri noise characteristics. *Magnetic Resonance Imaging*, 26:754–762.

Ehrenfest, P. (1927). Bemerkung über die angenäherte Gültigkeit der klassischen Mechanik innerhalb der Quantenmechanik. *Physical Review*, 45:455–457.

Fain, S., Korosec, F., Holmes, J., O'Halloran, R., Sorkness, R., and Grist, T. (2007). Functional lung imaging using hyperpolarized gas mri. *Journal of Magnetic Resonance Imaging*, 25:910–923.

Fain, S., Schiebler, M., McCormack, D., and G., P. (2010). Imaging of lung function using hyperpolarized helium-3 magnetic resonance imaging: Review of current and emerging translational methods and applications. *Journal of Magnetic Resonance Imaging*, 32:1398–1408.

Ferlay, J., Shin, H., Bray, F., Forman, D., Mathers, C., and Parkin, D. (2010). Estimates of worldwide burden of cancer in 2008. *International Journal of Cancer*, 127:2893–2917.

Fourier, J. B. J. (1822). *Theorie analytique de la chaleur*. Didot.

Ganong, W. (2005). *Review of Medical Physiology*. McGraw Hill Professional.

Griswold, M. A., Jakob, P. M., Heidemann, R. M., Nittka, M., Jellus, V., Wang, J., Kiefer, B., and Haase, A. (2002). Generalized autocalibrating partially parallel acquisitions (grappa). *Magnetic Resonance in Medicine*, 47(6):1201–1210.

Gulsvik, A. (2001). The global burden and impact of chronic obstructive pulmonary disease worldwide. *Monaldi Archives for Chest Disease*, 56:261–264.

Haacke, E. M., Brown, R. W., Thompson, M. R., and Venkatesan, R. (1999). *Magnetic Resonance Imaging: Physical Principles and Sequence Design*. John Wiley & Sons.

Hahn, E. L. (1950). Spin echoes. *Physical Review*, 80(4):580.

Hargreaves, B. A., Cunningham, C. H., Nishimura, D. G., and Conolly, S. M. (2004). Variable-rate selective excitation for rapid mri sequences. *Magnetic Resonance in Medicine*, 52(3):590–597.

Hargreaves, B. A., Vasanawala, S. S., Pauly, J. M., and Nishimura, D. G. (2001). Characterization and reduction of the transient response in steady-state mr imaging. *Magnetic Resonance in Medicine*, 46(1):149–158.

Hatabu, H., Alsop, D. C., Listerud, J., Bonnet, M., and Gefter, W. B. (1999). T2* and proton density measurement of normal human lung parenchyma using submillisecond echo time gradient echo magnetic resonance imaging. *European Journal of Radiology*, 29(3):145–252.

He, J., Fang, W., Lv, B., He, J.-G., Xiong, C.-M., Liu, Z.-H., and He, Z.-X. (2012). Diagnosis of chronic thromboembolic pulmonary hypertension: comparison of ventilation/perfusion scanning and multidetector computed tomography pulmonary angiography with pulmonary angiography. *Nuclear Medicine Communications*, 33:459–463.

Hennig, J., Weigel, M., and Scheffler, K. (2003). Multiecho sequences with variable refocusing flip angles: optimization of signal behavior using smooth transitions between pseudo steady states (traps). *Magnetic Resonance in Medicine*, 49:527–535.

Hinshaw, W. S. (1976). Image formation by nuclear magnetic resonance: The sensitive-point method. *Journal of Applied Physics*, 47(8):3709–3721.

Humphrey, L., Deffebach, M., Pappas, M., Baumann, C., Artis, K., Mitchell, J., Zakher, B., Fu, R., and Slatore, C. (2013). Screening for lung cancer with low-dose computed tomography: A systematic review to update the u.s. preventive services task force recommendation. *Annals of Internal Medicine*.

Kauczor, H. (2009). *MRI of the Lung*. Springer.

Kjørstad, Å., Corteville, D., Henzler, T., Schmid-Bindert, G., Zöllner, F., and Schad, L. (2015). Non-invasive quantitative pulmonary v/q imaging using fourier decomposition mri at 1.5t. *Zeitschrift für Medizinische Physik*, page doi: 10.1016/j.zemedi.2015.02.002.

Kjørstad, A., Corteville, D. M. R., Fischer, A., Henzler, T., Schmid-Bindert, G., Zöllner, F. G., and R., S. L. (2014a). Quantitative lung perfusion evaluation using fourier decomposition perfusion mri. *Magnetic Resonance in Medicine*, 72(2):558–562.

Kjørstad, A., Corteville, D. M. R., Henzler, T., Schmid-Bindert, G., Hodneland, E., Zöllner, F. G., and Schad, L. R. (2014b). Quantitative lung ventilation using fourier decomposition mri; comparison and initial study. *Magnetic Resonance Materials in Physics*, 27(6):467–476.

Lauterbur, P. C. (1973). Image Formation by Induced Local Interactions: Examples Employing Nuclear Magnetic Resonance. *Nature*, 242:190–191.

Le Roux, P. (2003). Simplified model and stabilization of ssfp sequences. *Journal of Magnetic Resonance*, 163:23–37.

Levitt, M. H. (2007). *Spin Dynamics*. John Wiley & Sons.

Li, S. and Jain, A. (2011). *Handbook of Face Recognition*. Springer.

Martinez, F. (2007). Genes, environments, development and asthma: a reappraisal. *European Respiratory Journal*, 29:179–184.

Mason, R., Broaddus, C., and Martin, T. (2010). *Murray and Nadel's Textbook of Respiratory Medicine*. Saunders.

Meaney, J., Johansson, L., Ahlstrom, H., and Prince, M. (1999). Pulmonary magnetic resonance angiography. *Journal of Magnetic Resonance Imaging*, 10:326–338.

Modersitzki, J. (2003). *Numerical Methods for Image Registration*. Oxford University Press.

Molinari, F., Madhuranthakam, A., Lenkinski, R., and Bankier, A. (2014). Ultrashort echo time mri of pulmonary water content: assessment in a sponge phantom at 1.5 and 3.0 tesla. *Diagnostic and Interventional Radiology*, 20(1):34–41.

Mugler, J. and Altes, T. (2013). Hyperpolarized 129xe mri of the human lung. *Journal of Magnetic Resonance Imaging*, 37:313–331.

Myronenko, A. and Song, X. (2010). Intensity-based image registration by minimizing residual complexity. *IEEE Transactions on Medical Imaging*, 29:1882–1891.

Nishimura, D. and Vasanamala, S. (2000). Analysis and reduction of the transient response in ssfp imaging. *Proc. Intl. Soc. Mag. Reson. Med. 8*.

Nyquist, H. (1928). Thermal agitation of electric charge in conductors. *Physical Review*, 32(1):110–113.

Oppelt, A., Graumann, R., Fischer, H., Hertl, W., and Schajor, W. (1986). Fisp: a new fast mri sequence. *Magnetic Resonance in Medicine*, 3:15–18.

Paul, D. and Zaitsev, M. (2009). Improved snr in linear reordered 2d bssfp imaging using variable flip angles. *Magnetic Resonance Imaging*, 27:933–941.

Pauli, W. (1924). Zur Frage der theoretischen Deutung der Satelliten einiger Spektrallinien and ihrer Beeinflussung durch magnetische Felder. *Naturwissenschaften*, 12:741–743.

Puderbach, M., Eichinger, M., Gahr, J., Ley, S., Tuengerthal, S., Schmähl, A., Fink, C., Plathow, C., Wiebel, M., and Müller, F.-M. (2007). Proton mri appearance of cystic fibrosis: comparison to ct. *European Radiology*, 17:716–724.

Purcell, E. (1946). Resonance absorption by nuclear magnetic moments in a solid. *Physical Review*, 69:37–38.

R., S. (2013). A three-dimensional model of tracheobronchial particle distribution during mucociliary clearance in the human respiratory tract. *Zeitschrift für Medizinische Physik*, 23:111–119.

Rabi, I. I., Kellogg, J. M. B., and Zacharias, J. R. (1934). The magnetic moment of the proton. *Physical Review*, 46:157–163.

Rabi, I. I., Millman, S., and Kusch, P. (1939). The molecular beam resonance method for measuring nuclear magnetic moments. The magnetic moments of 3Li6, 3Li7 and 9F19. *Physical Review*, 55:526–535.

Rami-Porta, R., Crowley, J., and Goldstraw, P. (2009). The revised tnm staging system for lung cancer. *Annals of Thoracic and Cardiovascular Surgery*, 15:4–9.

Reilly, J. (1989). Peripheral nerve stimulation by induced electric currents: exposure to time-varying magnetic fields. *Medical and Biomedical Engineering and Computing*, 27(2):101–110.

Rich, S., Dantzker, D., Ayres, S., Bergofsky, E., Brundage, B., Detre, K., Fishman, A., Goldring, R., Groves, B., and Koerner, S. (1987). Primary pulmonary hypertension. a national prospective study. *Annals of Internal Medicine*, 107:216–223.

Roach, P., Bailey, D., and Harris, B. (2008). Enhancing lung scintigraphy with single-photon emission computed tomography. *Seminars in Nuclear Medicine*, 38:441–449.

Roemer, P. B., Edelstein, W. A., Hayes, C. E., Souza, S. P., and Mueller, O. M. (1990). The nmr phased array. *Magnetic Resonance in Medicine*, 16(2):192–225.

Rossmann, K. (1969). Point spread-function, line spread-function and modulation transfer function: Tools for the study of imaging system. *Radiology*, 14:257–272.

Samee, S., Altes, T., Powers, P., de Lange, E., Knight-Scott, J., Rakes, G., Mugler, J., Ciambotti, J., Alford, B., and Brookeman, J. (2003). Imaging the lungs in asthmatic patients by using hyperpolarized helium-3 magnetic resonance: assessment of response to methacholine and exercise challenge. *Journal of Allergy and Clinical Immunology*, 111:1205–1211.

Schäffter, T., Weiss, S., and Börnert, P. (2002). A sar-reduced steady state free precessing (ssfp) acquisition. *Proceedings of the International Society for Magnetic Resonance 10*.

Scheffler, K. and Lehnhardt, S. (2003). Principles and applications of balanced ssfp techniques. *European Radiology*, 13:2409–2418.

Slichter, C. P. (1996). *Principles of Magnetic Resonance*. Springer.

Sommer, G., Bauman, G., Koenigkam-Santos, M., Draenkow, C., Heussel, C., Kauczor, H.-U., Schlemmer, H.-P., and Puderbach, M. (2013). Non-contrast-enhanced preoperative assessment of lung perfusion in patients with non-small-cell lung cancer using fourier decomposition magnetic resonance imaging. *European Journal of Radiology*, 82:879–887.

Stadler, A., Jakob, P. M., Griswold, M., Barth, M., and Bankier, A. A. (2005). T1 mapping of the entire lung parenchyma: Influence of the respiratory phase in healthy individuals. *Journal of Magnetic Resonance*, 21:759–764.

Stanisz, G. J., Odrobina, E. E., Pun, J., Escaravage, M., Graham, S. J., Bronskill, M. J., and Henkelman, R. M. (2005). T1, t2 relaxation and magnetization transfer in tissue at 3t. *Magnetic Resonance in Medicine*, 54:507–512.

Weisskoff, R. (1996). Simple measurement of scanner stability for functional nmr imaging of activation in the brain. *Magnetic Resonance in Medicine*, 36:643–645.

West, J. (2008). *Respiratory Physiology: The Essentials*. Lippincott Williams & Wilkins.

Wild, J. M., Marshall, H., Bock, M., Schad, L., Jakob, P., Puderbach, M., Molinari, F., Van Beek, E., and Biederer, J. (2012). MRI of the Lung (1/3): Methods. *Insights Imaging*, 3:345–353.

Wood, R., Boat, T., and Doershuk, C. (1976). Cystic fibrosis. *American Review of Respiratory Disease*, 113:833–878.

Wujcicki, A., Corteville, D. M. R., Materka, A., and Schad, L. R. (2015). Perfusion and ventilation filters for fourier-decomposition mr lung imaging. *Zeitschrift für Medizinische Physik*, 25(1):66–67.

Zapke, M., Topf, H., Zenker, M., Kuth, R., Deimling, M., Kreisler, P., Rauh, M., Chefd'Hotel, C., Geiger, B., and T., R. (2006). Magnetic resonance lung function - a breakthrough for lung imaging and functional assessment? a phantom study and clinical trial. *Respiratory Research*, 7:106–115.

Zitova, B. and Flusser, J. (2003). Image registration methods: a survey. *Image and Vision Computing*, 21:977–1000.

Zöllner, F., Zahn, K., Schaible, T., Schoenberg, S., Schad, L., and Neff, K. (2012). Quantitative pulmonary perfusion imaging at 3.0 t of 2-year-old children after congenital diaphragmatic hernia repair: initial results. *European Journal of Radiology*, 22(12):2743–2749.

Zur, Y., Stokar, S., and Bendel, P. (1988). An analysis of fast imaging sequences with steady-state transverse magnetization refocusing. *Magnetic Resonance in Medicine*, 6(2):175–193.

List of Figures

List of Tables

Acknowledgments

For this section I would like to switch to my native language.

Die Zusammenstellung dieser Arbeit war kein leichtes Unterfangen und wäre mir vermutlich unmöglich gewesen ohne die Hilfe und Unterstützung einer Vielzahl von Personen. Mein besonderer Dank gilt:

Prof. Lothar Schad, der mir die Möglichkeit gegeben hat diese Arbeit zu verfassen und mir immer seine uneingeschränkte Unterstützung zukommen ließ, nicht nur während meiner Dissertation, sondern auch während meiner Diplomarbeit.

Prof. Peter Bachert für die Bereitschaft zur Begutachtung dieser Arbeit und seine Vorlesung Medizinische Physik 2, die mein Interesse an der MRT weckte.

Frank Zöllner, meinem Arbeitsgruppenleiter, der mich in allen Fragen, wissenschaftlich oder organisatorisch, immer ausgezeichnet beraten hat.

Dr. Thomas Henzler und Dr. Gerald Schmid-Bindert für ihre Zusammenarbeit bei der Patientenstudie.

Åsmund Kjørstadt, meinem geschätzten Kollegen und Freund, mit dem zusammen es mir möglich war alle unsere Ideen umzusetzen, egal ob am Tage oder spät in der Nacht.

Philipp Krämer, der mir nicht nur die Grundlagen der Sequenzprogrammierung beibrachte, sondern auch bei allen Fragen zu diesem Thema eine Antwort parat hatte.

Jascha Zapp, der mich immer wieder motivierte, wenn etwas nicht funktionierte. Lungen MRT ist eben nicht ganz einfach.

Fabian Zimmer für seinen Hinweis auf die VERSE Technik. Der Ausflug zum Dobel hat sich gelohnt.

Sebastian Domsch für viele interessante Diskussionen. Diese waren immer eine willkommene Abwechslung im schnöden Alltag.

Frau Sabina Cox für ihre Hilfe beim bürokratischen Austausch mit der Personalabteilung, der Universität und der EU.

Dem gesamten CKM Team für die einmalig gute Arbeitsatmosphäre.

Allen Teilnehmern, Professoren und Mitarbeitern des π-Net für die vielen informativen, aber auch immer lustigen Workshops, Vorträge und Diskussionen.

Allen Patienten und Probanden, die sich bereiterklärten an meinen Messungen teilzunehmen.

Zuletzt möchte ich auch den Personen danken, die zwar nicht direkt an dieser Arbeit beteiligt waren, aber ohne deren Zutun diese trotzdem niemals zustande gekommen wäre:

Meinen Eltern, meiner Oma, meiner Schwester und meinen beiden Brüdern, sowie meinen Freunden Maik, Michael und Oliver.

Vielen Dank.

Erklärung

Ich erkläre hiermit, dass ich die vorgelegte Dissertation selbst verfasst und mich dabei keiner anderen als der von mir ausdrücklich bezeichneten Quellen und Hilfen bedient habe.

Heidelberg, den ....., ...
Unterschrift